UCGE Reports

Number 20313

Department of Geomatics Engineering

Improving Carrier Phase Reacquisition Time Using Advanced Receiver Architectures

(URL: http://www.geomatics.ucalgary.ca/graduatetheses)

by

Peng Xie

September 2010

University of Calgary

Improving Carrier Phase Reacquisition Time Using Advanced Receiver Architectures

by

Peng Xie

A THESIS
SUBMITTED TO THE FACULTY OF GRADUATE STUDIES
IN PARTIAL FULFILMENT OF THE REQUIREMENTS FOR THE
DEGREE OF MASTER OF SCIENCE

DEPARTMENT OF GEOMATICS ENGINEERING
CALGARY, ALBERTA
SEPTEMBER, 2010

Abstract

A frequency lock loop (FLL) and a phase lock loop (PLL) are used to track the carrier in a GNSS receiver. In order to meet the most stringent positioning and navigation requirements, several receiver architectures have been proposed for global navigation satellite system (GNSS) including stand-alone receivers or GNSS receivers integrated with inertial navigation systems (INS). Basically, there are four receiver architectures, namely, standard receivers, estimator-based receivers, vector-based receivers, and ultra-tight receivers.

The objective of this work is to reduce the carrier phase reacquisition time using advanced receiver architectures. This paper looks at how different receiver architectures can be used or modified to more rapidly reacquire carrier phase tracking, thus providing more measurements that can be used for high-accuracy positioning applications. This contrasts with other work which has focused more on reacquiring range capability.

Specifically, a piece-wise control method and a phase prediction architecture are proposed. The piece-wise method takes advantage of different parameters in the control system to produce different transition performance within the tracking loop. With this in mind, the approach divides the reacquisition process into separate periods each with different control system parameters in order to achieve a faster transition process. In the phase prediction architecture, carrier phase measurements are predicted for satellites that have lost lock by integrating the estimated Doppler computed from the navigation solution. Predicted phase quality is evaluated in both empirical and theoretical ways. All algorithms are tested using real data collected under mild to moderate operational conditions.

Acknowledgements

It is a pleasure to thank those who made this thesis possible. First of all, I would like to thank my supervisor, Dr. Mark Petovello for his guidance, support and continuous encouragement during my studies. Furthermore, I would like to express my gratitude to Dr. Gérard Lachapelle, I really appreciate that he gave me the opportunity to study in the Position, Location And Navigation (PLAN) group.

I would like to express my thanks to Dr. Cillian O'Driscoll and Dr. Daniele Borio for their valuable discussions. I would further like to extend my thanks to those graduate students Haris Afzal, Billy Chan, Zhe He, Ahmed Kamel, Tao Li, Tao Lin, Ping Luo, Martin Ma, Debo Sun, Melania Susi, Da Wang in the PLAN group for providing a comfortable and co-operative working environment. Their precious suggestions and discussions on my work are appreciated.

The financial support of General Motors of Canada, the Natural Science and Engineering Research Council of Canada, Alberta Advanced Education and Technology and the Western Economic Diversification Canada are acknowledged.

Finally, and most importantly, I would like to thank my parents, for their unconditional love, encouragement, and understanding through all of my years. This work would not have been possible without their support.

Table of Contents

CHAPTER FOUR: PIECE-WISE CONTROL METHOD 53

List of Tables

List of Figures

List of Abbreviations and Symbols

Acronyms

C/A	Coase/Acquisition
C/N_0	Carrier to Noise Density
DCM	Direction Cosine Matrix
DLL	Delay Lock Loop
DOP	Delusion of Precision
ECEF	Earth Centre Earth Fixed
FLL	Frequency Lock Loop
FLI	Frequency Lock Indicator
GNSS	Global Navigation Satellite System
GPS	Global Positioning System
GSNRx^{TM}	GNSS Software Navigation Receiver
I	In-phase Correlator Output
I&D	Integrate and Dump
IF	Intermediate Frequency
IMU	Inertial Measurement Unit
INS	Inertial Navigation System
L1	L1 Frequency Band Centred at 1575.42 MHz
MEMS	Micro Electro-Mechanical Systems
NCO	Numerically Controlled Oscillator
PI	Proportional-Integration
PLAN	Position, Location And Navigation

PLL	Phase Lock Loop
PLI	Phase Lock Indicator
PRN	Pseudorandom Noise
PSD	Power Spectrum Density
PW	Piece-Wise
Q	Quadra-phase Correlator Output
RF	Radio Frequency
RMS	Root Mean Square
STD	Standard Deviation
SV	Space Vehicle
VDFLL	Vector Delay/Frequency Lock Loop
VDLL	Vector Delay Lock Loop
VFLL	Vector Frequency Lock Loop
WGS84	World Geodetic System (dating from 1984 and last revised in 2004)

Symbols

A	Signal Amplitude
B_n	Filter Noise Bandwidth
C	Transformation Matrix
K	Filter Gain
H	Observation Matrix
$H(s)$	Transfer Function

M_p	Maximum Overshoot
R_N	Prime Vertical Radius of Curvature
R_M	Meridian Radius of Curvature
T_c	Sampling Interval Time
b	Clock Bias
c	Speed of Light
d	Clock Drift
e	Earth Eccentricity
h	Height
g^n	Gravity with respect to the navigation frame
p	Vehicle Position Vector
p_i	Polynomial Coefficients
q	Quaternion
s	Laplace Variable
φ	Carrier Phase
φ_e	Phase Error
t_p	Peak Time
t_r	Rise Time
t_s	Settling Time
v	Velocity
ω	Angular Velocity

ω_n	Natural Frequency
ξ	Damping Ratio
z	z-Domain Parameter Representing a Step in Time
$\times$	Vector cross product
λ	Vehicle Longitude
L	Vehicle Latitude
ϕ	Roll Angle
θ	Pitch Angle
ψ	Azimuth
ε_k	Frequency Error
σ_f	Doppler Jitter
$\delta\tau$	Code Phase Error
$\delta\varphi$	Carrier Phase Error
δf	Carrier Frequency Error
δa	Carrier Acceleration Error
β	Converts from Units of Radians to Chips
ω_A	Driving Noise of Amplitude
$\omega_{\delta\tau}$	Driving Noise of Code Phase Error
ω_b	Driving Noise of Clock Bias
ω_d	Driving Noise of Clock Drift
ω_a	Driving Noise to Account for Line-of-Sight Acceleration

v	Vehicle Velocity Vector
ω_v	Velocity Uncertainty
ω_b	Clock Bias Uncertainty
ω_d	Clock Drift Uncertainty
ρ	Pseudorange
σ_H^2	Vehicle Horizontal Velocity Variance
σ_U^2	Vehicle Vertical Velocity Variance
α	Satellite Elevation
$\Delta\omega_0$	Initial Frequency Error

CHAPTER ONE: INTRODUCTION

The use of carrier phase techniques in Global Navigation Satellite Systems (GNSS) to reach centimetre-level positioning accuracy has gained increasing research interest in recent years. The reason for widely used carrier phase techniques is that the carrier phase measurements can provide better position information than code phase measurements due to its multipath and noise characteristics (Ronald et al 2006). Generally, phase error is less than 4 degrees (2 millimetres) in the high carrier to noise ratio (C/N_0) scenarios. Furthermore, the maximum multipath error is limited to a quarter of a wavelength (Lachapelle 2008).

Unfortunately, tracking requirements for the carrier phase are much more stringent than those for pseudorange or carrier Doppler, and loss of phase lock is likely when the received GNSS signals are weaker than normal (Petovello et al 2007), such as under bridges or dense-foliage, the receiver cannot provide phase measurements during loss of lock periods. With this in mind, how to reduce the carrier phase reacquisition time is the main concern of this thesis. More specifically, the objective is to reduce the carrier phase reacquisition time using advanced receiver architectures, with special focus on how different receiver architectures can be used or modified. Advanced receiver architectures include the estimator-based receiver, the vector-based receiver, and the GNSS integrated with inertial navigation systems (INS). Such approaches would provide more measurements that can be used for high-accuracy positioning applications.

1.1 Background and Motivation

1.1.1 Carrier Phase Introduction

Carrier phase measurements are obtained by taking the difference between the generated signal phases at receiver reception time and satellite transmission time respectively (Odijk 2002). Phase measurements are related to the geometric distance between the receiver and satellite. In the GNSS receiver, only the fractional part of carrier phase can be measured by integrating the Doppler offset in the phase lock loop, and results in an extremely accurate phase measurement between time epochs. The carrier phase noises include correlated and uncorrelated components (Gebre-Egziabher et al 2003). Uncorrelated noise could be considered as wide-band noise, most of which will be filtered out by the receiver (Ward et al 2006). Correlated phase errors on the other hand, include the stochastic errors in the satellite clock, the local oscillator errors when generating the NCO local replica, platform vibration, and dynamic stress due to platform motion.

1.1.2 Standard Tracking Loops Introduction

A frequency lock loop (FLL) and a phase lock loop (PLL) are used to track the carrier Doppler and carrier phase respectively in a GNSS receiver. The basic method of carrier tracking is to build a loop filter and use it to follow the input signal. The frequency (phase) differences between input and local replica are compared through a frequency (phase) discriminators, and then passed through the loop filter. A FLL-assisted-PLL scheme is used to improve the pull-in ability of the loop filter, as well as reduce the locking time (Ward et al 2006). In a standard receiver architecture, generally speaking, the carrier loop starts with acquisition, then transitions to a FLL, then to a FLL-assisted-PLL, and finally to a PLL. This is because the FLL is more robust to noise than PLL. Moreover, a FLL can tolerate higher receiver dynamics (Jwo 2001, Chiou 2004).

For a tracking loop, it is desirable that the transition process (transient response) to be sufficiently fast and damped (Ogata 1997). In GNSS tracking loops, the most widely used loop filters are second-order or third-order filters. For a second-order loop, the transition process is determined by the loop's damping ratio and natural frequency. There is always a trade-off in the design procedure of the damping ratio and natural frequency. A relatively small natural frequency will provide excellent noise performance but will be unable to track dynamics induced on the signal, and also the transition time will be large. In contrast, a relatively large natural frequency will reduce the transition time but will have poor noise performance (Chiou 2004, Gebre-Egziabher et al 2003).

Usually tracking loops use fixed natural frequency and damping ratio loop filters. The typical values for natural frequency and damping ratio in the FLL are 10 Hz and 0.707 respectively, and for PLL they are 15 Hz and 0.707 (Petovello et al 2007). An adaptive filter is employed in Sun (2010), Chiou et al (2007), Petovello et al (2007), and Gebre-Egziabher et al (2005), whereas the natural frequency is changed according to the receiver dynamics and signal power, and better frequency and phase tracking qualities are obtained.

1.1.3 Estimator-Based Architecture

In the estimator-based tracking loop, the discriminators and loop filters of the FLL and PLL are replaced by a single Kalman filter (Psiaki et al 2007, Petovello et al 2006). The goal of the Kalman filter is to improve the carrier tracking accuracy. The first advantage of an estimator-based tracking loop is that the observation noise is changed in the filter according to the C/N_0. In so doing, the natural frequency is adaptively adjusted (O'Driscoll et al 2009, Zarchan 2005), the natural frequency of an estimator-based tracking loop will be derived in this work. The second advantage is that a model is used to describe phase dynamics, whereas this link is indirect in a traditional tracking loop. The third advantage is that an estimator-based tracking loop has the capability to feedback both phase error and frequency error to the NCO, which enables shorter transition times in the tracking loop (Thomas 1989). Kalman filter theory is well documented in Gelb (1974), Brown et al (2002), Zarchan (2005), and Simon (2006) and will not be repeated here. In the GSNRx^{TM} software receiver, a five-state adaptive gain Kalman filter is employed to track the carrier (O'Driscoll et al 2009). In so doing, the natural frequency of the Kalman filter is adjusted in order to make a better estimation.

1.1.4 Vector-Based Architecture

The vector-based scheme combines the tracking of different satellites into a single algorithm by using a navigation filter. The outputs of the navigation filter are used to drive the code and frequency numerically controlled oscillators (NCO) (Gardner 2005). The primary advantages of vector-based tracking are noise is reduced in all channels making them less likely to enter the non-linear tracking regions, and it can operate with momentary blockage of one or more satellites (Petovello 2006, Spilker 1995).

There are several vector-based schemes, such as the vector delay lock loop (VDLL) (Van Dierendonck 1996), the vector frequency lock loop (VFLL) (Kiesel et al 2008, Lashley et al 2007), and the vector delay/frequency lock loop (VDFLL) (Petovello et al 2006, Bevly et al 2008). VDLL employs the user position and satellite position to predict the phases of the received pseudorandom noise (PRN) sequences. VFLL operates on a simple principle that the carrier Doppler of the received signal is based on the position and velocity of the user and satellite, as well as user clock drift. VDFLL is used to control both code NCO and carrier NCO, however, the carrier phase estimation is not available in the VDFLL architecture until an additional phase tracking loop is employed to track the carrier phase (Bevly et al 2008).

To this end, it is possible to reacquire satellites faster than the standard receivers in the vector-based architecture. Since the predicted Doppler is available from the navigation filter after the signal is received again, the tracking loop can be started with more accurate Doppler than the standard procedure. The ability to reacquire one satellite rapidly is shown in some previous works by employing the VFLL architecture (Bevly et al 2008); however, the work only concentrated on the initial frequency but not the phase. This thesis focuses on the carrier phase.

1.1.5 Integrated Navigation System Introduction

Inertial navigation systems have been used in a wide variety of navigation applications in the fields of marine, aerospace, and spacecraft technology (Bar-Itzhack 1988, Savage 2000, Rogers 2003, Soloviev 2004, Titterton and Weston 2004). The motivation of GNSS/INS integrated navigation is to take advantage of complementary operational characteristics of satellite navigation systems and inertial navigation systems. The estimation of INS error parameters allows GNSS/INS navigation with substantially smaller errors than could be achieved with either a stand-alone inertial navigation system or GNSS navigation system (Wendel et al 2004). The advantages of GNSS/INS integration include continued navigation during periods of GNSS signal outage, and possibly faster reacquire satellites as they come into view again or strong enough to acquire after loss of lock (Petovello et al 2006, Bevly et al 2008). And during highly dynamic maneuvers, INS velocity provides the GNSS tracking loops with additional information which is not available to a stand-alone GNSS receiver.

Loosely or tightly coupled GNSS/INS systems are defined depending on what kinds of Kalman filters are employed (Jekeli 2000, Wendel et al 2004, Farrell 1998). In a loosely-coupled GNSS/INS system, position and velocity from GNSS receiver are used as the measurements in the Kalman filter. In a tightly-coupled GNSS/INS system, the raw measurements, such as pseudorange and carrier Doppler, are employed directly in the Kalman filter as the measurements. Both loosely and tightly coupled schemes provide users with limited immunity against momentary signal outages (Alban et al 2003). The third scheme of integration, namely, ultra-tight coupled GNSS/INS, uses inertial sensors to aid the GNSS phase/frequency and code tracking loops directly (Wendel et al 2004, Alban et al 2003). The external Doppler information is employed to cancel the effect of dynamic stress in the ultra-tight receiver, and reduce the Doppler and carrier phase noise in the tracking loops (Wendel et al 2004, Petovello et al 2006, Alban et al 2003).

1.1.6 Software Receiver Introduction

The GSNRx^{TM} software receiver is employed in this work to process the GNSS signals. GSNRx^{TM} is a C++ based GNSS software receiver developed in the Position, Location And Navigation (PLAN) group at the University of Calgary (Petovello et al 2008, O'Driscoll 2009). GNSS software receivers replace the core components of the hardware receivers with software-based signal processing techniques. Software receivers have achieved a high level of maturity. The flexibility of software implementations allows rapid modifications of the receiver functions and parameters, which is not possible in the hardware implementations (Borre et al 2006). As a part of the research, the tracking functions in GSNRx^{TM} were modified to implement the proposed fast reacquisition scheme.

1.2 Previous Research Limitations

Different architectures of tracking loops were proposed and analyzed in the previous works (Thomas 1989, Spilker 1996, Best 2004, Ward et al 2006, Gardner 2005, O'Driscoll et al 2008). Regarding the reacquisition after loss of lock, most previous works concentrated on the code phase and carrier frequency reacquisition (Soloviev et al 2004, O'Driscoll et al 2008, Bevly et al 2008). Specifically, the aiding information was employed to reduce the size of the search space and therefore reduce the time taken to reacquire the signals. However, the carrier phase reacquisition strategy has not been analyzed yet, which is the main concern of this work.

The relationship between natural frequency, damping ratio, overshoot, and rise time has not been investigated in the previous work during the reacquisition process. In the general receiver tracking loop design, the fixed natural frequency and damping ratio are used in the loop filter. As mentioned in 1.1.2, a large natural frequency reduces the rise time and a large damping ratio will result in a small overshoot, as well as a small rise time (Ogata 1997). Moreover, the adaptive method in the previous works is only used to reduce the tracking noises, however, the special focus of this work is on the transition time.

As mentioned in section 1.1.4, the carrier signal reacquisition of the vector-based scheme in previous work (Bevly et al 2008) was considered in the scenarios where only one or two satellites lose lock, and the works only concentrated on the initial frequency in the FLL, not the phase. However, the essence of carrier phase is completely ignored, which is the integration of carrier Doppler from the tracking loop. Specifically, the Doppler for a satellite can be estimated by projecting the computed receiver velocity onto the satellite line of sight after loss of lock, and this, in turn, can be integrated to predict carrier phase measurements. In so doing, when the satellite signal becomes available again or at least strong enough to acquire, the phase of the signal is already predicted.

1.3 Objectives and Contributions

Given the lack of research towards the carrier phase acquisition, this work expands upon the work described in the previous section to reduce the carrier phase reacquisition time using advanced receiver architectures. To this end, the following tasks are arranged in this thesis.

1. *Piece-wise control method assessment*. Develop an adaptive scheme (piece-wise control method) for the phase reacquisition. The transition time for different natural frequencies and damping ratios will be assessed, specifically, to select a proper loop filter parameter set of interest in this work. Furthermore, can the piece-wise method be used in both FLL and PLL? Moreover, how to implement the piece-wise method in the third-order or higher order tracking loop systems is also a task of this work.
2. *Kalman filter transition process.* The transition process of estimator-based tracking loop will be assessed in this work. Can the Kalman filter be used to correct both frequency error and phase error scheme reduce the phase transition time? In order to make a fair comparison with the standard tracking loop, the natural frequency of Kalman filter will be derived in this work.
3. *Phase prediction method assessment.* Develop a phase prediction scheme during the loss of lock period. The phase prediction accuracy will be assessed under the different signal scenarios, such as partially dense-foliage scenario, dense-foliage scenario, and under passing the bridge scenario (with INS aiding). The relation between the predicted phase accuracy and receiver velocity performance will also

be considered in this work. Specifically, the phase reacquisition performance in the phase prediction architecture is of interest.

4. *Software receiver implementation*. In order to implement the piece-wise control method and phase prediction method, a manually induced loss of lock is created in the software receiver, and the carrier frequency and carrier phase are also reset manually for the local replica signal.

In realizing the above objectives, several contributions are made in this work and are summarized as follows:

1. Proposed the piece-wise control methods to reduce the carrier phase reacquisition time, which include a piece-wise FLL followed by a piece-wise PLL method, and a directly piece-wise PLL method. The performance of each approach was assessed using data collected on a vehicle under mild to moderate operational conditions. For the piece-wise method, the transition time was shown to be reduced by a factor of approximately three for the frequency pull-in period and by a factor of about four for phase pull-in period.
2. Kalman filter natural frequency for different process noise and observation noise is derived in this work, and a comparison between standard tracking loop and estimator-based tracking loop is conducted.
3. Phase prediction method is proposed and evaluated in this work, wherein continuous carrier phase measurements are effectively provided if the loss of lock period is small. In this situation, the reacquisition process could theoretically start with a small initial phase (and frequency) error, thus resulting in a faster carrier phase reacquisition.

1.4 Thesis Outlines

This thesis contains six chapters and three appendices which are organized as described below.

Chapter One presents the motivation, objectives and contributions of this work to improve the carrier phase reacquisition time. Results and limitations of previous work are shown.

In Chapter Two an overview of receiver tracking loops is provided. Standard tracking loops, estimator-based tracking loops, vector-based tracking loops, and ultra-tight tracking loops are introduced in this chapter.

Chapter Three presents the INS introduction and various strategies for GNSS/INS integration. For inertial navigation system, the coordinate system, coordinate transformation, and mechanization equations are presented.

In Chapter Four the piece-wise control method is discussed, the parameter tuning process is presented, and the performance of piece-wise FLL followed by a piece-wise PLL method, and a directly piece-wise PLL method, are shown in this chapter.

Chapter Five presents the phase prediction method, which is conducted in both vector-based receiver and ultra-tight receiver. The phase prediction performances under different signal power scenarios are considered. Specifically, partially dense-foliage, dense-foliage, and passing under bridges are considered.

In Chapter Six the summary and recommendations for future work are presented.

The appendices contain various detailed information relevant the thesis.

CHAPTER TWO: TRACKING LOOP OVERVIEW

This chapter describes the theory behind tracking loop design. Standard tracking loops, estimator-based tracking loops, and vector-based tracking loops are introduced in this chapter. Generally, a GNSS receiver contains a code tracking loop and a carrier tracking loop (Ward et al 2006). The code tracking loop is used to get the pseudorange from the satellite to the receiver; on the other hand, the carrier tracking loop is used to get the carrier Doppler and carrier phase. The pseudorange is used to compute the user position and the carrier Doppler is used to compute the user velocity (Spilker 1996).

Tracking loops continuously follow the dynamic of the incoming signal. Carrier tracking loops in GNSS receivers include frequency tracking and phase tracking, which can be performed by frequency lock loops (FLLs) and phase lock loops (PLLs) respectively (Ward et al 2006). PLL also tracks carrier frequencies; however, the tracking requirement is more stringent than FLL. It is very hard to directly track the carrier phase in a GNSS receiver due to the poor frequency pull-in ability of phase tracking loop. The general acquisition procedure is to start from carrier frequency tracking to reduce the Doppler uncertainty and then transition to carrier phase tracking. If the receiver loses track of a satellite, an acquisition process must be performed again to reacquire the satellite (Gardner 2005). Most GNSS receivers track carrier phases to get high accuracy phase measurement (Spilker 1996).

2.1 Standard Receiver

Generally, a frequency lock loop and a phase lock loop are employed in the GNSS receiver to track the carrier frequency and carrier phase respectively. Figure 2.1 shows the structure of a basic second-order tracking loop.

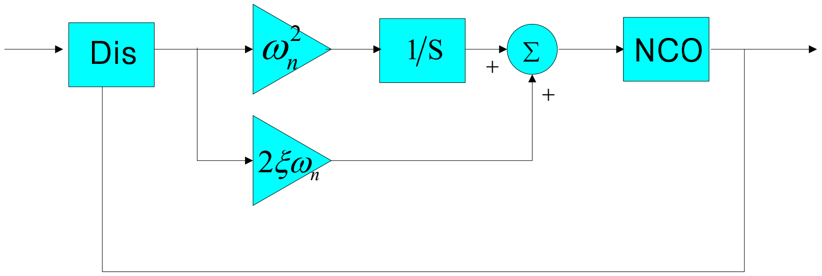

Figure 2.1: Basic Second-Order Tracking Loop

A tracking loop is a feedback system that tracks the frequency or phase of a received signal. The basic purpose of a FLL (PLL) is to generate a signal whose frequency (frequency and phase) approximates the frequency (frequency and phase) of the received signal (Best 2004). The tracking loop contains three essential elements: a discriminator, a loop filter, and a numerically controlled oscillator (NCO) (Gardner 2005). The signal enters the tracking loop after down-conversion and sampling. After the PRN code and carrier frequency are correlated with a local signal (over a pre-defined integration interval), the in-phase (I) and quadra-phase (Q) correlator outputs are passed to the discriminators (Borre et al 2006). A discriminator defines the type of tracking loop, for a FLL, the discriminator is used to obtain the frequency difference between the received signal and the local replica; for a PLL, the discriminator is used to get the phase error estimate (Ward et al 2006). The phase error is defined as the average phase error over the integration interval. Several types of frequency detector and phase detector are introduced in Ward et al (2006), an arctangent-type discriminator is used in this work for carrier phase tracking. The errors from the discriminators are then fed to the loop filter, which then delivers a suitable control signal to the NCO to generate a local replica. Of these three elements, the loop filter is most relevant in the context of this thesis. As such, the functions of the loop filter are discussed in Section 2.1.1.

2.1.1 Loop Filter Introduction

The loop filter has three main functions. The first function is to track the signal dynamic induced by the user and satellite motion. The second function is to filter out unwanted portions of the signal. Since the lower frequency signals are of interest, the loop filter must be a low-pass filter (Best 2004). The third function is to reduce the initial errors caused by the frequency or phase mismatch between the received signal and the local replica. For a FLL, the initial frequency error is reduced during the tracking process; for a PLL, both the initial frequency error and initial phase error are reduced during the tracking process.

The loop filter is characterized by its sensitivity to dynamic errors, and its transition performance in the presence of discontinuities. The transition process is defined in Section 2.1.2. The dynamic analysis of a loop filter is normally performed on its transfer function, $H(s)$, which relates the system input and output signals. The typical closed-loop transfer functions during the tracking process are given by the following equations for first, second and third-order loops respectively (Best 2004).

$$H\left(s\right)=\frac{G\left(s\right)}{1+G\left(s\right)}=\frac{\omega_n}{s+\omega_n} \tag{2.1}$$

$$H\left(s\right)=\frac{G\left(s\right)}{1+G\left(s\right)}=\frac{2\xi\omega_n s+\omega_n^2}{s^2+2\xi\omega_n s+\omega_n^2} \tag{2.2}$$

$$H\left(s\right)=\frac{G\left(s\right)}{1+G\left(s\right)}=\frac{2\omega_n s^2+2\omega_n^2 s+\omega_n^3}{s^3+2\omega_n s^2+2\omega_n^2 s+\omega_n^3} \tag{2.3}$$

where s : Laplace variable

ω_n : Natural frequency

ξ : Damping ratio

Strictly speaking, the damping ratio only applies to the second-order control system. For the first-order and third-order systems, the performance is only decided by the natural frequency, as shown in Equations (2.1) and (2.3). The loop filter natural frequency must be set to reject most of the noise. As discussed in Ogata (1997) and Gardner (2005), a narrow natural frequency loop filter is capable of rejecting the incoming noise but has degraded performance to track the signal dynamic. On the other hand, wide natural frequency loop filter can track both satellite and receiver dynamics, but the drawback is that more noise is introduced in the tracking loop. As discussed above, the loop filter natural frequency must be sufficiently large to track the signal dynamics and also be sufficiently small to minimise the signal noise. Generally, noise bandwidth is used to describe the loop filter noise mitigation behaviour, the relation between noise bandwidth and natural frequency is given by (Ward et al 2006).

Table 2-1: Relation between Natural Frequency and Noise Bandwidth

Loop Order	Noise Bandwidth as a Function of ω_n
First	$B_n = 0.25\omega_n$
Second	$B_n = 0.53\omega_n$
Third	$B_n = 0.7845\omega_n$

where B_n is noise bandwidth.

Figure 2.2 shows the frequency tracking performance with different FLL natural frequencies. As shown in this figure, a larger natural frequency introduces more noise in the loop filter.

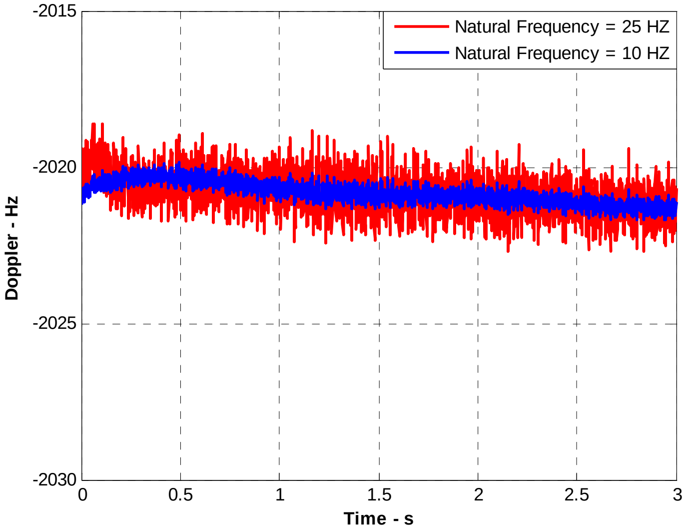

Figure 2.2: Frequency Tracking Performance of a Second-Order Loop with Different Natural Frequencies

The damping ratio controls how much overshoot the filter can have and also controls how fast the filter reaches its steady-state (Borre et al 2006). The choice of the damping ratio is a trade-off between the overshoot and the transition time. Generally, the value of 0.707 is preferred since a filter with this specified damping ratio converges reasonably fast and the overshoot is not high (Ogata 1997).

The tracking errors of GNSS receivers include two major components: the error caused by the thermal noise, and the steady-state error caused by the vehicle dynamics (Jwo 2001). A small steady-state error is usually desired for GNSS signal tracking. In control systems, the steady-state error is defined as the deviation of the output signal from the input after the transition process has died out (Ogata 1997). Different loop orders have different dynamic tracking performance, as shown in Table 2-2 (Ward et al 2006).

Table 2-2: Steady-State Tracking Loop Errors (from Ward et al 2006)

Loop Order	Steady-State Error	Characteristics
First	$\varphi_e = \frac{\Delta f}{\omega_n}$	Sensitive to velocity stress
Second	$\varphi_e = \frac{\Delta \dot{f}}{\omega_n^2}$	Sensitive to acceleration stress
Third	$\varphi_e = \frac{\Delta \ddot{f}}{\omega_n^3}$	Sensitive to jerk stress

where Δf is the phase rate.

Third-order loop filters have better dynamic tracking performance than first-order and second-order loop filters; however, third-order loop filters are unstable in some scenarios (Gardner 2005). Second-order loop filters are preferred in the low dynamic scenarios, since second-order loop filters are unconditionally stable with any parameters (Gardner 2005). The loop filter design methods are well documented in the literature, e.g. Best (2004), Gardner (2005), and Borre et al (2006).

2.1.2 Loop Filter Transition Process Analysis

The tracking loop goes through the transition process when subject to a discontinuous input in order to reduce both the frequency error and the phase error to near zero. The transition process of a control system usually exhibits damped oscillatory behaviour before reaching steady-state (Ogata 1997). Common specifications of a transition process are rise time, peak time, settling time, and maximum overshoot, as shown in Figure 2.3. In this figure, y is the filter response; M_p is maximum overshoot, which defined as the maximum peak value of the response curve from unity; t_r is rise time, which defined as the time required for the filter response to rise from zero to its final value (unity); t_p is peak time, which defined as the time required to reach the first peak of overshoot; t_s is settling time, which defined as the time required for the response curve to reach and stay with a predefined final value (usually 5% of the final value). For faster carrier phase reacquisition, a tracking loop with acceptable settling time and overshoot is needed. In this work, the settling time is defined as the transition time.

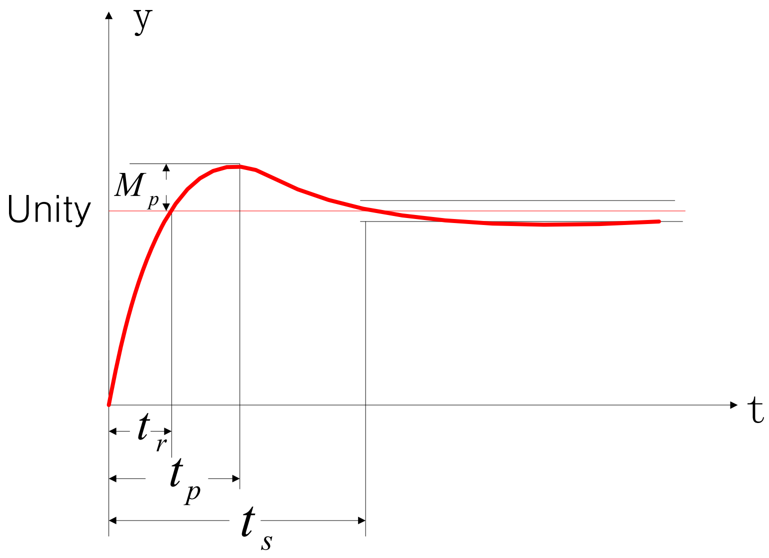

Figure 2.3: Illustration of Tracking Loop Transition Process

Before the carrier phase reacquisition analysis, the performance of a standard receiver after a loss of lock must be assessed first. The carrier loop starts with acquisition after a loss of lock and then consecutively transitions to a FLL, a FLL-assisted-PLL, and finally a PLL. This can be a time consuming process. Below, the effect of different natural frequencies and damping ratios on the transition time is assessed for a general second-order control system, where the nonlinear behaviour of discriminator is not considered.

Figure 2.4 shows the transition process of a general second-order loop using different damping ratios with a fixed 10 Hz natural frequency, which is generally used in the frequency tracking loop (O'Driscoll 2008). The system in the figure is excited by a unit step signal. As can be seen in the figure, loop filters with smaller damping ratios have larger overshoot in the transition process. In contrast, a larger damping ratio results in a smaller overshoot and also a shorter transition time.

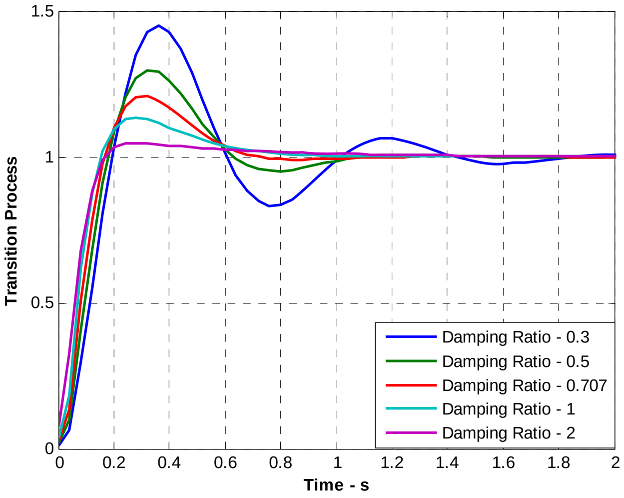

Figure 2.4: Transient Response for Different Loop Damping Ratios with Fixed 10 Hz Natural Frequency

Considering the natural frequency, Figure 2.5 shows the transition process of a second-order loop using different natural frequencies with a fixed damping ratio of 0.707. In this case, a larger natural frequency results in a shorter transition time.

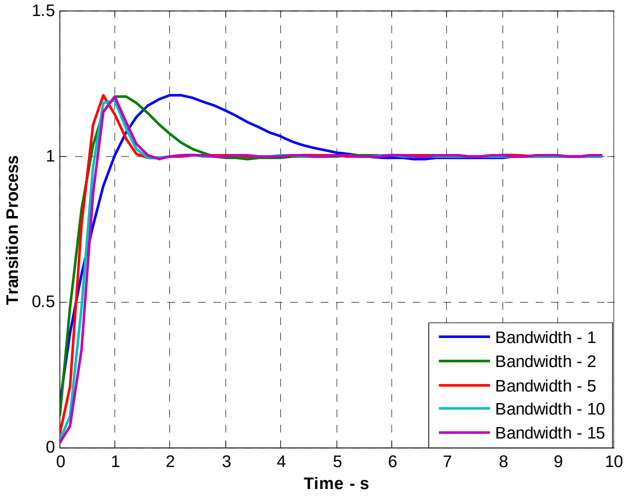

Figure 2.5: Transient Response for Different Loop Natural frequencies with Fixed 0.707 Damping Ratio

Figure 2.4 and Figure 2.5 suggest that if the damping ratio and natural frequency are increased during the reacquisition process, a faster transition process is expected. Figure 2.6 shows the performance of a second-order tracking loop with a large natural frequency and a large damping ratio (15 Hz natural frequency and 2.1 damping ratio), also, the performance with typical parameters (10 Hz natural frequency and 0.707 damping ratio) is shown.

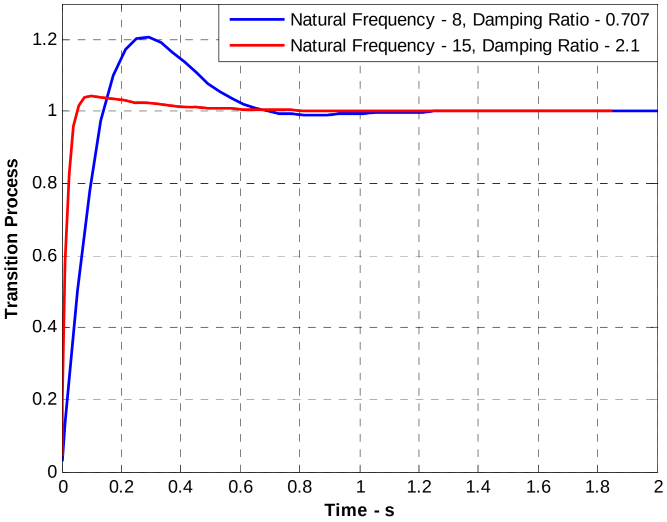

Figure 2.6: Transient Response Comparison between Large Natural frequency and Damping Ratio and Typical Natural Frequency and Damping Ratio

The filters with a large natural frequency and damping ratio loop converge faster and have smaller overshoot than the filters with the general parameter values; however, high damping ratios and wide natural frequencies are not always ideal. Specifically, higher damping ratios cause slower reactions to the user dynamics, and wider natural frequencies introduce more noise in the tracking loop. Correspondingly, a better method is introduced in Chapter 4 to take advantage of the tracking loops with high damping ratios and wide natural frequencies.

For carrier phase reacquisition, the transition process of different initial errors should be evaluated first. Before the initial frequency error analysis, the definition of the loss of lock should be clarified first. Two types of loss of lock are defined in this work, namely, loss of phase lock and loss of signal lock. Loss of phase lock occurs when the phase error is larger than a pre-decided phase threshold in the PLL. In the GSNRx^{TM} software receiver, a loss of phase lock is declared when the phase lock indicator (PLI) is smaller than 0.5 (30 degrees phase error), when this happens, the receiver transitions to a FLL (O'Driscoll 2008). However, one thing should be noted, in the loss of phase lock case, the frequency tracking loop still works well. Loss of signal lock means the receiver does not track this satellite anymore, every time this happens, the receiver restarts the signal acquisition procedure.

With this in mind, the initial frequency error assessment is only necessary in the loss of signal lock case. The frequency error is mainly due to the vehicle dynamics, satellite movement and receiver clock drift after the loss of signal lock. For the frequency error due to the satellite component, the maximum Doppler drift rate is on the order of 0.9 Hz per second (Watson 2005). Assuming a 30 second interval in which the signal is unavailable or too weak to acquire and track (the “loss of lock time”; 30 s is quite long). The Doppler uncertainty due to satellite motion in this case is 27 Hz. For vehicle motion, assuming the line of sight velocity changes by 30 m/s (100 km/h, which is the general case in a ground-based vehicle scenario) over 30 seconds, the Doppler change is approximately 150 Hz for the GPS L1 signal. Finally, for even relatively poor oscillators, the frequency stability over 30 seconds is negligible compared to the previous two effects. As such, the total Doppler uncertainty after 30 s is approximately 200 Hz.

Figure 2.7 shows the transition process of different initial frequency errors (manually induced in the software receiver) in a FLL. The lower plots in the figures show the errors with a magnified y-axis scale. Selected frequency errors are 10 Hz, 20 Hz, 30 Hz, 50 Hz, 100 Hz, and 200 Hz, thus encompassing the full range of values assumed above. The FLL natural frequency is 10 Hz, the coherent integration time is 1 ms. As might be expected, the transition time for larger initial frequency error is longer than smaller initial frequency error.

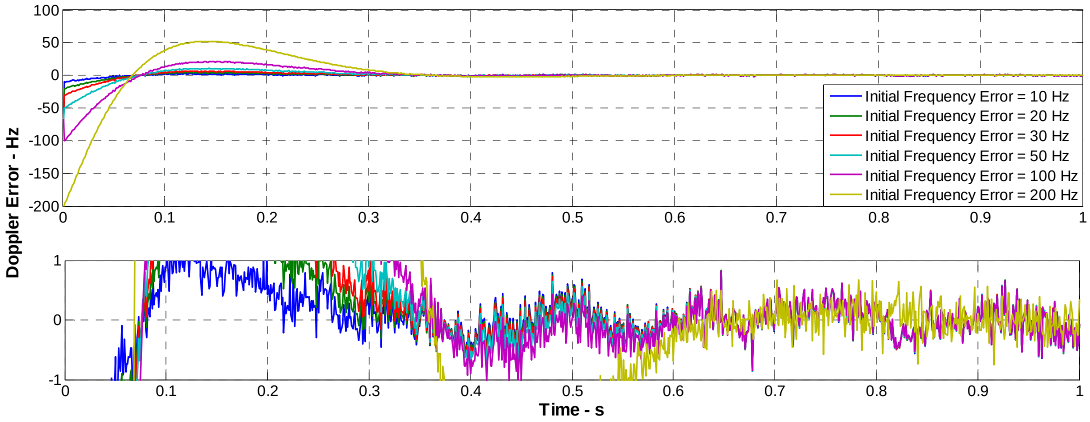

Figure 2.7: Transition Process of Second-Order FLL with Different Initial Frequency Errors (bottom plot is a zoomed in version of the top plot)

Figure 2.8 shows the transition process for different initial phase errors (manually induced in the software receiver) in a PLL with zero initial frequency error for a loop natural frequency of 15 Hz, similarly, smaller initial phase errors have faster transition processes in a PLL.

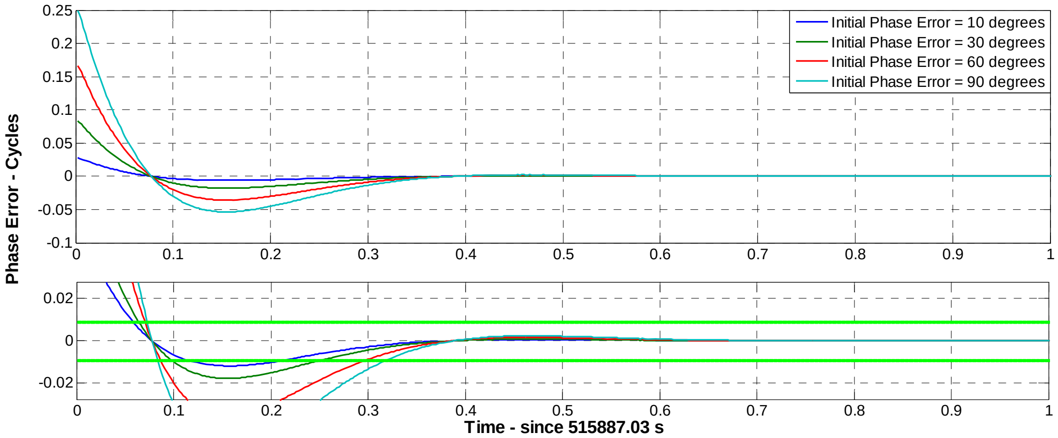

Figure 2.8: Transition Process of Second-Order PLL with Different Initial Phase Errors (bottom plot is a zoomed in version of the top plot)

Notice that the phase error is “zero” after reaching steady-state, this is due to the phase reference is obtained from the same tracking loop without manually induced loss of phase lock, as such, they have the same steady-state behaviours. In the real situation, the phase error is characterized by the phase jitter. Figure 2.7 and Figure 2.8 suggest that having smaller initial errors in the tracking loop can improve the reacquisition performance.

Since the damping ratio concept does not apply to the higher order loop filters, instead of increasing the damping ratio and natural frequency separately in the second-order system, the gain of the loop filter can be directly increased to reduce the transition time and overshoot. The structure of a second-order tracking loop with a filter gain is shown in Figure 2.9.

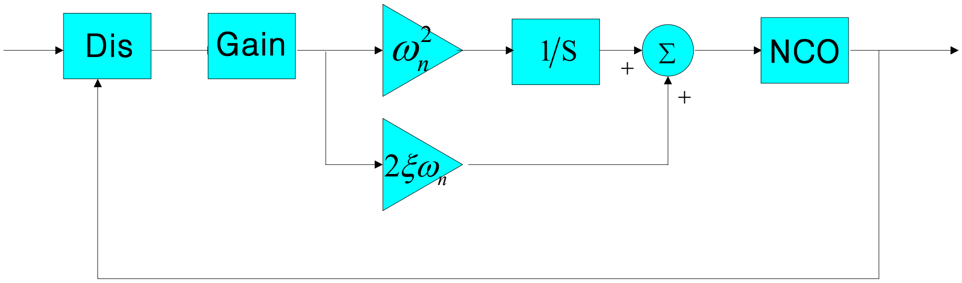

Figure 2.9: Second-Order Tracking Loop with Large Filter Gain

The open-loop transfer function for second-order loop filter with gain K is given by:

$$G(s) = K\frac{2\xi\omega_n s + \omega_n^2}{s^2} \tag{2.4}$$

If let:

$$K = a^2 \tag{2.5}$$

Then, substitute Equation (2.5) in Equation(2.4) gives:

$$G(s) = \frac{2(a\xi)(a\omega_n)s + (a\omega_n)^2}{s^2} \tag{2.6}$$

Equation (2.6) shows that a filter amplified by a large gain of a^2 has the same transfer function as a filter with the natural frequency and damping ratio increased by a factor of a.

For the third-order loop filter, the transfer function is solely decided by the natural frequency, as shown in the Equation (2.3). The relation between gain and natural frequency is not as obvious as second-order system shown in Equation (2.6), however, large gain can also reduce the overshoot and transition time for the third-order loop filter, as shown in Figure 2.10, where the natural frequency is 6 Hz.

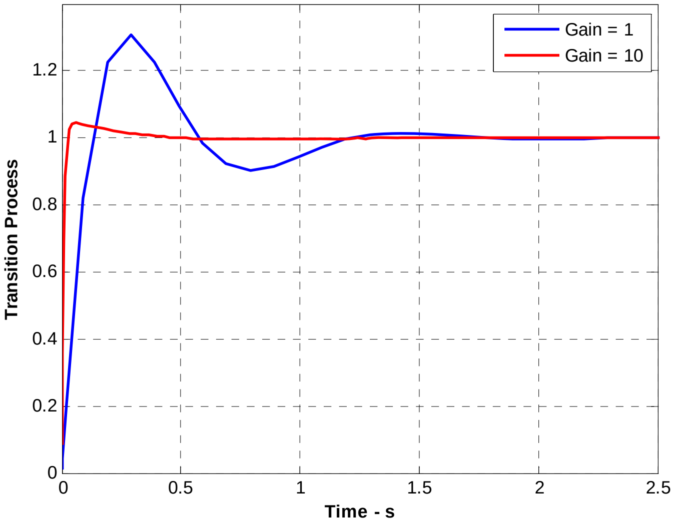

Figure 2.10: Transient Response Comparison between Large Gain and General Parameter Values for a Third-Order Loop

It is shown that the filters with a large filter gain converge faster and have smaller overshoot than the filters with the general parameter values.

2.1.3 Discrete Loop Filter

In the previous sections, the discussions were based on analog systems. In order to process the digitized data in software receivers, the analog signals must be converted into discrete signals (Tsui 2004). Generally, FLLs and PLLs are designed by using the analog methods in the continuous time domain. The digital tracking loops are then derived from the analog tracking loops. Several techniques can be employed to design the loop filter in the digital domain; however, the most commonly used method is based on transformation methods, where the discrete form is obtained by means of mapping functions from the analog domain. The step invariant mapping method is employed in GSNRx$^{\text{TM}}$ software receiver to convert a continuous loop filter to a digital loop filter, which is given by (Borio and O'Driscoll 2009):

$$s \to \frac{(z-1)}{T_c z} \tag{2.7}$$

where z : z-domain parameter representing a step in time (Jury 1964)

T_c : Sampling interval time (i.e., integration time)

Note that the transformation methods are effective only when $B_n T_c << 1$, where B_n is the filter noise bandwidth (Ward et al 2006).

The following is an example showing how to get the discrete form second-order PLL loop filter. The continuous open-loop second-order loop filter transfer function is given by (Ward et al 2006):

$$\frac{Y(s)}{X(s)} = \frac{2\xi\omega_n s + \omega_n^2}{s} \tag{2.8}$$

Substituting Equation (2.7) into Equation (2.8) gives:

$$\frac{Y(z)}{X(z)} = \frac{\left(2\xi\omega_n + \omega_n^2 T_c\right) - 2\xi\omega_n z^{-1}}{1 - z^{-1}} \tag{2.9}$$

By using the z inverse transformation, the discrete form loop filter is given by (Tsui 2004):

$$y_k = y_{k-1} + \left(2\xi\omega_n + \omega_n^2 T_c\right) x_k - 2\xi\omega_n x_{k-1} \tag{2.10}$$

where y_{k-1} : Filter output at the last epoch

x_{k-1}, x_k : Filter inputs at the last epoch and the current epoch respectively

2.2 Estimator-Based Receiver

In estimator-based receivers, the traditional discriminators and loop filters in the PLL are replaced by a local Kalman filter (Petovello et al 2006, Psiaki et al 2007). The goal of the Kalman filter is to improve the carrier tracking accuracy. Kalman filter theory is well documented in Gelb (1974), Brown et al (2002), Zarchan (2005), and Simon (2006), and will not be repeated here.

Three-state Kalman-based tracking loop is shown in Appendix B, where the states included are the code phase error, the carrier frequency error, and carrier acceleration error. The equivalence between third-order standard tracking loop and Kalman filter is shown there. However, the combined DLL and PLL approach is employed in the software receiver (Petovello et al 2006), where a five-state Kalman filter is used to track the errors in the predicted signals. The states estimated in this case are the amplitude of signal, the code phase error, the carrier phase error, the frequency error and the carrier acceleration error. More details about local five-state Kalman filter will be shown in Chapter 5.

The transition process for the standard tracking loop was already shown in the section 2.1.2. Recall that the transition time is decided by the loop filter natural frequency and damping ratio (for second-order loop filter). One thing should be noted in the standard tracking loop that only frequency is corrected during the tracking process. However, in the estimator-based architecture, both frequency error and phase error are corrected during the tracking process, which means that the transition process should be different from the standard tracking loops. In this section, the transition process for the estimator-based tracking loop is assessed. The parameters used in the local Kalman filter are shown in Table 2-3.

Table 2-3: Local Kalman Filter Parameters

States	5
C/N_0	50 dB/Hz
Observation Noise	0.005
Line of Sight Spectral Density	4 $m/s^2/\sqrt{Hz}$
Integration Time	1 ms

As shown in Appendix C, for 50 dB/Hz C/N_0 and 4 $m/s^2/\sqrt{Hz}$ line of sight spectral density, the equivalent natural frequency is around 5 Hz.

As with the standard FLL assessment, a manual frequency offset was induced in the software receiver to evaluate the transition process for estimator-based tracking loop. Figure 2.11 shows the transition process for third-order standard FLL (5 Hz natural frequency) and estimator-based tracking loop, the initial frequency error is 20 Hz. Generally, it is not common to use a third-order FLL, however, in order to have a direct comparison with the estimator-based approach, a third-order standard FLL is used here. Moreover, a second-order standard FLL can also be compared with a two-state Kalman filter, where the carrier acceleration error is removed from the state vector, however, a shorter transition time for the two-state estimator-based receiver is expected.

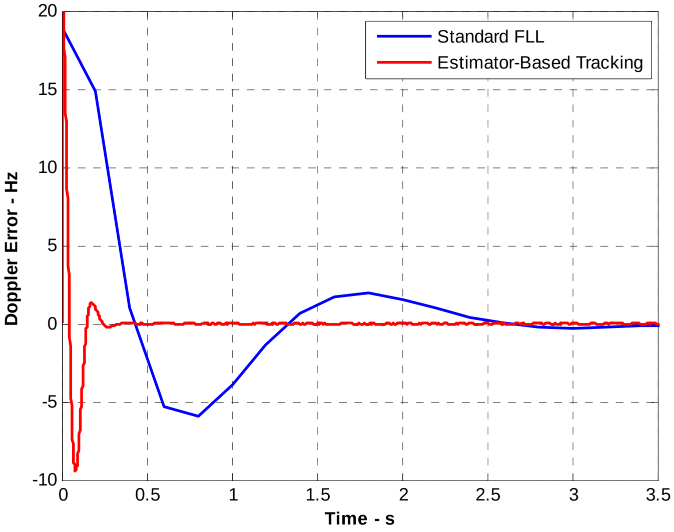

Figure 2.11: Carrier Frequency Transition Process for Third-Order Standard FLL and Estimator-Based Tracking of 5 Hz Natural Frequency with 20 Hz Initial Frequency Error

Obviously, the estimator-based tracking loop has faster transition process than standard FLL, however, it is also observed that the overshoot for estimator-based tracking loop is slightly larger than the standard FLL.

The same as the standard PLL assessment, a manual phase offset was induced in the software receiver to evaluate the transition process for estimator-based tracking loop. Figure 2.12 shows the phase transition process for 0.2 cycles initial phase error (frequency error is zero), the natural frequency for the standard PLL is 5 Hz.

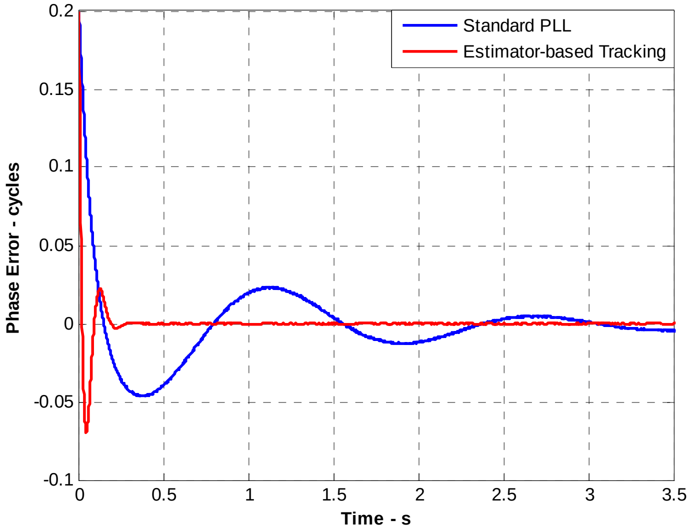

Figure 2.12: Carrier Phase Transition Process for Third-Order Standard PLL and Estimator-Based Tracking of 5 Hz Natural Frequency with 0.2 Cycles Initial Phase Error

Figure 2.11 and Figure 2.12 suggest that for the carrier phase reacquisition, estimator-based receiver can provide faster transition process than standard PLL.

2.3 Vector-Based Architecture

The vector-based tracking concept was initially introduced by Spilker (1994). Different from conventional GNSS receivers, a vector-based receiver combines the tracking of all the visible satellites through a composite filter. In a standard receiver and estimator-based receiver, signal tracking is done on a satellite-by-satellite basis, which means all satellites are tracked separately and no information is shared between channels. The advantage of this kind of architecture is that it is more robust and one satellite will not corrupt another. However, in the vector-based architecture, it operates on a simple principle that the code phase, code Doppler, and carrier Doppler of the received signal are based on the position and velocity of the user and satellite. In this way, the navigation solution is used to drive the code and frequency NCO values in the receiver.

The primary advantage of vector-based architectures is that noise is reduced in all channels, and the receiver is less likely to enter the non-linear tracking regions, which in turn, should improve the signal tracking ability under weak signal scenarios (Petovello 2006). Another advantage is possibly reacquiring satellites faster than the standard receivers. Since the predicted Doppler is available from the navigation filter after the signal is received again, the tracking loop can be started with more accurate Doppler than the standard procedure. The ability to reacquire one satellite rapidly is shown in some previous works by employing the vector-based FLL (VFLL) architecture (Bevly et al 2008); however, the work only concentrated on the initial frequency but not the phase. This thesis focuses on the carrier phase.

In the vector-based architecture, a separate phase tracking loop should be employed to track the carrier; otherwise, the phase measurements cannot be obtained (Bevly et al 2008). Usually, a cascaded approach is employed in the vector-based architecture (Kim et al 2003, Jovancevic et al 2004, Petovello et al 2007, 2008). In this case, each channel employs a local loop to track the carrier.

Figure 2.13 shows the structure of the vector-based receiver employed in the GSNRx^{TM} software receiver. Two different Kalman filters are employed in this case to track both frequency and carrier phase, namely, the navigation filter and the local filter.

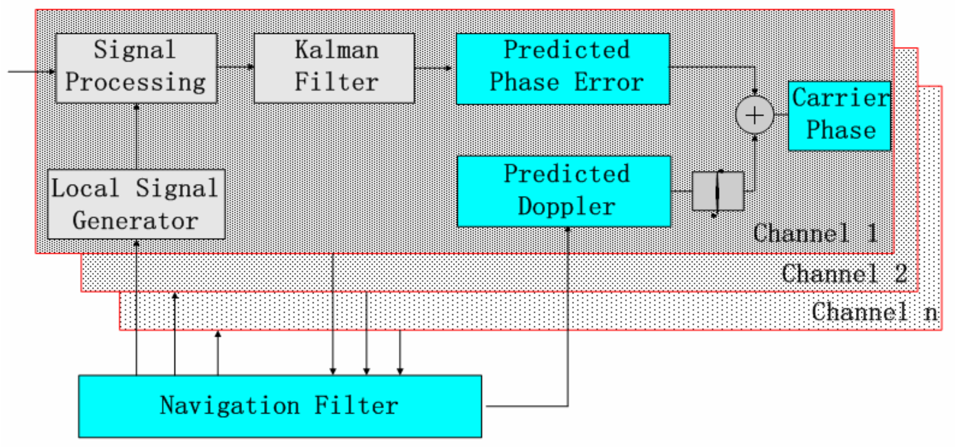

Figure 2.13: Vector-Based Phase Tracking Strategy

The estimator-based PLL discussed in Section 2.2 is employed as the local filter in the vector-based architecture. The navigation filter is employed to close the tracking loop and control the NCOs. Position error, velocity error, and clock error are estimated in the navigation filter (Petovello et al 2008, Bevly et al 2008). The measurements used to update the navigation filter are the pseudorange and carrier Doppler from each channel. In some other implementations, the error estimates from the local filters could be used directly to update the navigation filter. With the known position and velocity of the user in the navigation filter, the feedback to the local signal generators are obtained from the predicted range and Doppler to each satellite. Details will be shown in Chapter 5.

CHAPTER THREE: OVERVIEW OF GNSS/INS INTEGRATION

This chapter describes the theory behind integrated navigation systems using GNSS and inertial data. The inertial navigation systems (INS) are self-contained systems, which do not rely on external information. INS provides position, velocity and attitude information based on the sensor outputs; accelerometers provide acceleration information of the vehicle, and gyroscopes provide orientation information (Savage 2000). Therefore, INS is essentially immune to the external interference. However, the accuracy of an INS is limited by the sensor accuracy, which introduces position and velocity errors that increase with time. In addition, INS requires an initial alignment process, which can be challenging with low-cost sensors.

In contrast, the estimated accuracy of GNSS remains at the roughly same level over time assuming the signal environment remains approximately the same. The advantages of GNSS include no external input for initialization, and both position and velocity estimates are bounded. The disadvantage of GNSS is the signal is easily to be interrupted by the surrounding objects causing multipath errors, and loss of lock over short time periods is possible due to the signal blockage, interference, or jamming (Farrell 1998). Also, the output rate is relatively lower compared to an INS.

GNSS/INS integrated navigation systems take advantage of the complementary characteristics of different systems. The combined system offers a significant gain in performance in terms of accuracy and robustness compared to the standalone usage of either system (Wendel et al 2004). The growth of INS navigation errors with time is reduced by using aiding information from GNSS receivers.

This chapter starts with a review of inertial navigation systems and then moves to loosely-coupled, tightly-coupled, and ultra-tight GNSS/INS integration strategies.

3.1 Inertial Navigation System Overview

An Inertial Navigation System (INS) is used for autonomously determining position using inertial angular rate sensors, acceleration sensors, and a data processing computer (Savage 2000). The original applications of inertial navigation system used stable platform techniques. In these systems, the inertial measurement unit (IMU) is mounted on a stable (gimballed) platform and, most importantly, it is mechanically isolated from the rotation of the vehicle relative to the navigation frame. Modern INS systems have removed most of the mechanical platform, however, in particular applications where very high accuracy is required, gimballed platform systems are still commonly used, such as missile and submarine systems. Instead, modern systems rigidly attach the inertial sensors to the body of the host vehicle, forming what is called a strapdown system. In the strapdown system, the physical platform is replaced by the mathematical platform which represented by Euler angles. The potential benefits of this method are lower cost and greater reliability compared to the equivalent platform systems. However, the computational load for strapdown system is increased (Titterton and Weston 2004). The principal functions executed in the computer are angular rate integration and specific force transformation (Savage 1998), which collectively represent the “mechanization”. In the mechanization process, the platform angles are obtained in the angular rate integration process. At the same time, acceleration is obtained after removing the acceleration due to gravity, and the single and double integration of acceleration allows for the estimation of the velocity and position of the vehicle respectively. This section begins with the coordinate systems review, and then the INS mechanization equations, which include attitude update, velocity, and position update.

3.1.1 Coordinate Systems

Coordinate reference frames need to be defined before processing inertial data. To this end, the inertial frame, Earth-Centred-Earth-Fixed (ECEF) frame, navigation frame, and body frame are defined in this section. Each frame is an orthogonal, right-handed coordinate system.

An inertial frame (i-frame) is a reference frame in which Newton's laws of motion apply, therefore it is not accelerating, but may be in uniform linear motion (Farrell 2008). The origin of inertial frame is the centre of the Earth, three axes are fixed with respect to the stars, as shown in Figure 3.1. x_i , y_i and z_i axes are defined in this figure, with x_i - axis pointing towards the mean vernal equinox, z_i - axis coincident with the Earth's polar axis, and y_i - axis is decided by the right-handed coordinate system.

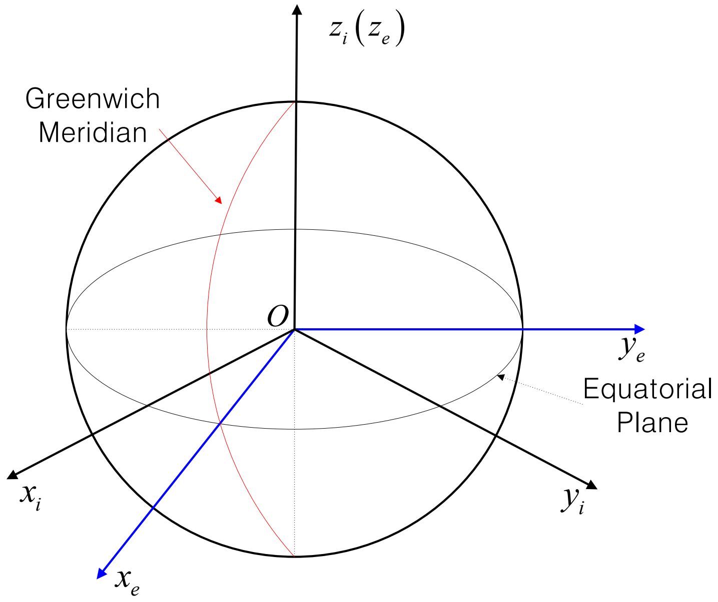

Figure 3.1: Illustration of Inertial Frame and ECEF Frame

The origin of ECEF frame (e-frame) is also the centre of the Earth, however, the axes are fixed with respect to the Earth compared to the inertial frame. x_e, y_e and z_e are defined in Figure 3.1, with x_e - axis pointing towards the intersection of the plane of the Greenwich meridian with the Earth's equatorial plane, z_e - axis coincident with the Earth's spin axis, and y_e - axis is decided by the right-handed coordinate system. The rotation rate of ECEF frame is $\omega_{ie} = 7.292115e^{-5} rad/s$ respect to the inertial frame for the WGS84 reference system (Savage 2000).

The navigation frame (n-frame) is a local geographic frame, also called local level frame. The origin of the navigation frame is the location of the navigation system, and the axes are aligned with the directions of north, east, and down. In this work, x_n - axis pointing towards the true north, y_n - axis pointing towards the east, and z_n - axis is decided by the right-handed coordinate system.

The body frame is defined by the orientation of the IMU axes. The origin of body frame is the centre of IMU, with x_b - axis pointing towards the right of the vehicle, y_b - axis pointing towards the front of the vehicle, and z_b - axis is decided by the right-handed coordinate system.

3.1.2 Coordinates Transformation

Coordinates transformation is used to transform a vector from one frame to another frame (Rogers 2003). Every vector has a distinct coordinate representation relative to a predefined reference frame and the vector's components described in one frame can be presented in another frame of arbitrary orientation with respect to the original frame by a transformation matrix. For example, a velocity vector can be represented by v^n or v^b, where the superscripts define the reference frames in which the vectors are represented, here, the navigation frame and body frame respectively. The representations of some special quantities also use subscripts to indicate the physical standing, for example, ω_{nb}^b indicates the angular velocity from body frame to navigation frame expressed in the body frame. Mathematically, the coordinate transformation is accomplished by sequential rotations from the original frame's axes to specific frame, which will be shown later. A transformation matrix is defined as C with a superscript indicating the destination frame and a subscript origin frame in this work. For example, C_n^b represents the rotation from

n frame to b frame, in so doing, the velocity vectors in navigation frame and body frame shown above are related as

$$v^b = C_n^b v^n \tag{3.1}$$

The most commonly used coordinate transformation (the transformation between ECEF frame and navigation frame) in navigation systems is introduced in this section. Some other transformations can be derived in the same way as this below.

The transformation between the ECEF and navigation frame can be performed by three consecutive rotations as shown in Figure 3.2, which are given by Equations (3.2), (3.3), and (3.4), respectively, where λ is vehicle longitude, L is vehicle latitude.

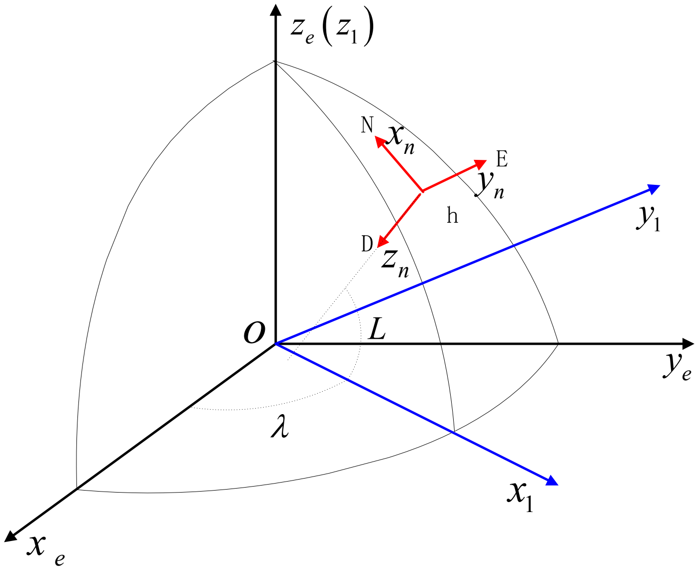

Figure 3.2: Illustration of Transformation from ECEF Frame to Navigation Frame

Step 1: Rotate by λ about z_e axis, from $x_e y_e z_e$ frame to $x_1 y_1 z_1$ frame

$$C_e^1 = \begin{bmatrix} \cos\lambda & \sin\lambda & 0 \\ -\sin\lambda & \cos\lambda & 0 \\ 0 & 0 & 1 \end{bmatrix} \tag{3.2}$$

Step 2: Rotate by L about y_1 axis, from $x_1y_1z_1$ frame to up-east-north frame (defined as 2)

$$C_1^2 = \begin{bmatrix} \cos L & 0 & \sin L \\ 0 & 1 & 0 \\ -\sin L & 0 & \cos L \end{bmatrix} \tag{3.3}$$

Step 3: Rotate by -90° about east axis, from up-east-north frame to north-east-down frame (defined as n in this work, navigation frame)

$$C_2^n = \begin{bmatrix} 0 & 0 & 1 \\ 0 & 1 & 0 \\ -1 & 0 & 0 \end{bmatrix} \tag{3.4}$$

And finally get the transformation matrix C_e^n between ECEF frame and navigation frame as

$$C_e^n = C_2^n C_1^2 C_e^1 = \begin{bmatrix} -\sin L\cos\lambda & -\sin L\sin\lambda & \cos L \\ -\sin\lambda & \cos\lambda & 0 \\ -\cos L\cos\lambda & -\cos L\sin\lambda & -\sin L \end{bmatrix} \tag{3.5}$$

3.1.3 Mechanization

The mechanization equations are used to get the position, velocity, and attitude increments of the vehicle from the IMU data. Mechanization can be conducted in any coordinate system, but in this work the navigation frame is used due to convenience. The attitude update, velocity update, and position update are each discussed in detail below.

Attitude update

The orientation of a body with respect to a reference frame is known as attitude (Titterton and Weston 2004), which is usually presented by the Euler angles, direction cosine matrix (DCM), or quaternions. A strapdown INS computes the orientation that is used to project the accelerations from the body frame to the navigation frame. After this, the velocity and position of the vehicle can be obtained. However, the initial values of attitude presents must be determined before the mechanization can be performed.

The quaternion approach is often preferred in the INS mechanization due to the linearity of quaternion differential equations, and the lack of singularities. Quaternion method takes advantage of the fact that Euler states can be represented as a single rotation about a single fixed vector, which is given by (Titterton and Weston 2004)

$$Q = \begin{bmatrix} q_0 & q_1 & q_2 & q_3 \end{bmatrix}^T \tag{3.6}$$

And the complex form is

$$Q = q_0 + q_1 i + q_2 j + q_3 k \tag{3.7}$$

There are four parameters in the quaternion vector, however, only three degree of freedom exists. More details about quaternion method are available in Kuipers (1998), Savage (2000), Farrell (2008). Quaternion update equation is given by

$$\dot{Q}_n^b = \begin{bmatrix} \dot{q}_0 \\ \dot{q}_1 \\ \dot{q}_2 \\ \dot{q}_3 \end{bmatrix} = \frac{1}{2} \begin{bmatrix} 0 & -\omega_{nbx}^b & -\omega_{nby}^b & -\omega_{nbz}^b \\ \omega_{nbx}^b & 0 & \omega_{nbz}^b & -\omega_{nby}^b \\ \omega_{nby}^b & -\omega_{nbz}^b & 0 & \omega_{nbx}^b \\ \omega_{nbz}^b & \omega_{nby}^b & -\omega_{nbx}^b & 0 \end{bmatrix} \begin{bmatrix} q_0 \\ q_1 \\ q_2 \\ q_3 \end{bmatrix} \tag{3.8}$$

where ω_{nb}^{b} : Angular velocity from body frame to navigation frame expressed in the body frame

Conversion from quaternion to DCM is

$$C_b^n = \begin{pmatrix} q_0^2+q_1^2-q_2^2-q_3^2 & 2\left(q_1q_2+q_0q_3\right) & 2\left(q_1q_3-q_0q_2\right) \\ 2\left(q_1q_2-q_0q_3\right) & q_0^2-q_1^2+q_2^2-q_3^2 & 2\left(q_2q_3+q_0q_1\right) \\ 2\left(q_1q_3+q_0q_2\right) & 2\left(q_2q_3-q_0q_1\right) & q_0^2-q_1^2-q_2^2+q_3^2 \end{pmatrix} \tag{3.9}$$

Velocity update

Before the velocity update, the specific force is introduced first. As discussed above, inertial navigation systems rely on the accelerometer outputs which can be integrated to provide the change of velocity and position (Titterton and Weston 2004). The navigation frame is usually used in navigation applications since it is more convenient than other frames. The specific force under the navigation frame is given by Equation (3.10) (Savage 2000), which includes the real acceleration in the navigation frame, the Earth gravity, and the Coriolis acceleration caused by the rotation of navigation frame and Earth.

$$f^n = \dot{v}^n + (2\omega_{ie}^n + \omega_{en}^n) \times v^n + g^n \tag{3.10}$$

where v^n : Vehicle velocity with respect to the navigation frame

ω_{ie}^n : Earth rotation rate with respect to the navigation frame

ω_{en}^n : Angular velocity between navigation frame and Earth frame with respect to the navigation frame

g^n : Gravity with respect to the navigation frame

× : Vector cross product

Rewrite Equation (3.10) and substitute $f^n = C_b^n f^b$ to get

$$\dot{V}_{ep}^n = C_b^n f^b - \left(2\omega_{ie}^n + \omega_{ep}^n\right) \times V_{ep}^n + g^n \tag{3.11}$$

Integrating Equation (3.11) returns the velocity update under navigation frame.

Position update

Position is the integration of the velocity, the position update is given by

$$\dot{L} = \frac{v_n}{R_N + h} \tag{3.12}$$

$$\dot{\lambda} = \frac{v_e}{(R_M + h)\cos L} \tag{3.13}$$

$$\dot{h} = -v_d \tag{3.14}$$

where L : Vehicle latitude

λ : Vehicle longitude

h : Vehicle height

The velocities shown above are in the navigation frame. R_N and R_M are radii of curvature along lines of constant latitude and constant longitude respectively, which are given by

$$R_N = \frac{a}{\left(1 - e^2 \sin^2 L\right)^{1/2}} \tag{3.15}$$

where a : Equatorial radius of Earth, which is 6378137 m under WGS84 coordinate system

e : Earth eccentricity, which is 0.081819 under WGS84 coordinate system

$$R_M = \frac{a\left(1-e^2\right)}{\left(1-e^2\sin^2 L\right)^{3/2}} \tag{3.16}$$

As discussed above, ten differential equations are used to describe the time evolution of navigation parameters in the INS, which include 4 quaternions, 3 velocities, and 3 positions. These differential equations can be numerically integrated separately. The Euler integration method and Runge-Kutta method can be employed to get the integration of the navigation parameters. Generally, for low dynamic applications, the Euler integration method is preferred due to the low computational load; however, in the high accuracy applications, a fourth-order Runge-Kutta integration is preferred to obtain the navigation solutions (Rosales and Colomina 2005).

Initialization

As stated above, inertial navigation systems require the initialization of the position, velocity, and attitude parameters (Farrell 2008). Three topics are of interest for initialization, including calibration, initialization, and alignment.

The calibration process is used to determine various inertial measurement errors, such as biases, scale factor errors, and axis non-orthogonalities. Before being used, the accelerometers and gyroscopes are initially calibrated in the laboratory or using a separate field test. The initialization process is used to determine the initial position and velocity of vehicle. Alignment is used to determine the orientation of the axes with respect to the reference axis system (Titterton and Weston 2004). There are two fundamental types of alignment: self-alignment and the alignment of a secondary system with the aid of a primary reference (Titterton and Weston 2004). This section is concerned with the self-alignment technique. A self-alignment is carried out based solely on the IMU outputs, and can be divided into coarse alignment and fine alignment. During the alignment process, the most difficult objective is to establish the initial azimuth.

The basic concept of coarse alignment is quite simple and straightforward. Coarse alignment takes advantage of the fact that Earth's gravity and rotation rate are constant and can be predicted at the given position (Rogers 2003). The angular velocity and specific force from inertial sensors are then compared to the theoretical values, and yield a reasonable estimate of initial attitude. Usually coarse alignment is conducted in the static scenario. In the static scenario, the gravity vector is used to determine the pitch and roll as given by (Farrell 2008)

$$\begin{bmatrix} \phi \\ \theta \end{bmatrix} = \begin{bmatrix} \arctan 2\left(f_y, f_z\right) \\ \arctan 2\left(f_x, \sqrt{f_y^2 + f_z^2}\right) \end{bmatrix} \tag{3.17}$$

where f is under the body frame.

After the coarse levelling, the estimated azimuth is given by

$$\psi = -\tan^{-1}\left(\frac{\omega_{ibx}^{b}}{\omega_{iby}^{b}}\right) \tag{3.18}$$

However, the sensor accuracy requirement behind this method is that the gyroscope accuracy must be accurate enough to sense the rotation of Earth, which cannot be accomplished by commercial micro electro-mechanical systems (MEMS) sensors.

The fine alignment process is used to refine the attitude obtained in the coarse alignment process, which is based on the INS error propagation equation (see Appendix A) and extended Kalman filter estimate. Fine alignment process will be discussed in the GNSS/INS integration section. The misalignment is estimated during the fine alignment process, and also some IMU errors.

3.2 Integration Strategies Overview

GNSS/INS integrated navigation systems take advantage of the complementary characteristics of the two different systems. The combined system offers a significantly increased performance in terms of accuracy and robustness compared to the standalone usage of either system (Wendel et al 2004). GNSS/INS integration strategies are based on the optimal estimation theory. Kalman filters are widely employed to merge the data of the navigation sensors. The differences between the INS and GNSS are processed in the Kalman filter to estimate the growing position and velocity errors over time in the INS. Generally, there are three strategies employed to integrate GNSS and INS data together, which are normally classified as loosely-coupled, tightly-coupled, and ultra-tightly-coupled (Petovello et al 2003). Usually a feedback Kalman filter is used to improve the integration performance. In this approach, the estimated errors are used to reset the GNSS and INS parameters. Continuous correction (over time) assures the long-term accuracy of INS system, as well as calibrates the IMU errors.

In the GNSS/INS integration system used in this work, the IMU is rigidly mounted to the vehicle and the offset to the GNSS antenna, namely, the lever-arm, should be measured before the mission. Figure 3.3 shows the lever-arm between the GNSS antenna and IMU. The required lever-arm accuracy should be better than 1 cm (Petovello 2003).

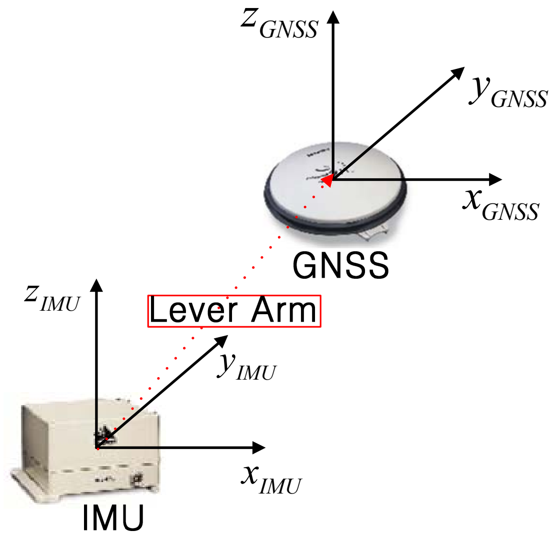

Figure 3.3: Illustration of Lever-Arm (Modified from NovAtel)

3.2.1 Loosely-Coupled Integration

GNSS and INS operate independently in the loosely-coupled strategy, which is relatively easy to implement compared to the other strategies discussed below. In the loosely-coupled strategy, position and velocity from GNSS and INS are used as measurements to a Kalman filter to aid the INS (Petovello 2003). In so doing, the position and velocity from GNSS are directly compared to the INS outputs, as shown in Figure 3.4.

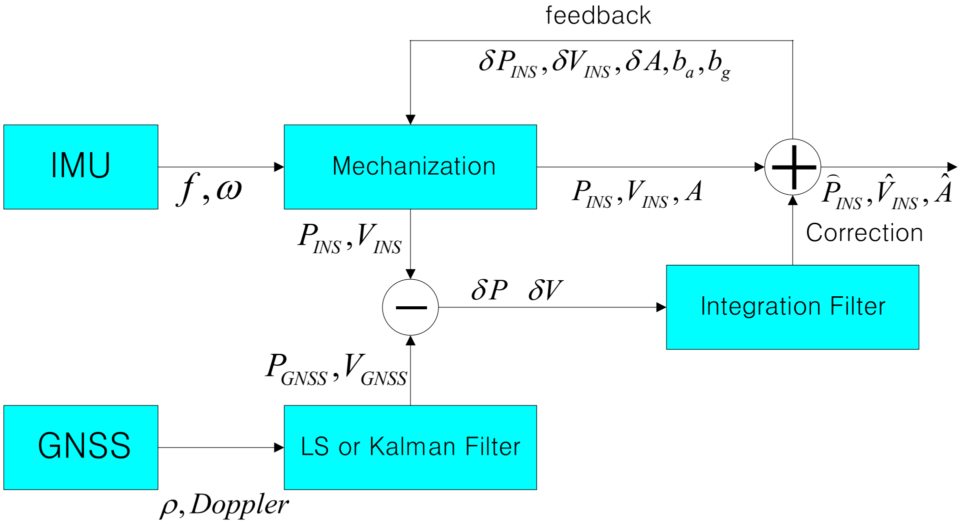

Figure 3.4: Loosely-Coupled Integration

GNSS position and velocity are obtained by least-squares or Kalman filtering. The INS error model shown in Appendix A is used in the integration filter to estimate the errors that occur in the mechanization. Generally, the system model for the loosely-coupled integration consists of nine error states which include three position errors, three velocity errors, and three attitude errors. However, due to the IMU sensor errors and clock errors in the GNSS system, the number of states is expanded in the integration filter. In the fine alignment process, the same strategy is used to estimate the orientation errors.

The advantages of loosely-coupled integration is that it is relatively easy to implement, and GNSS and INS operate independently which means that one system cannot be corrupted by the other. However, the drawback is that, if a Kalman filter is employed in the GNSS receiver, the position and velocity measurements are time-correlated which can cause performance degradation in the integration Kalman filter (Godha 2006). And in the incomplete constellation cases, for example, if the number of available satellites is not sufficient to get the position and velocity measurements, the GNSS information has to be ignored completely in the loosely-coupled system, in this situation, the navigation errors of INS grow unbounded.

3.2.2 Tightly-Coupled Integration

In the tightly-coupled integration system, the pseudorange and carrier Doppler from the GNSS tracking loop are used directly in the Kalman filter, as shown in Figure 3.5.

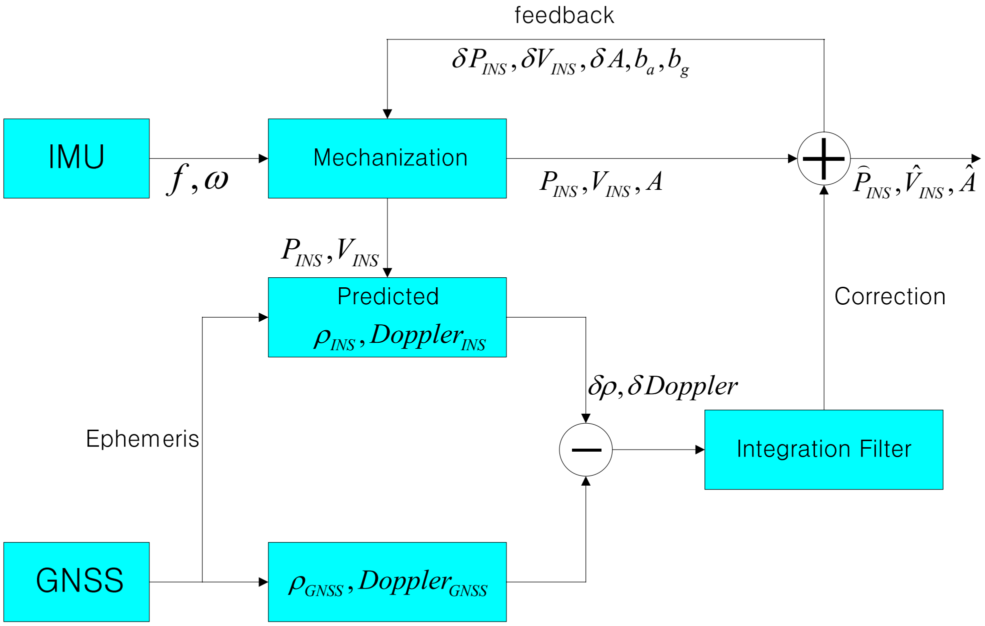

Figure 3.5: Tightly-Coupled Integration

Tightly-coupled integration uses the same state model as loosely-coupled integration, the difference is the Kalman filter measurements. Unlike for a loosely-coupled system which requires that at least four satellites be tracked in order to get the GNSS position and velocity solution, the number of tracked satellites is not important in the tight integration case. The major drawback of tightly-coupled system is that the computational load increases.

3.3 Ultra-Tight Integration

For a GNSS-only receiver, a traditional PLL estimates the Doppler and clock errors of the incoming signal during the tracking process (Alban et al 2003). However, the performance of the tracking loop is degraded under dynamic scenarios. If these parameters can be estimated externally, such as from inertial sensors, they can be used to aid the tracking loop. A conventional ultra-tight system uses separate tracking loops for each satellite channel as shown in Figure 3.6, and the INS outputs provide the dynamic reference for the GNSS signal integration inside the receiver correlators. Correspondingly, the local replicas are adjusted for dynamic changes using the inertial aiding (Soloviev et al 2004). Ultra-tight receiver offers numerous advantages in terms of robustness, under high dynamic, as well as carrier tracking performance.

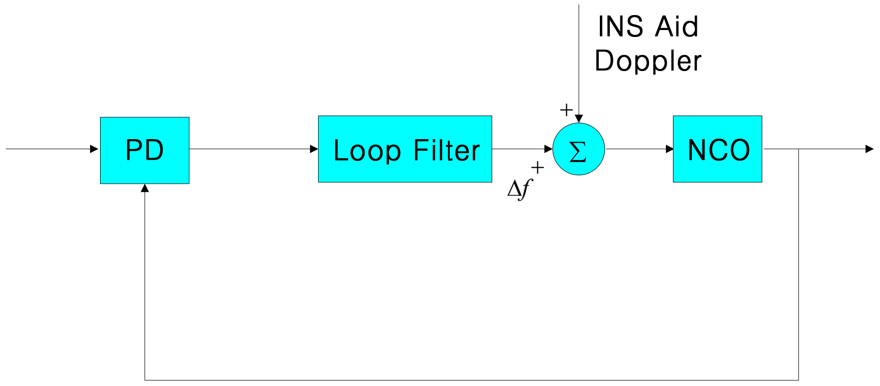

Figure 3.6: Standard Ultra-Tight Integration

In the standard PLL, the output of the loop filter is the estimated carrier Doppler, as shown in Chapter 2. However, in the ultra-tight receiver, with the aiding of the external INS, the output of loop filter is the Doppler error between the true carrier Doppler and the INS predicted Doppler. The ultra-tight configuration shown above offers advantages over the traditional structure in term of noise suppression and tracking bandwidth. The signal dynamics are tracked with the bandwidth provided by the INS, which means that the loop filter bandwidth used to track the Doppler error can be reduced. Loop filter bandwidth depends on the Doppler error from external aiding. To this end, the Doppler accuracy depends on the IMU quality and different kinds of IMU can provide different aiding performance.

A vector-based ultra-tight scheme is preferred in the receiver used in this work (Petovello 2003). In the vector-based receiver, the NCO is controlled by the navigation filter, and solely determined on the basis of position, clock, and line-of-sight (LOS) estimation, which means that the standard loop filter shown in Figure 3.6 does not exist anymore. The benefits of vector-based receiver are already shown in Chapter 2. Table 3-1 shows the specification of the tactical grade IMU (HG1700) used in this work (Godha 2006).

Table 3-1: HG1700 Specifications

	Accelerometers	Gyroscope
In run bias	1 mg	1 deg/h
Scale factor	300 ppm	150 ppm
Random walk	2.16 e-6 $g/\sqrt{Hz}$	7.5 deg/$h/\sqrt{Hz}$

The details of ultra-tight Kalman filter will be provided in the Chapter 5.

CHAPTER FOUR: PIECE-WISE CONTROL METHOD

This chapter looks at the performance of the piece-wise control method proposed in this work. The motivation of piece-wise control is to reduce the transition time during the carrier phase reacquisition process, thereby providing more phase measurements for high-accuracy positioning applications. In a standard receiver architecture, generally speaking, the carrier loop starts with acquisition, then transitions to a FLL, then to a FLL-assisted-PLL, and finally to a PLL. During the reacquisition process, this procedure is restarted, albeit often with smaller search spaces.

However, given the reduced search space, other approaches may be used to provide a more rapid transition to carrier phase tracking. For example, the relationship between rise time, overshoot, natural frequency, and damping ratio has not been investigated in previous work during the reacquisition process. In the GNSS tracking loop, a large damping ratio can reduce the overshoot of the transition process, and a large natural frequency will result in a smaller rise time. Therefore, if the damping ratio and natural frequency are increased in the loop filters during the carrier phase reacquisition process, a smaller convergence time and overshoot is expected. With this in mind, a piece-wise control approach has been proposed in this work. The approach divides the reacquisition and tracking process into separate periods each with different natural frequencies and damping ratios. It is noted that the differences among a FLL and a PLL are filter orders and specific loop filter parameters; in other words, the same types of loop filter are employed in both frequency tracking and phase tracking, which means that the piece-wise method can be used both in the frequency tracking process and the phase tracking process.

4.1 Proposed Metrics

Before presenting the new method, the metrics used to evaluate the algorithm is first presented. Generally, frequency lock indicator (FLI) and phase lock indictor (PLI) can be used to evaluate the performance of frequency tracking and phase tracking quality respectively. FLI (Mongredien et al 2006) and PLI (Van Dierendonck 1995) are the function of frequency error, phase error, and integration time. The FLI is given by

$$FLI = \cos\left(4\pi\delta f T_c\right) \tag{4.1}$$

where T_c : Integration time

δf : Frequency error in the tracking loop

For example, for a 20 ms integration time, $FLI = 0.9$ means that the frequency error in the frequency tracking loop is 1.8 Hz. The PLI is given by

$$PLI = \cos\left(2\delta\varphi\right) \tag{4.2}$$

where $\delta\varphi$: Phase error in the tracking loop

For example, $PLI = 0.9$ indicates the phase error in the phase tracking loop is 13 degrees.

Generally, the transitions between a FLL and a PLL are based on the FLI and PLI values. For example, a loss of phase lock is declared if PLI is smaller than 0.5 (O'Driscoll et al 2009), which means that the phase error in the PLL is larger than 30 degrees. At this point, the receiver transitions from a PLL to a FLL. In the carrier phase reacquisition process, the Doppler and carrier phase transition time have been of particular interests. As mentioned above, FLI and PLI can be used to evaluate the tracking errors. However, usually a filter is used in the PLAN group GSNRx^{TM} software receiver to obtain the FLI and PLI. In so doing, a delay is introduced. Therefore, the use of FLI and PLI is not effective to evaluating the transition time. In order to avoid the delay phenomenon in the transition time evaluation process, the primary metrics used in this work are Doppler jitter (Borio et al 2009) and phase jitter (Gebre-Egziabher et al 2003).

The evaluation process for the frequency transition time is conducted by the following two steps, polynomial fitting and Doppler jitter calculation. During the first step, a polynomial fitting is employed to obtain the interpolation of the tracking results. The polynomial fitting equation is given by

$$y_k = p_0 + p_1 t_k + \cdots + p_{n-1} t_k^{n-1} + p_n t_k^n \tag{4.3}$$

where n : Polynomial order

p_i : Polynomial coefficients, from p_0 to p_n

Essentially, the coefficients of a polynomial are determined in a least-squares sense. Generally a first-order (linear) polynomial is employed in this work because the Doppler change during the transition process (usually less than 1 s) is small, which means that a first-order fit is accurate enough and will be shown later. However, a second-order polynomial would be preferred for a longer transition process. The tracking errors and Doppler jitter are calculated in the second step, tracking errors are given by

$$\varepsilon_k = z_k - y_k \tag{4.4}$$

where z : Observed tracking results

y : Polynomial results

Doppler jitter is a function of signal power, loop filter noise bandwidth, and integration time, and is given mathematically by (Borio et al 2009)

$$\sigma_f = \frac{1}{T_c}\sqrt{\frac{B_n}{C/N_0}\left(1+\frac{1}{2T_cC/N_0}\right)} \tag{4.5}$$

where B_n : Loop filter noise bandwidth

T_c : Integration time

C/N0 : Carrier to noise density

However, a more practical way is used in this work to obtain the Doppler jitter, which is given by

$$\sigma_f = \sqrt{\frac{\sum_{k=1}^{n}\varepsilon_k}{n-1}} \tag{4.6}$$

where ε_k : Tracking error

n : Number of samples

Different from the frequency transition time assessment, the polynomial fitting does not apply to the phase transition time analysis. The reason for this is that generally the carrier phase increments over integration time (1 ms for example) are in the order of several cycles. Because of this, high accuracy polynomial fitting cannot be obtained. Fortunately, since the loss of phase lock is manually induced in the phase tracking loop, the carrier phase outputs without a manually induced loss of phase lock can be used as a reference. In so doing, the phase errors can be obtained. Moreover, the relationship between the

C/N_0 and loop filter bandwidth is shown in Gebre-Egziabher (2003), which can be used as the threshold to determine the phase transition time.

To this end, the transition time is herein defined as the time required for the Doppler error (phase error) to become smaller than the 3σ Doppler jitter (phase jitter) over the span of 100 continuous epochs. This approach was selected empirically and seemed like a reasonable value based on the results shown later. More specifically, the time of first epoch after the 100 continuous epochs mentioned above (relative to when the signal reacquisition process stared) is the transition time.

In order to get the baseline performance for the piece-wise control method, a simulation is introduced in this work where a manual loss of signal lock is created in the software receiver, and the carrier frequency and carrier phase are also reset manually for the local replica signal. In so doing, the transition process assessments for different initial frequency errors and different initial phase errors are possible.

4.2 Piece-wise FLL Assessment

Piece-wise FLL is used to reduce the frequency transition time in the reacquisition process, and enable a PLL start with a small initial frequency error. The transition processes for different initial frequency errors are already shown in the Chapter 2, as well as the tracking loop performances of different natural frequencies and damping ratios. In this section, the performance of piece-wise FLL is assessed with a maximum initial frequency error of 200 Hz, which is assumed in the Chapter 2. The approach divides the tracking process into separate periods each with different natural frequencies and damping ratios. The performance of such an approach is evaluated in terms of the time required to attain specified frequency tracking qualities (Doppler jitters).

This section will discuss the method of frequency polynomial fitting, followed by parameter tuning of the piece-wise tracking loop, and finally the performance assessment of the piece-wise FLL method for different scenarios.

4.2.1 Polynomial Fitting

Polynomial fitting is employed here to evaluate the FLL transition process, the definition of transition time is already shown in the proposed metrics section. Without loss of general, different satellites with different received signal power have been assessed. Here take PRN 31 (C/N_0 is 51 dB/Hz) for example to illustrate how to obtain the Doppler jitter and the frequency tracking transition time, the given natural frequency is 10 Hz, damping ratio is 0.707, and a second-order loop filter is employed. Generally, the Doppler outputs without manually induced loss of signal lock can be used to obtain the polynomial fitting results. However, the FLL reaches the steady-state after 1 s; to this end, the tracking results thereafter can also be used to obtain the polynomial fitting for the FLL outputs, as well as the Doppler jitter. As discussed earlier, a first-order polynomial fitting is sufficient to fit the FLL results after reaching steady-state in this case, which is given by

$$f_k = p_0 + p_1 t_k \tag{4.7}$$

where p_0, p_1 : Polynomial coefficients

The red curve in Figure 4.1 shows the transition process after loss of signal lock, with an initial frequency error of 200 Hz. The green curve represents the polynomial fitting of the tracking results, the differences between the FLL outputs and polynomial fitting are defined as the tracking errors ε, which is shown in Equation (4.4).

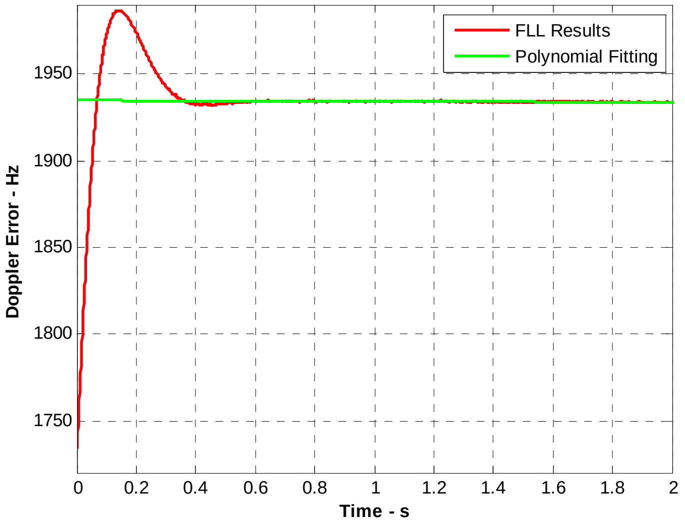

Figure 4.1: Polynomial Fitting for the FLL Transition Process

The Doppler jitter is then given by Equation (4.6) which returns 0.19 Hz in this case. Notice that only the tracking errors after reaching steady-state are used in Equation (4.6). Figure 4.2 shows the same results as Figure 4.1 but with the scale of y-axis is from -1 Hz to 1 Hz in order to show the transition time more clearly. The 3σ Doppler jitter used as the threshold to determine the FLL transition time (blue line) is also shown.

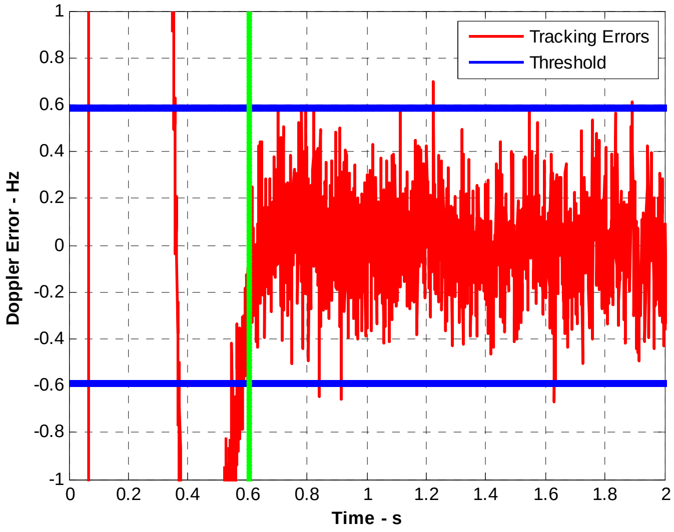

Figure 4.2: Frequency Errors during the FLL Transition Process

for the PRN 31

It is observed that for a 200 Hz initial frequency error, the transition time is 0.6 s (green line).

4.2.2 Parameters Tuning

Different natural frequencies and damping ratios have different transition processes and are already shown in Chapter 2. From this, a problem arises in finding tracking loop parameter values during the reacquisition process in order to meet the fast carrier phase reacquisition requirement. Also, how best to control the transitions between different loop filter parameters are of interest in this section. Generally, two types of logic can be employed in the piece-wise method to control the parameter transitions, the first one is time-based logic, and the second one is FLI-based (PLI-based) logic. In the time-based logic, a fix period is used to control the transition between the piece-wise method and general tracking loop (i.e. 10 Hz natural frequency and 0.707 damping ratio for standard FLL). In the FLI-based (PLI-based) logic, the transition is controlled by the FLI (PLI) value since the FLI (PLI) is a function of frequency (phase) error. However, as shown in the proposed metrics section, FLI (PLI) is not effective to evaluate the transition time, to this end, the time-based logic is used in this work.

Different tracking loop parameters were assessed during the tuning process. Specifically, the natural frequency range was from 8 Hz to 80 Hz with a step of 4 Hz, and the damping ratio range was from 0.707 to 8.4 with a step of 0.707. Furthermore, since a time-based logic was ultimately adopted, different piece-wise intervals (i.e., intervals with constant parameters) were ranged from 10 ms to 80 ms with a step of 10 ms. Table 4-1 shows the specific parameter sets of interest, as they give an idea of how to conduct the parameters tuning. The first parameter set is used to show the performance of increased natural frequency compared to the general parameter set; the second parameter set is used to show the performance of larger damping ratio and longer piece-wise control period; the third and forth parameter sets are used to show the performance of even larger natural frequencies and damping ratios.

Table 4-1: Different Parameter Sets for the Piece-Wise FLL Parameters Turning

Parameter Sets	Natural Frequency	Damping Ratio	Piece-Wise Epochs
1	$\omega_n = 30$ Hz	$\xi = 0.707$	20 ms
2	$\omega_n = 30$ Hz	$\xi = 1.414$	80 ms
3	$\omega_n = 60$ Hz	$\xi = 5.6$	20 ms
4	$\omega_n = 80$ Hz	$\xi = 8.4$	20 ms

Figure 4.3 shows the transition process for the first parameter set of 200 Hz initial frequency error. Comparing Figure 4.2 and Figure 4.3 shows that the rise time is reduced by the larger natural frequency while holding damping ratio the same as the general values.

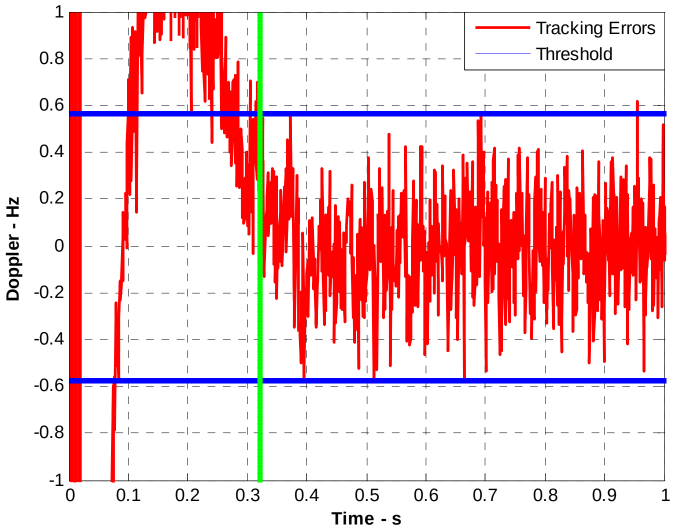

Figure 4.3: Frequency Transition Process Zoomed in

for the First Parameter Set of 200 Hz Initial Frequency Error

The same threshold (Doppler jitter) is employed in all cases as shown in Figure 4.2, this is due to the fact that they have the same steady-state behaviours. The transition time for 200 Hz initial frequency error is 0.32 s and is shown in this figure (green line). However, Figure 4.3 also shows that the overshoot is still relatively large after 20 epochs of the piece-wise period. This should be reduced by further increasing the piece-wise parameter values in the tracking loop. Figure 4.4 shows the performance of the second parameter set, where the damping ratio is increased to 1.414, and piece-wise period is increased to 80 epochs.

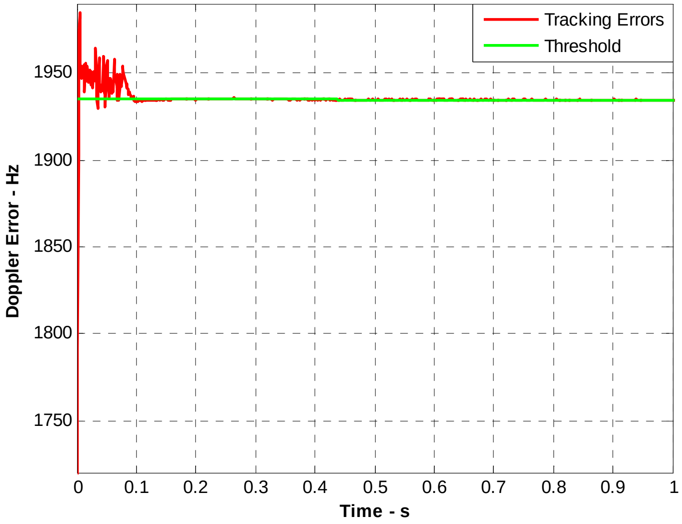

Figure 4.4: Frequency Transition Process and Polynomial Fitting for the Second Parameter Set

The drawback of the piece-wise method with longer piece-wise control period however is that the tracking noise during the piece-wise period is obviously larger than the general tracking loop, as shown in Figure 4.4. This suggests that it is better to reduce the overshoot as soon as possible by using an even larger natural frequency and (or) damping ratio, but not longer piece-wise period. Figure 4.5 shows the performance of the third parameter set.

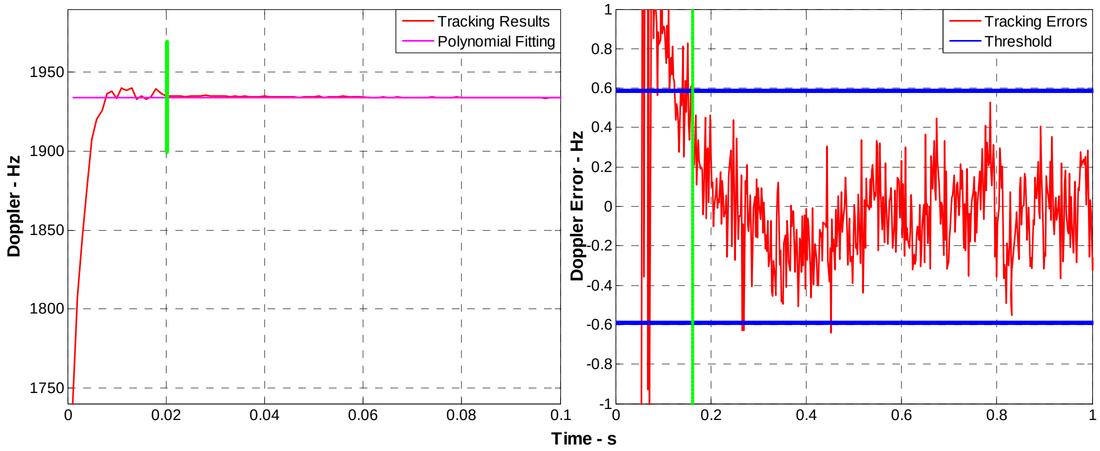

Figure 4.5: Frequency Transition Process and Zoomed in for the Third Parameter Set

Figure 4.5 shows a better transition process compared to the first two parameter sets, the remaining frequency error at the last piece-wise epoch is smaller than 2 Hz (green line, left-hand figure). After that, the standard natural frequency and damping ratio tracking loop reduces the tracking noise. The green line in the right-hand figure shows the transition time (0.16 s). Notice that the scale of the x-axis in the left-hand figure is different from the right-hand figure.

The first three parameter sets show that the transition times are reduced by increasing the parameter values, which are as expected since larger natural frequency and damping ratio will reduce the rise time and overshoot of the control system. However, given the metric in this section, further increasing the parameter values did not yield any additional benefits, since larger parameter values also increase the noise in the tracking loop. The performance of the forth parameter set is shown in Figure 4.6.

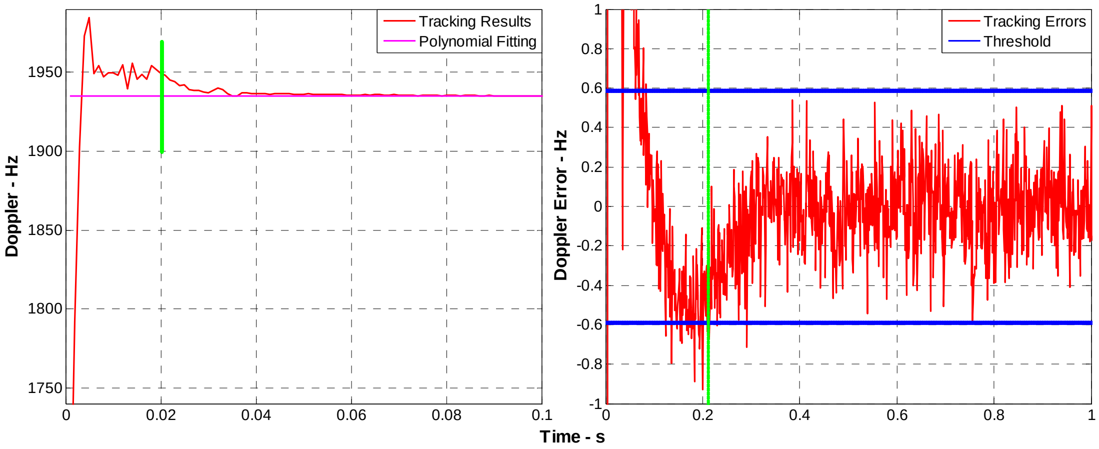

Figure 4.6: Frequency Transition Process and Zoomed in for the Forth Parameter Set

Figure 4.6 shows that the frequency error after the piece-wise period is larger than the third parameter set, the remaining frequency error of the forth parameter set is 15 Hz. This is because the tracking noise is increased by the large natural frequency and damping ratio values. The right-hand figure shows that the transition time is 0.22 s.

The simulation results show that a trade-off between transition time and tracking noise should be made for the piece-wise control method. To this end, the third parameter set is chosen as the proper parameter set. After the proper natural frequency and damping ratio are obtained, the piece-wise method performance is assessed with different initial frequency errors. Figure 4.7 shows the performance of the standard architecture, which is already shown in Chapter 2. Figure 4.8 shows the transition process of the piece-wise architecture, where the time-based logic is employed. In order to observe the transition process more clearly, the bottom plot shows the zoomed in version of each plot.

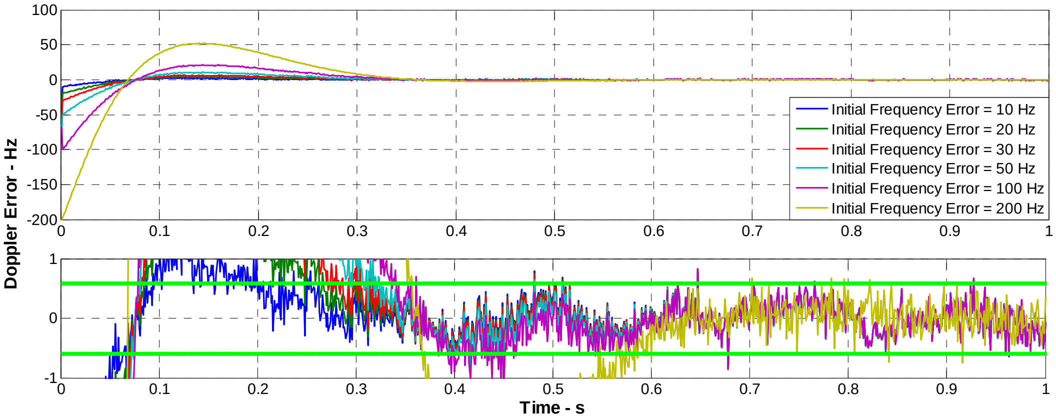

Figure 4.7: Transition Processes of Different Frequency Errors in the Standard FLL Architecture (bottom plot is a zoomed in version of the top plot)

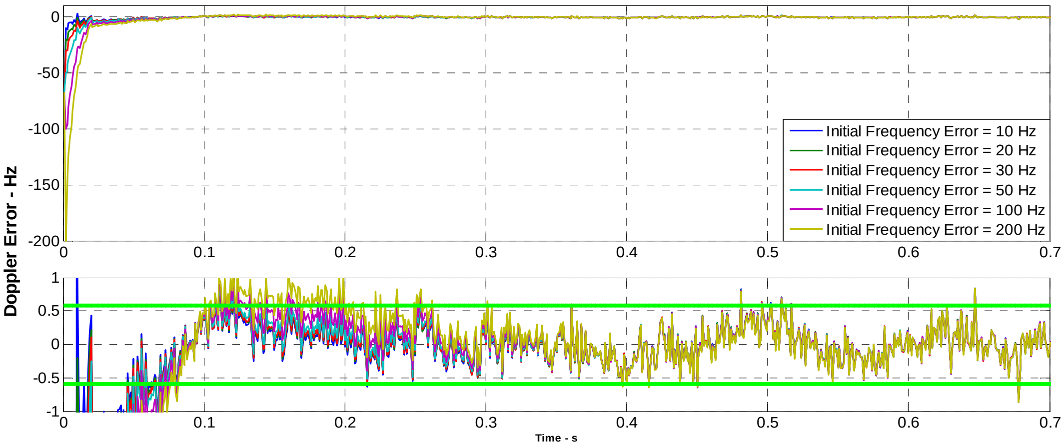

Figure 4.8: Transition Processes of Different Frequency Errors in the Piece-Wise FLL Architecture (bottom plot is a zoomed in version of the top plot)

As should be obvious, a smaller transition process is obtained by using the piece-wise FLL architecture as shown in Figure 4.8. Table 4-2 summarizes the transition times for different initial frequency errors using the standard and piece-wise architectures respectively. In nearly all cases, the piece-wise method produces a two- to three-fold improvement in transition time.

Table 4-2: Standard FLL and Piece-Wise FLL Comparison

Initial Frequency Error	Transition Time for Standard FLL	Transition Time for Piece-Wise FLL
10 Hz	0.24 s	0.12 s
20 Hz	0.27 s	0.13 s
30 Hz	0.31 s	0.13 s
50 Hz	0.35 s	0.18 s
100 Hz	0.51 s	0.19 s
200 Hz	0.59 s	0.24 s

Nine other open-sky loss of signal lock scenarios were also conducted to evaluate the performance of piece-wise FLL method. The loss of locks were manually set at every 5 seconds, and the C/N_0 ranged from 49 dB/Hz to 51 dB/Hz among all the cases. Figure 4.9 shows the transition process of 200 Hz initial frequency error for these ten simulations.

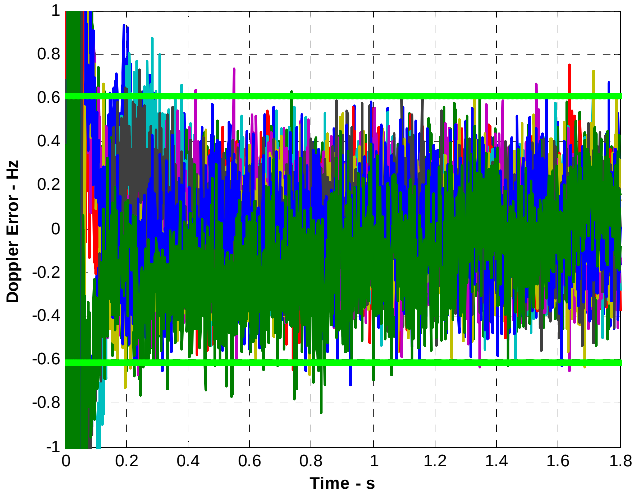

Figure 4.9: Transition Process of 200 Hz Initial Frequency Errors for Ten Different Loss of Signal Lock Scenarios (each line corresponds to a different loss of lock)

Figure 4.10 shows the transition times for all these ten simulations, the mean value and standard deviation are 0.21 s and 0.05 s, respectively.

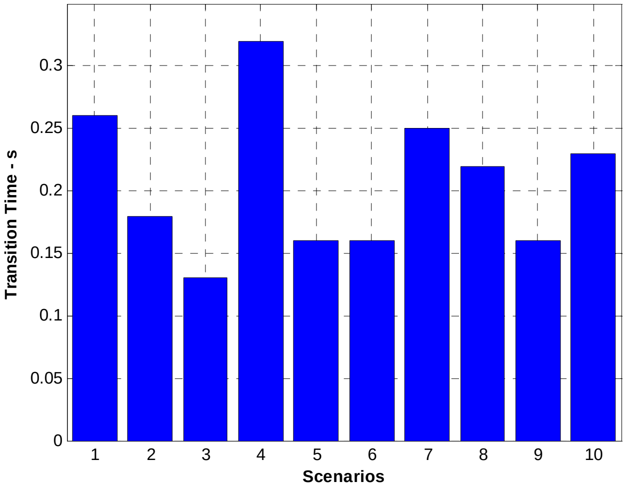

Figure 4.10: Transition Time Summary for Ten Different Loss of Signal Lock Scenarios

The drawback of time-basic logic is also shown in this plot, it is observed that the transition time for the forth scenario is 0.32 s, which is much larger than the mean value (0.21 s). The reason for this is due to the fact that a 20 ms piece-wise period is not long enough to reduce the initial frequency error. After the 20 ms period the standard PLL starts with a relatively larger frequency error. Table 4-3 shows the transition time summary for different initial frequency errors, the same as the 200 Hz initial frequency error case, 10 simulations are conducted for each initial frequency error.

Table 4-3: Piece-Wise FLL Method Transition Time Summary for 10 Simulations

Initial Frequency Error	Mean of Transition Time	STD of Transition Time
10 Hz	0.09 s	0.02 s
20 Hz	0.11 s	0.04 s
30 Hz	0.12 s	0.03 s
50 Hz	0.17 s	0.03 s
100 Hz	0.19 s	0.05 s
200 Hz	0.21 s	0.05 s

After the piece-wise FLL assessment in the open-sky scenario, PRN 14 is selected to evaluate the transition process under the weak signal scenario. The C/N_0 of the received signal is 40 dB/Hz. Figure 4.11 show the standard FLL performance for a 100 Hz initial frequency error under the weak signal scenario. It is noted that the frequency tracking noise is increased after reaching steady-state. The reason for this is due to the degraded signal power for PRN 14, this means that the threshold used to define the transition time is also increased. By using Equation (4.6), the threshold obtained for PRN 14 found to be 1.8 Hz.

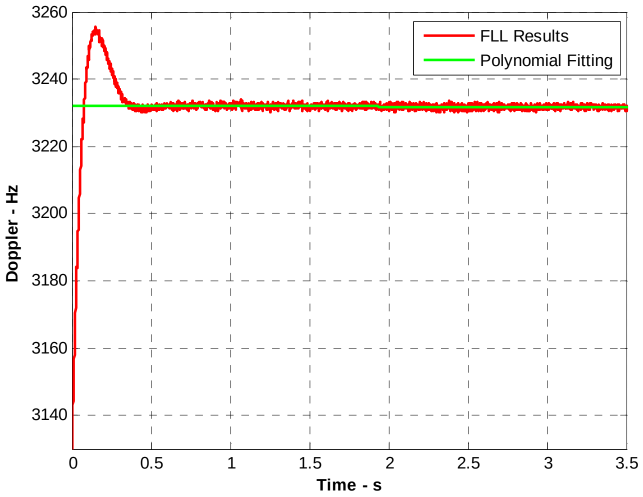

Figure 4.11: Frequency Transition Process and Polynomial Fitting for PRN 14 with 100 Hz Initial Frequency Error

Figure 4.12 shows the piece-wise FLL performance.

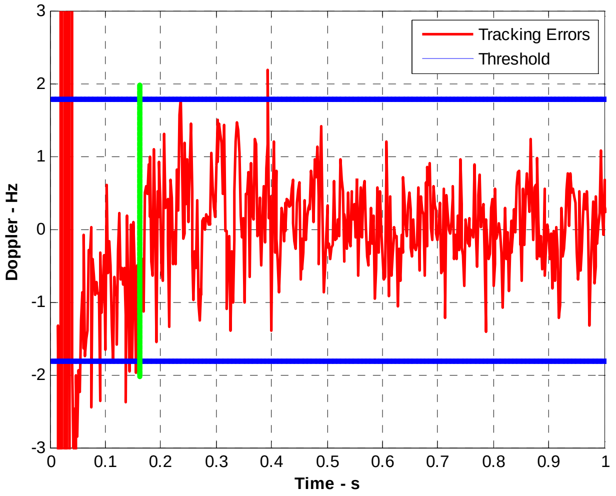

Figure 4.12: Piece-Wise FLL Transition Process Zoomed in for PRN 14

It is shown that the transition time for the weak signal satellite (0.17 s) is almost the same as the strong signal satellite (PRN 31, 0.19 s). These results suggest that the transition time is only a function of the loop filter parameter values.

4.3 Piece-wise PLL

The piece-wise FLL performance shown above suggests that the piece-wise method can reduce the frequency transition time during the reacquisition process. To this end, the proper parameter set obtained from the piece-wise FLL section can also be used in the second-order piece-wise PLL (since FLL and PLL use the same type of loop filter). Figure 4.13 and Figure 4.14 show the transition process of different initial phase errors for the standard PLL and piece-wise PLL respectively.

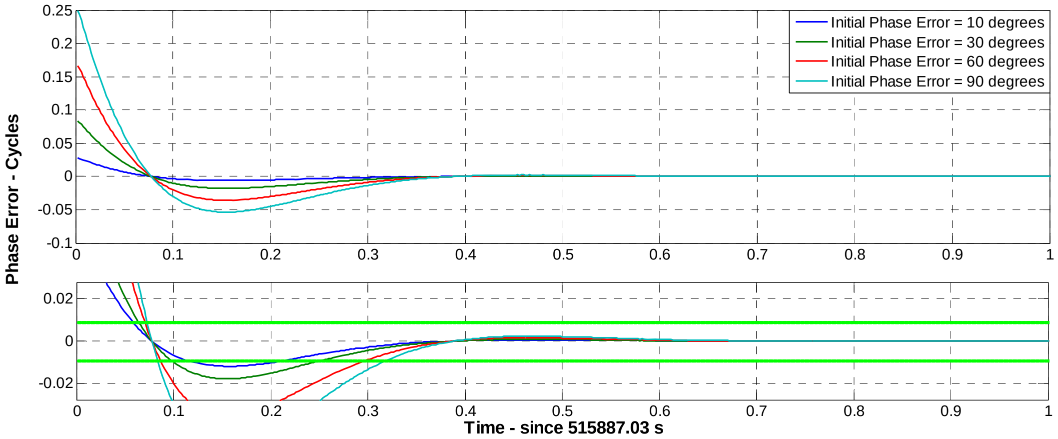

Figure 4.13: Transition Process of Different Phase Errors for the Standard PLL (bottom plot is a zoomed in version of the top plot)

The phase jitter from Gebre-Egziabher (2003) is used as the threshold to determine the phase transition time where the total phase jitter is smaller than 2 degrees for a signal with a C/N_0 of 50 dB-Hz scenario.

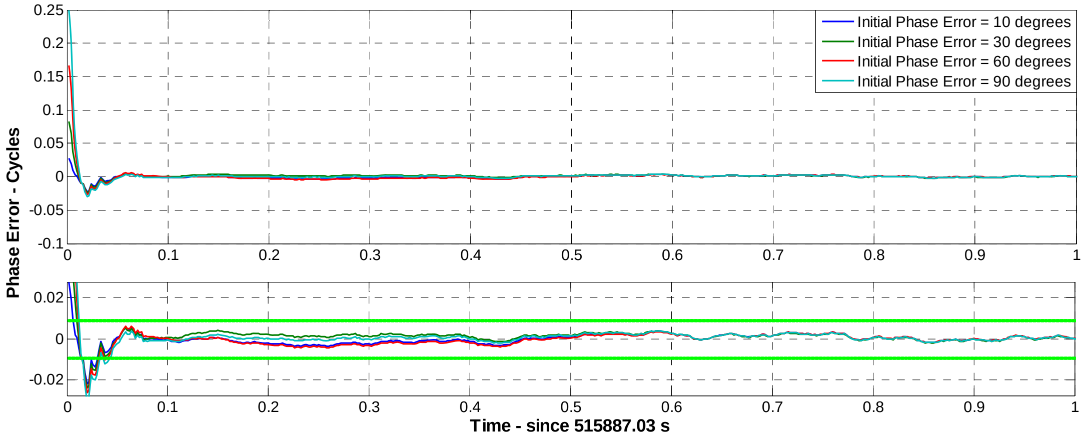

Figure 4.14: Transition Process of Different Phase Errors for the Piece-Wise PLL (bottom plot is a zoomed in version of the top plot)

The comparison between standard PLL and piece-wise PLL is summarized in Table 4-4, again, the improvement with the piece-wise approach is noticeable with a four- to five-fold improvement in all cases.

Table 4-4 Standard and Piece-Wise PLL Comparison

Initial Phase Error	Transition Time Standard	Transition Time Piece-Wise
10 degrees	0.21 s	0.04 s
30 degrees	0.24 s	0.04 s
60 degrees	0.29 s	0.04 s
90 degrees	0.32 s	0.05 s

Given the above, a piece-wise FLL followed by a piece-wise PLL is recommended to reacquire the GNSS signal more quickly. In this way, the piece-wise FLL is used to reduce the frequency error in the tracking loop, and then the carrier phase error is reduced by the piece-wise PLL. For a 200 Hz initial frequency error and 90 degrees initial phase error case, the transition time is reduced from 0.91 s (0.59 s for FLL and 0.32 s for PLL) to 0.25 s (0.21 s for piece-wise FLL and 0.04 s for piece-wise PLL), which means that more carrier phase observations are available after employing piece-wise control methods.

The same as piece-wise FLL method, nine other open-sky loss of signal lock scenarios are also conducted to evaluate the performance of piece-wise PLL method by employing the same proper loop filter parameters, the loss of locks are manually set at every 5 seconds.

Table 4-5 Piece-Wise PLL Method Transition Time Summary

Initial Phase Error	Mean of Transition Time	STD of Transition Time
10 degrees	0.03 s	0.01 s
30 degrees	0.04 s	0.01 s
60 degrees	0.03 s	0.01 s
90 degrees	0.04 s	0.01 s

4.4 Directly Piece-Wise PLL

Section 4.2 and section 4.3 show the performance of piece-wise approach, the approach above combines the piece-wise FLL and piece-wise PLL together, in so doing, a smaller transition process is achieved compared to the standard PLL. However, remember that the transition process in the PLL is used to reduce both frequency error and phase error in the phase tracking loop, an interesting question arises if a PLL can be used directly during the reacquisition process.

The pull-in ability of a standard PLL is assessed in this section. Key parameters of interests are the loop filter pull-in range and pull-in time. Based on the initial frequency analysis section, the maximum frequency uncertainty after loss of signal lock can reach 200 Hz. The definitions of pull-in range and pull-in time are shown in Best (2004). A pull-in range is defined as the range where a PLL will always become locked, but the pull-in process can be rather slow. The pull-in time is the time a PLL needs to become phase locked during the pull-in process. The PLL's pull-in range is an important parameter in practical applications. In the analog applications, the PLL pull-in range is a function of filter natural frequency and damping ratio. The ability depends on the types of phase detector and loop filters used in the PLL (Best 2004). The PLL has a wider pull-in range for a larger natural frequency; similarly, larger damping ratio can also increase the pull-in range.

For an active proportional-integration (PI) loop filter, which is the case in the software receiver (Best 2004), the pull-in range is given by

$$\omega_P \approx \infty \tag{4.8}$$

It is shown that the pull-in range is infinity for this type of loop filter, which means that the PLL pulls in under any conditions. The pull-in time is given by

$$T_P \approx \frac{1}{\pi^2}\frac{\Delta\omega_0^2}{\xi\omega_n^3} \tag{4.9}$$

where $\Delta\omega_0$: Initial frequency error

ω_n : Loop filter natural frequency

ξ : Loop filter damping ratio

However, generally this is not the case in the software-based PLL, the reason for this is due to the integration process being employed in the software receiver. The pull-in ability is changed by the averaging process. For a small natural frequency and damping ratio loop filter, a large initial frequency error cannot be pulled in. In this section, the pull-in ability is assessed by processing the real data.

Best (2004) shows that different natural frequencies and different damping ratios have different pull-in performance. The pull-in abilities of different parameters are evaluated through the simulation in this section. Table 4-6 shows the parameter sets of interests, the natural frequency range from 15 Hz to 50 Hz with a step of 5 Hz, and the damping ratio range from 0.707 to 5.6 with a step of 0.707.

Table 4-6: Parameter Sets for Pull-in Ability Assessment of Directly PLL Method

Parameters	Natural frequency	Damping Ratio
1	$\omega_n = 15$ Hz	$\xi = 0.707$
2	$\omega_n = 30$ Hz	$\xi = 0.707$
3	$\omega_n = 50$ Hz	$\xi = 0.707$

4	$\omega_n = 50$ Hz	$\xi = 2.121$
5	$\omega_n = 50$ Hz	$\xi = 5.656$

The pull-in process of different initial frequency errors using a 30 Hz natural frequency and 0.707 damping ratio are shown in Figure 4.15, the initial frequency errors are 20 Hz, 40 Hz, and 60 Hz, respectively.

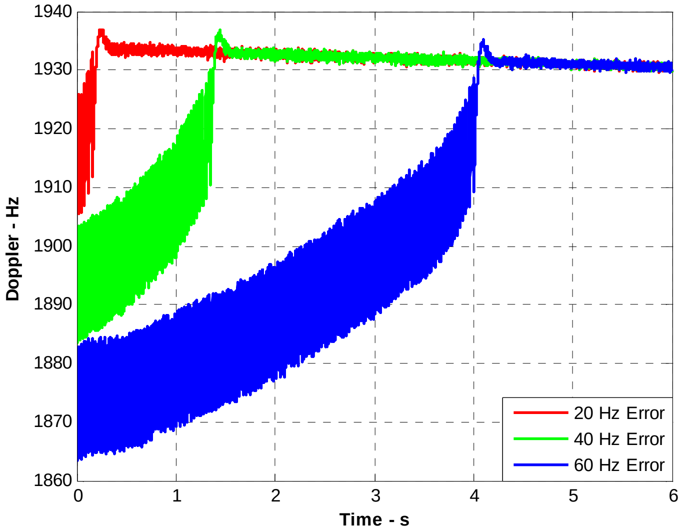

Figure 4.15: Pull-in Processes of Different Initial Errors for the First Parameter Set

The pull-in processes of different initial frequency errors are shown in this figure. For a 20 Hz initial frequency error, the pull-in time is less than 0.5 s, however, for a 60 Hz initial error, the pull-in time is around 4 s. It should be noted that the frequency error larger than 60 Hz cannot be pulled-in in this case. Figure 4.16 shows the pull-in ability of the 50 Hz natural frequency and 0.707 damping ratio.

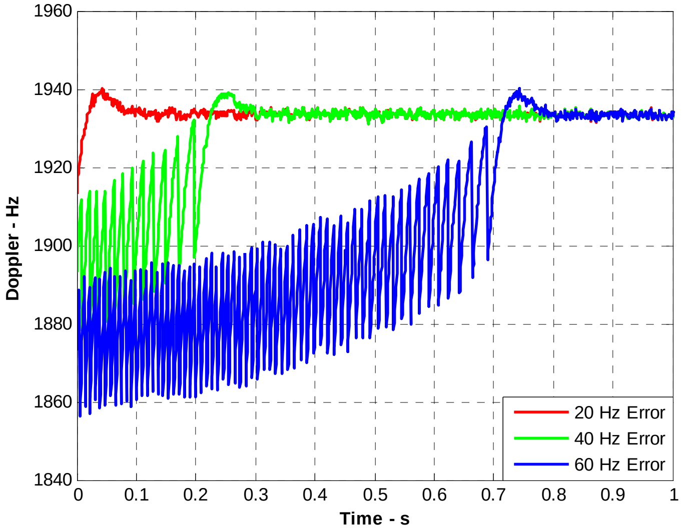

Figure 4.16: Pull-in Processes of Different Initial Errors for the Third Parameter Set

Similarly, both smaller initial frequency errors and larger natural frequency can reduce the pull-in time, these results agree with the analog results shown in Best (2004). The pull-in time for 60 Hz initial frequency is reduced from 4 s to 0.7 s compared to the 30 Hz natural frequency case. The pull-in ability is also improved since the natural frequency is increased. The maximum pull-in frequency error is 80 Hz in this case. These results show an improved performance by increasing the natural frequency of loop filter. In case 3, 4, and 5, the damping ratio is increased while holding the natural frequency constant. Figure 4.17 shows the performance of a natural frequency of 50 Hz and a damping ratio of 2.1.

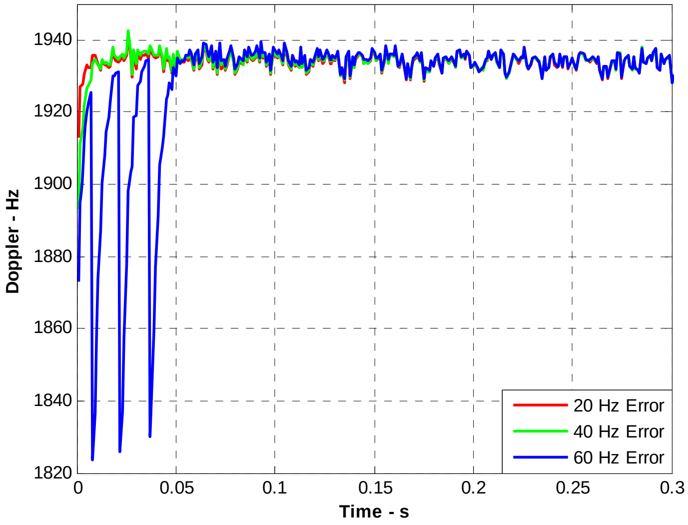

Figure 4.17: Pull-in Processes of Different Initial Errors for the Forth Parameter Set

As expected, larger damping ratio can further reduce the pull-in time of a PLL. Also, the pull-in ability is improved since a 100 Hz initial frequency error can be easily pull-in by this parameter set. This figure also suggests that for a 60 Hz initial frequency error, the PLL can be used directly to track the frequency and phase, since the pull-in time for 60 Hz frequency error is reduced to 50 ms. However, for the 200 Hz initial frequency error, which is the largest frequency uncertainty assumed in Chapter 2, it is very hard to be pulled-in by directly PLL method even larger parameter values are applied. To this end, for the directly PLL case, only the initial frequency error smaller than 100 Hz is considered.

It is noted that the one-step piece-wise logic used in section 4.3 is not a good choice for directly piece-wise PLL method as shown in Figure 4.18, a slow pull-in process is clearly shown in this figure after the piece-wise period. This is due to the large frequency noise during the piece-wise period and the initial frequency error is still large for the standard parameters. This means that standard PLL needs a long time to pull-in the frequency error.

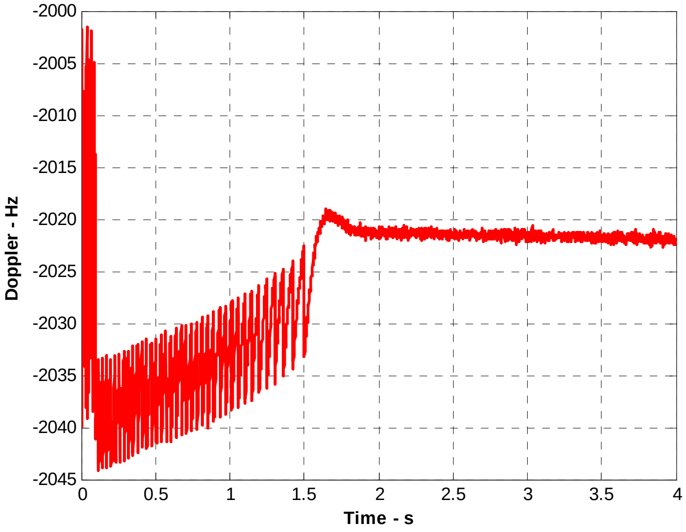

Figure 4.18: Directly Piece-Wise PLL Performance with an Initial Frequency Error of 100 Hz for One-Step Logic

To this end, a two-step piece-wise PLL method is employed in the directly piece-wise PLL architecture, as shown in Table 4-7. The same procedure is applied to obtain the proper tracking loop parameters as shown in the piece-wise FLL section.

Table 4-7 Logic for Piece-Wise PLL Directly

	Natural Frequency	Damping Ratio	Piece-Wise Epochs
First step	50 Hz	5.6	50 ms
Second step	30 Hz	2.1	20 ms

Figure 4.19 and Figure 4.20 show the performance of two-step piece-wise control method.

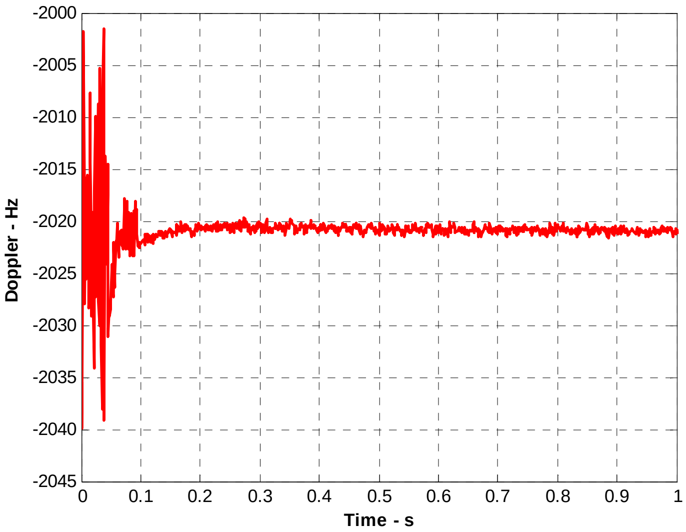

Figure 4.19: Frequency Transition Process of Directly Piece-Wise PLL Method with an Initial Frequency Error of 100 Hz for Two-Step Logic

At the first step, large natural frequency and damping ratio are used, as shown in Figure 4.19; from this, a 100 Hz initial frequency error can be easily pull in by this parameter set. The second step is used to reduce the remaining frequency error after the first step. After this, the standard parameters are used for the carrier phase tracking. Figure 4.20 shows the carrier phase transition process.

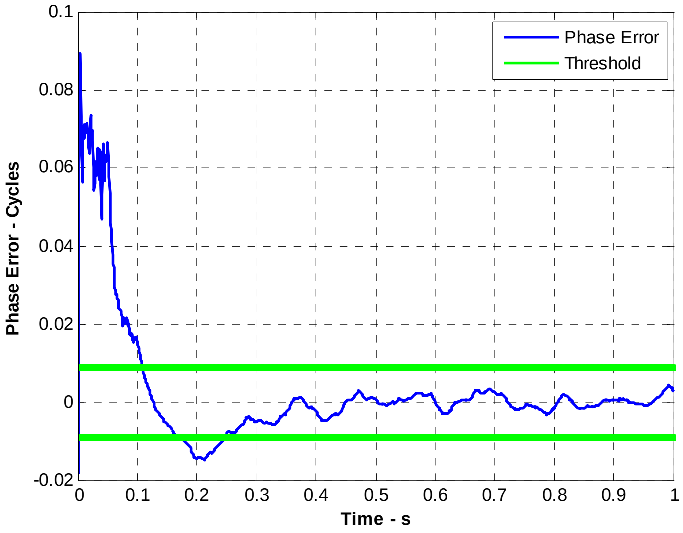

Figure 4.20: Phase Error Transition Process of Directly Piece-Wise PLL Performance with an Initial Frequency Error of 100 Hz

It is shown that the carrier phase transition process for two-step piece-wise PLL method is 0.25 s. However, compared to the piece-wise FLL followed by the piece-wise PLL scheme, they have almost the same transition times.

The results shown in this section suggest that for smaller initial frequency errors, a PLL can be used directly to track the frequency and carrier phase (after reaching steady-state, both frequency and carrier phase are locked). However, for larger initial frequency errors, using a directly PLL method is not preferred since it will take a long time to converge. Furthermore, a PLL may diverge due to the pull-in ability constraint. To this end, the piece-wise FLL followed by the piece-wise PLL scheme is recommended in this work.

4.5 Conclusion

Piece-wise approaches are proposed in this chapter, these include a piece-wise FLL followed by a piece-wise PLL method, and a direct piece-wise PLL method. The performance of each approach was assessed using data collected on a vehicle under mild to moderate operational conditions. For the piece-wise method, the transition time was shown to be reduced by a factor of approximately three for the frequency pull-in period and by a factor of about four for phase pull-in period. Finally, piece-wise FLL followed by piece-wise PLL scheme is recommended to reduce the reacquisition time during the carrier phase reacquisition process.

CHAPTER FIVE: PHASE PREDICTION METHOD

This chapter looks at the performance of a phase prediction method proposed in this work. The motivation of the phase prediction method comes from the standard phase tracking loop, which says the carrier phase is essentially the integration of carrier Doppler. However, the Doppler for a satellite can be estimated by projecting the computed receiver velocity onto the satellite line of sight, and this, in turn, can be integrated to predict carrier phase measurements. In so doing, if continuous velocity estimates are available with acceptable accuracy, effectively carrier phase measurements can be predicted by integrating the Doppler computed from vector-based navigation filter, and thus reduce the carrier phase reacquisition process. Details will be provided in the following sections.

5.1 Vector-Based Architecture Introduction

Before the phase prediction introduction, the detailed Kalman-based tracking loop structure used in the GSNRx™ software receiver is explained, including the dynamic model, measurement model, process noise, and observation noise. Figure (2.13) shows the structure of the vector-based receiver used in GSNRx™ (Petovello et al 2006). A cascaded approach is employed in the vector-based architecture, meaning each channel employs a local loop to track the carrier phase (but not frequency). Two different types of Kalman filter are employed in this architecture, namely, local Kalman filter and navigation filter.

Local Kalman filter is used to track the carrier phase. To this end, frequency error and phase error are estimated during the tracking process. The navigation filter is used to close the tracking loop, the position error, velocity error, and clock errors are estimated in the navigation filter (Petovello et al 2008, Bevly et al 2008). In this way, the navigation solution is used to drive the code and frequency NCO in the receiver. Each of the two Kalman filters will be discussed in the thesis. The Kalman filter generally consists of two models, namely, the dynamic model and measurement model, more details are available in Brown (1998), Zarchan (2004), Gelb (1974).

5.1.1 Local Kalman Filter

Dynamic model

In the Kalman filter based PLL, traditional discriminators and loop filters in the PLL are replaced by a Kalman filter (Petovello et al 2006, Psiaki et al 2007). Three-state Kalman-based tracking loop is already shown in Appendix B, where the states included the code phase error, the carrier frequency error, and carrier acceleration error. The equivalence between standard PLL and Kalman filter is shown there. However, the combined DLL and PLL approach is employed in the software receiver (Petovello et al 2006), where a five-state Kalman filter is used to track the errors in the predicted signals. The states to be estimated in the Kalman-based tracking loop are the amplitude of signal, the code phase error, the carrier phase error, the frequency error and the carrier acceleration error, which is given by

$$x = \begin{bmatrix} A & \delta\tau & \delta\varphi & \delta f & \delta a \end{bmatrix}^T \tag{5.1}$$

where A : Signal amplitude

$\delta\tau$: Code phase error in chips

$\delta\varphi$: Carrier phase error in radians

δf : Carrier frequency error in rad/s

δa : Carrier acceleration error in rad/s^2

Kalman filter state model is given by (Petovello et al 2006)

$$\begin{bmatrix} \dot{A} \\ \delta\dot{\tau} \\ \delta\dot{\varphi} \\ \delta\dot{f} \\ \delta\dot{a} \end{bmatrix} = \begin{bmatrix} 0 & 0 & 0 & 0 & 0 \\ 0 & 0 & 0 & \beta & 0 \\ 0 & 0 & 0 & 1 & 0 \\ 0 & 0 & 0 & 0 & 1 \\ 0 & 0 & 0 & 0 & 0 \end{bmatrix} \cdot \begin{bmatrix} A \\ \delta\tau \\ \delta\varphi \\ \delta f \\ \delta a \end{bmatrix} + \begin{bmatrix} 1 & 0 & 0 & 0 & 0 \\ 0 & 1 & \beta\cdot 2\pi f & 0 & 0 \\ 0 & 0 & 2\pi f & 0 & 0 \\ 0 & 0 & 0 & 2\pi f & 0 \\ 0 & 0 & 0 & 0 & 2\pi/\lambda \end{bmatrix} \cdot \begin{bmatrix} \omega_A \\ \omega_{\delta\tau} \\ \omega_b \\ \omega_d \\ \omega_a \end{bmatrix} \tag{5.2}$$

where β : Converts from units of radians to chips

ω_A : Driving noise of the amplitude

$\omega_{\delta\tau}$: Driving noise of code phase error

ω_b : Driving noise of clock bias

ω_d : Driving noise of clock drift

ω_a : Driving noise to account for line-of-sight acceleration

The main tuning parameter taken into consideration in this work is the spectral density of the line of sight acceleration driving noise ω_a, which is related to the receiver dynamics, and in turn, decides the natural frequency for the Kalman filter, which is shown in the Appendix C.

Measurement model

Before discussing the measurement model in detail, first consider the form of the correlator outputs. The in-phase (I) and quadra-phase (Q) correlator outputs can be written as (Petovello and Lachapelle 2006)

$$I = A \cdot N \cdot R\left(\delta\tau - \Delta\right) \cdot \frac{\sin\left(\pi \cdot \delta f \cdot T_c\right)}{\pi \cdot \delta f \cdot T_c} \cdot \cos\left(\delta\overline{\varphi}\right) \tag{5.3}$$

and

$$Q = A \cdot N \cdot R\left(\delta\tau - \Delta\right) \cdot \frac{\sin\left(\pi \cdot \delta f \cdot T_c\right)}{\pi \cdot \delta f \cdot T_c} \cdot \sin\left(\delta\overline{\varphi}\right) \tag{5.4}$$

where N : Number of samples in the correlator

R : Auto-correlation function

Δ : Correlators offset (e.g., for the early or late correlators), ± 0.5 chips in this case

T_c : Integration time

$\delta\overline{\varphi}$: Average local phase error during the integration interval

The average phase error is given by (Petovello et al 2006)

$$\delta\overline{\varphi} = \delta\varphi_0 + \delta f_0 \cdot \frac{T_c}{2} + \delta a_0 \cdot \frac{T_c^{\,2}}{6} \tag{5.5}$$

where $\delta\varphi_0$: Phase error at the start epoch of the integration interval

δf_0 : Frequency error at the start epoch of the integration interval

δa_0 : Carrier acceleration error at the start epoch of the integration interval

The measurements come from the correlators outputs available from each channel. Since the code error is estimated in the Kalman filter, the correlator outputs from early, prompt, and late replica codes are also included in the observations. The observation vector z is then given by

$$z = \begin{bmatrix} I_E & Q_E & I_P & Q_P & I_L & Q_L \end{bmatrix}^T \tag{5.6}$$

where E, P, and L indicate the correlators output at early, prompt, and late replica codes, respectively. The design matrix can be obtained by expanding the observation equation in a Taylor series as given by

$$\begin{aligned} H_i &= \frac{\partial z_i}{\partial x} \\ &= \begin{bmatrix} \frac{\partial z_i}{\partial A} & \frac{\partial z_i}{\partial \delta\tau} & \frac{\partial z_i}{\partial \delta\varphi} & \frac{\partial z_i}{\partial \delta f} & \frac{\partial z_i}{\partial \delta a} \end{bmatrix} \end{aligned} \tag{5.7}$$

Measurement variance is given by (Van Dierendonck 1995)

$$\sigma^2 = \sigma_I^2 = \sigma_Q^2 = \frac{1}{2 \cdot 10^{0.1 \cdot C/N_0} \cdot T_c} \tag{5.8}$$

where C/N_0 : Signal to noise ratio

For 50 dB/Hz C/N$_0$ and 1 ms integration time, the observation noise is $\sigma^2 = 0.005$. Notice that the observations for the different replica codes are correlated with each other, this returns the observation noise matrix (Salem 2010)

$$R = \sigma^2 \begin{bmatrix} 1 & 0 & 0.5 & 0 & 0 & 0 \\ 0 & 1 & 0 & 0.5 & 0 & 0 \\ 0.5 & 0 & 1 & 0 & 0.5 & 0 \\ 0 & 0.5 & 0 & 1 & 0 & 0.5 \\ 0 & 0 & 0.5 & 0 & 1 & 0 \\ 0 & 0 & 0 & 0.5 & 0 & 1 \end{bmatrix} \tag{5.9}$$

Equation (5.8) also suggests that longer integration time will improve the tracking performance.

5.1.2 Navigation Filter

Dynamic model

Navigation filter is used to close the tracking loop in the vector-based architecture, and is assumed to have the following system model (Petovello et al 2006)

$$\begin{bmatrix} \dot{p} \\ \dot{v} \\ \dot{b} \\ \dot{d} \end{bmatrix} = \begin{bmatrix} 0_{3\times3} & I_{3\times3} & 0_{3\times1} & 0_{3\times1} \\ 0_{3\times3} & 0_{3\times3} & 0_{3\times1} & 0_{3\times1} \\ 0_{1\times3} & 0_{1\times3} & 0_{1\times1} & I_{1\times1} \\ 0_{1\times3} & 0_{1\times3} & 0_{1\times1} & 0_{1\times1} \end{bmatrix} \cdot \begin{bmatrix} p \\ v \\ b \\ d \end{bmatrix} + \begin{bmatrix} 0_{3\times3} & 0_{3\times1} & 0_{3\times1} \\ I_{3\times3} & 0_{3\times1} & 0_{3\times1} \\ 0_{1\times1} & I_{1\times1} & 0_{1\times1} \\ 0_{1\times1} & 0_{1\times1} & I_{1\times1} \end{bmatrix} \cdot \begin{bmatrix} (\omega_v)_{3\times1} \\ (\omega_b)_{1\times1} \\ (\omega_d)_{1\times1} \end{bmatrix} \tag{5.10}$$

where subscripts indicate the dimension of the quantity

p : Vehicle position vector

v : Vehicle velocity vector

b, d : Clock bias and drift, respectively

I, 0 : Identity matrix and zero matrix, respectively

ω_v : Velocity uncertainty

ω_b : Clock bias uncertainty

ω_d : Clock drift uncertainty

This model assumes the velocity is a random walk process, however, higher order models may be selected for other applications.

Measurement model

The pseudorange and Doppler errors are used as the measurements in the navigation filter. The pseudorange is given by

$$\rho_i = \left\| p_i - p \right\| + c \cdot b \tag{5.11}$$

where p_i : Satellite position vector

c : Speed of light

The Doppler is given by

$$f_i = \frac{(v_i - v)(p_i - p)}{\lambda \left\| p_i - p \right\|} + c \cdot d \tag{5.12}$$

where v_i : Satellite velocity

λ : Signal wavelength in meters

Equation (5.12) is also used to generate local carrier replica frequency to control the NCO. The same as the local Kalman filter case, the design matrix can be obtained by expanding the observation Equations (5.11) and (5.12) in a Taylor series as given by

$$H_{2i-1} = \frac{\partial z_i}{\partial p}, H_{2i} = \frac{\partial z_i}{\partial v} \tag{5.13}$$

where i from 1 to m (the LOS satellites number).

5.2 Phase Tracking

As mentioned in Chapter 2, carrier phase is essentially the integration of Doppler in the phase tracking loop. However, in the vector-based tracking loop, the NCO is controlled by the navigation filter. In so doing, the carrier phase is the integration of predicted Doppler plus phase corrections from the local Kalman filter. One can therefore write

$$\varphi_{k+1} = \varphi_k + \int_{t_k}^{t_{k+1}} f dt + \Delta\varphi \tag{5.14}$$

where φ_{k+1}, φ_k : Carrier phase at the $k+1$ and k epoch, respectively

f : Carrier Doppler from the navigation filter

$\Delta\varphi$: Predicted phase error from the local Kalman filter

Figure 5.1 shows an example for the predicted phase error during 3 seconds interval under the open-sky scenario. Generally, $\Delta\varphi$ indicates the phase error induced by the imperfect velocity estimation from the navigation filter, the signal noise, and multipath error, which is estimated by the local Kalman filter and should be corrected at every epoch, otherwise the phase error will accumulate with time.

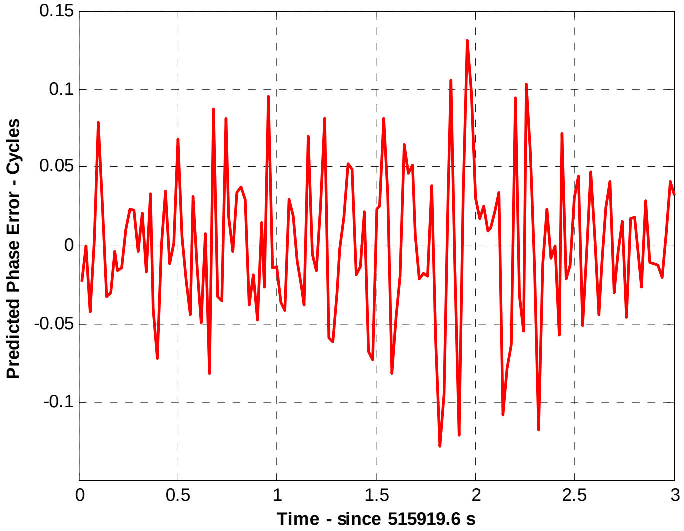

Figure 5.1: Predicted Phase Error during 3 Seconds Open-Sky Period

5.3 Phase Prediction Method

Given the above, a phase prediction architecture is proposed in this work to predict carrier phase during periods of loss of lock. Obviously, the tracking loop cannot provide continuous carrier phase measurements during loss of signal lock periods. However, in the vector-based architecture, if continuous velocity estimates are available with acceptable accuracy, carrier phase measurements can effectively be predicted by integrating the Doppler computed from vector-based navigation filter. This is given mathematically by

$$\varphi_{k+1} = \varphi_k + \int_{t_k}^{t_{k+1}} f dt \tag{5.15}$$

Notice that here the predicted phase error from the Kalman filter is not available compared to Equation (5.14) since the signal is not being tracked, which means that the phase error will accumulate with time during phase prediction process. The idea is to start the phase prediction a few epochs before the loss of phase lock epoch, and terminate when the signal is reacquired. Practically, this can be implemented as shown in Figure 5.2, for example.

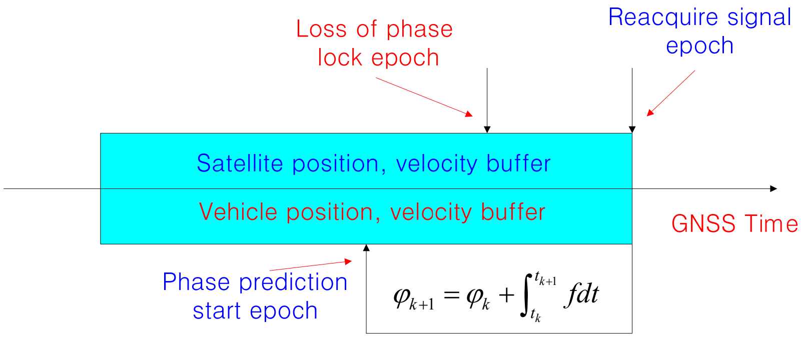

Figure 5.2: Phase Prediction Schedule for the Loss of Phase Lock Case

Position and velocity buffers are used to predict the Doppler during the phase prediction process, since the phase error at the loss of phase lock epoch is larger than the predefined threshold, as such, the phase prediction process is started when the phase error is small (check the PLI). The potential benefits of this approach include the continuous carrier phase observations are effectively provided during loss of the lock period, and cycle slips are automatically compensated if the phase error (over the loss of lock period) is smaller than a quarter-cycle. Another advantage is that the reacquisition process can be started with small phase and frequency error thus allowing a PLL to be used directly. By extension, the benefit of a small initial phase error is shown in the Chapter 4.

Equation (5.15) also suggests that the carrier phase prediction strategy can be used in any architecture where the predicted Doppler is available, not only in the vector-based receiver. Figure 5.3 shows the general phase prediction strategy, which can be used in the standard receiver.

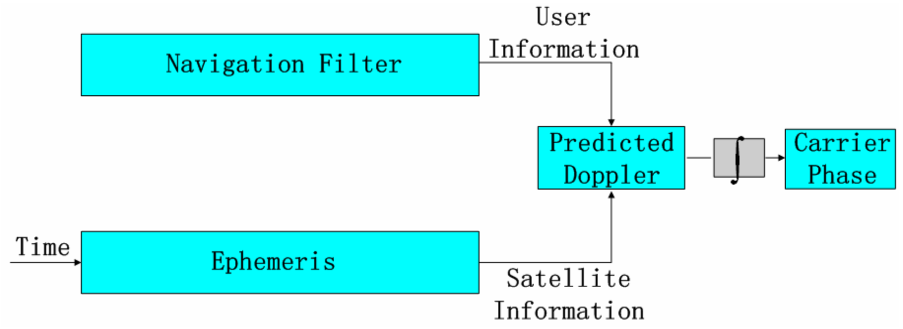

Figure 5.3: General Phase Prediction Strategy

In so doing, when the satellite signal becomes available again or at least strong enough to acquire, the phase of the signal is already predicted. However, the question arises as to the quality of predicted carrier phase.

To get an idea of the expected performance of the proposed approach, it is assumed that the velocity error is white noise. This is reasonable in most cases since the velocity is computed from the Doppler measurements and the systematic error *rates* due to the satellite errors and atmospheric effects are much lower than the Doppler measurement noise. Recall that the equation for the predicted Doppler was shown in (5.12). Assuming the east-north-up vehicle velocity uncertainties respectively denoted as σ_{v_E}, σ_{v_N}, and σ_{v_U}, are independent of each other, using variance propagation (Gao 2008), the Doppler accuracy is given by (oscillator error is not considered here, although it is assumed the change in clock drift will be minimal over short data outage durations):

$$\sigma_{f_i}^2 = \frac{1}{\lambda^2}\begin{bmatrix}\cos\alpha_i \sin\psi_i & \cos\alpha_i \cos\psi_i & \sin\alpha_i\end{bmatrix}\begin{bmatrix}\sigma_{v_E}^2 & 0 & 0 \\ 0 & \sigma_{v_N}^2 & 0 \\ 0 & 0 & \sigma_{v_U}^2\end{bmatrix}\begin{bmatrix}\cos\alpha_i \sin\psi_i \\ \cos\alpha_i \cos\psi_i \\ \sin\alpha_i\end{bmatrix} \tag{5.16}$$

where α, ψ : Satellite elevation and azimuth respectively

Further assuming the velocity standard deviations in the north and east directions are the same, and denoting them as σ_H, then

$$\sigma_{f_i}^2 = \frac{1}{\lambda^2}\left(\sigma_H^2 \cos^2\alpha_i + \sigma_U^2 \sin^2\alpha_i\right) \tag{5.17}$$

where σ_H^2 : Vehicle horizontal velocity variance

σ_U^2 : Vehicle vertical velocity variance

Generally, $\sigma_U^2 > \sigma_H^2$ due to satellite geometry. This is written as $\sigma_U^2 = \sigma_H^2 + \Delta\sigma^2$ where $\Delta\sigma^2$ represents an increase in the vertical variance relative to the horizontal variance. Substituting this into equation (5.17) gives

$$\sigma_{f_i}^2 = \frac{1}{\lambda^2}\left(\sigma_H^2 \cos^2\alpha_i + \left(\sigma_H^2 + \Delta\sigma^2\right)\sin^2\alpha_i\right) = \frac{1}{\lambda^2}\left(\sigma_H^2 + \Delta\sigma^2 \sin^2\alpha_i\right) \tag{5.18}$$

This equation shows that higher elevation satellites will have larger predicted Doppler error. This makes sense because the largest velocity uncertainty is in the vertical direction.

Returning again to the assumption of white velocity errors, the variance of the predicted carrier phase, in units of cycles squared, is given by

$$\begin{aligned}\mathrm{var}_{\varphi}(t,\tau) &= E\left[\varphi(t)\varphi(\tau)\right] \\ &= E\left[\int_0^t f(\lambda)\,d\lambda \int_0^\tau f(\zeta)\,d\zeta\right] \\ &= \int_0^t\int_0^\tau E\left[f(\lambda)f(\zeta)\right]d\lambda d\zeta \\ &= \int_0^t\int_0^\tau \Theta_f^2\,\delta(\lambda-\zeta)\,d\lambda d\zeta \\ &= \Theta_f^2 \min(t,\tau)\end{aligned} \tag{5.19}$$

where $\delta(\lambda-\zeta)$: Dirac delta function

$E[\;]$: Expectation function

Θ_f : Spectrum density of a white rate noise process

which yields

$$\mathrm{var}_{\varphi}(t,t) = \Theta_f^2 t \tag{5.20}$$

Notice that the unit of Θ_f is $cycle/s/\sqrt{Hz}$, which is given by

$$\Theta_f = \sigma_f / \sqrt{1/T_c} \tag{5.21}$$

From Equation (5.20), the predicted carrier phase is a random walk process with an accuracy given as a function of loss of lock duration time t and predicted Doppler accuracy Θ_f.

To confirm the above, the phase prediction performances under different velocity accuracy scenarios and different receiver architectures are assessed below. Section 5.4 shows the performance for vector-based architecture in the open-sky scenario, partially dense-foliage scenario, and dense-foliage scenario. Section 5.5 shows the performance for ultra-tight receiver in the dense-foliage scenario and simulated passing under bridge scenario.

5.4 Predicted Phase Accuracy Assessment for Vector-Based Architecture

5.4.1 Open-Sky Scenario

The open-sky static test data was first used to obtain a baseline performance for phase prediction under ideal operating conditions. Specifically, loss of signal lock was manually induced on a single satellite every three seconds for a duration of two seconds. A total of 150 losses of lock were simulated. The velocity error for the first 200 seconds in this benign scenario is shown in Figure 5.4:

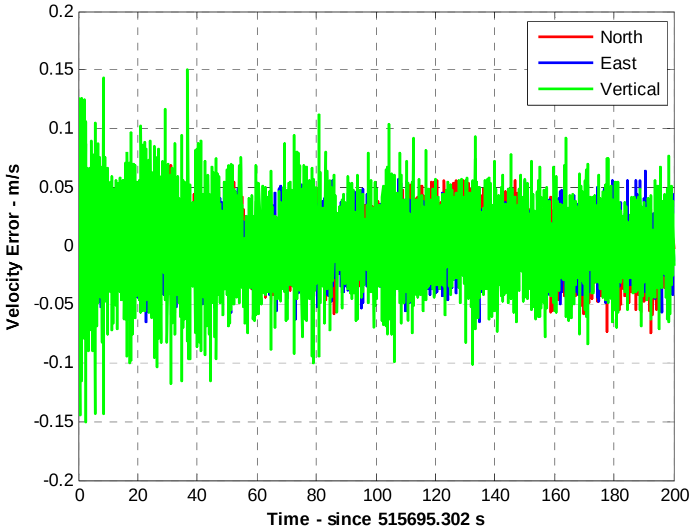

Figure 5.4: Static Open-Sky Scenario Velocity Error

The standard deviation of north, east and vertical errors are 0.02 m/s, 0.02 m/s, and 0.03 m/s respectively, and the velocity update rate is 20 Hz. Using Equations (5.17) and (5.21), for PRN 22 (21 degrees elevation angle with a C/N$_0$ of 42 dB-Hz), this gives a predicted Doppler spectral density of $0.025\,cycle/s\big/\sqrt{Hz}$. Figure 5.5 shows the error of the predicted carrier phase during the 150 losses of lock simulated in the data set.

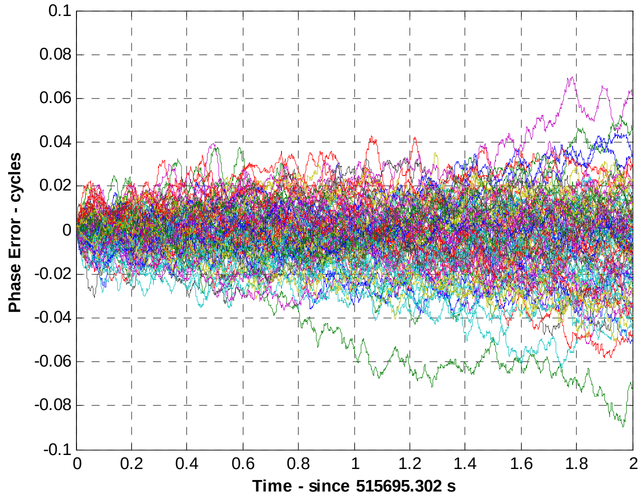

Figure 5.5: Error of Predicted Phase for PRN 22 under the Static Open-Sky Scenario over Two Seconds

Figure 5.6 shows the phase prediction standard deviation for PRN 22.

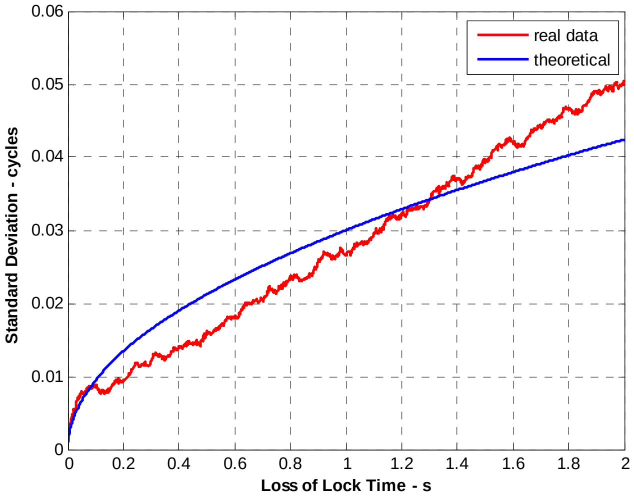

Figure 5.6: Phase Prediction Error Standard Deviation under Static Open-Sky Scenario for PRN 22

The predicted phase error is only 0.05 cycles after 2 seconds, which agrees well with the theoretical value computed using Equation (5.20). Given the strong performance of the proposed method in the static scenario, the open-sky portions of the test were used to assess the quality of predicted carrier phase in more realistic conditions. Figure 5.7 shows the open-sky test trajectory.

Figure 5.7: Open-Sky Test Scenario Trajectory (red line shows the trajectory, from Google$^{\text{TM}}$)

The horizontal velocity accuracy during this test was 0.07 m/s, and the vertical velocity accuracy was 0.12 m/s, where NovAtel's Inertial Explorer software was employed to obtain the velocity reference trajectory. The three dimension velocity accuracy for Inertial Explorer software is 0.03 m/s within 120 seconds (NovAtel 2010). For PRN 31 (65 degrees elevation angle with a C/N_0 of 49 dB/Hz), the predicted Doppler spectral density is $0.09\,cycle/s\Big/\sqrt{Hz}$ from Equation (5.17). Similar to the static data processing, loss of signal lock was artificially induced every five seconds for a duration of three seconds. Figure 5.8 shows the error of the predicted carrier phase during the 180 losses of lock simulated in the data set.

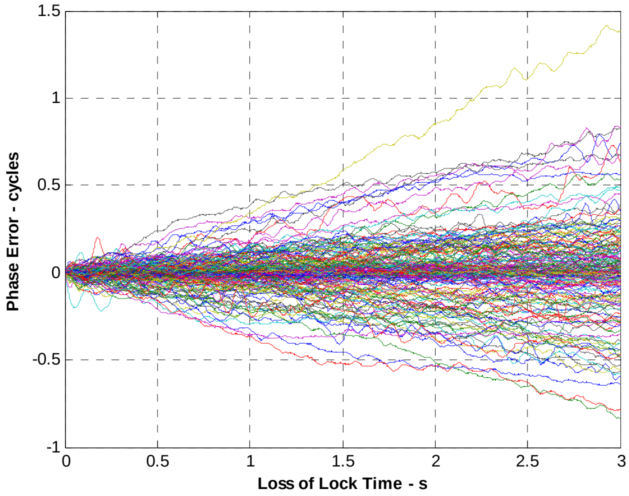

Figure 5.8: Error of Predicted Phase for PRN 31 under Open-Sky Scenario over Three Seconds

Figure 5.9 shows the standard deviation over three seconds.

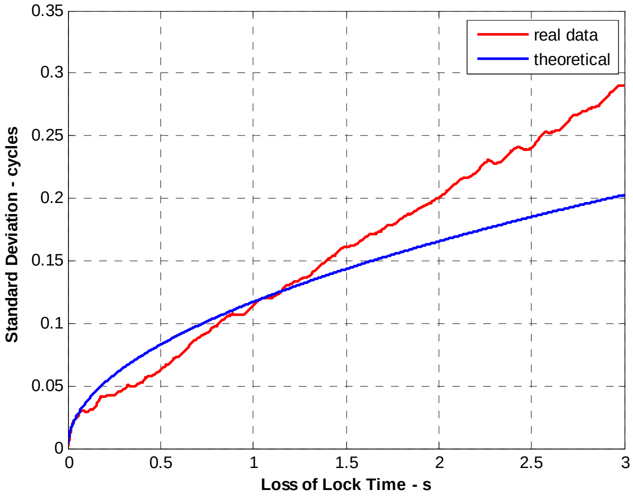

Figure 5.9: Phase Prediction Error Standard Deviation under Open-Sky Scenario for PRN 31

The theoretical predicted carrier phase accuracy is 0.13 cycles if loss of signal lock duration time is 1 second, and 0.25 cycles phase error after 3 seconds. Furthermore, for the time interval considered, the actual and theoretical errors are in close agreement, although the trend suggests this may not be the case for longer loss of lock times. Table 5-1 shows the phase prediction performance for five different satellites assuming loss of signal lock on only one satellite at a time.

Table 5-1: Summary of Predicted Carrier Phase Performance for Five Satellites under Open-Sky Scenario for Three Second Period

PRN	Elevation (degrees)	C/N_0 (dB/Hz)	Theoretical σ_φ (cycles)	Actual σ_φ (cycles)
16	33	44	0.16	0.42
20	62	49	0.22	0.18
23	47	49	0.20	0.31
31	65	50	0.22	0.29
32	52	50	0.21	0.22

Although the actual error standard deviations do not match the theoretical values exactly, the agreement suggests the theoretical value is generally a reasonable approximation over a period of a few seconds at least. That said, the disagreement is obviously larger for PRN 16. The most likely reason for this is the implicit assumption made when predicting carrier phase, namely, that the Doppler is constant value during each navigation solution update interval (50 ms in this case). However, this is not true in all cases, especially during dynamic periods. Furthermore, PRN 16 is the lowest elevation satellite in the table, and will thus be subject to the most signal dynamics since the vehicle is moving almost entirely in the horizontal plane.

5.4.2 Partially Dense-foliage Scenario

As an assessment of the algorithm in degraded signal scenarios, data from a short, partially dense-foliage section of the test was used to evaluate the carrier phase prediction performance in the low signal power scenarios. Figure 5.10 shows part of the test trajectory containing partially dense-foliage (red curve in the figure). The signal from PRN 22 was blocked by the trees to the south, as the elevation of this satellite was 21 degrees, and azimuth was 118 degrees. In this scenario, a 0.6 seconds loss of signal lock was experienced "naturally" (i.e., not manually induced). In the standard and vector-based receiver (without phase prediction), carrier phase measurements were not available during this loss of lock period.

Figure 5.10: Partially Dense-foliage Scenario (red line indicates the trajectory, from Google^{TM})

Figure 5.11 shows the front-view of partially dense-foliage scenario.

Figure 5.11: Partially Dense-foliage Scenario (Front View)

Figure 5.12 shows the velocity error of the vector-based receiver during the partially dense-foliage period, the navigation filter update interval is 50 ms for vector-based receiver.

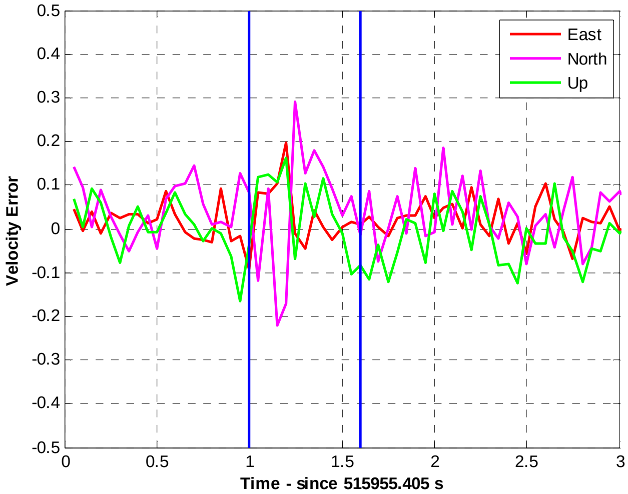

Figure 5.12: Velocity Performance during Partially Dense-foliage Scenario over Three Seconds (blue lines denote partially dense-foliage period)

It is observed that the velocity errors are increased during the partially dense-foliage period, as shown in the region within blue lines. This is due to the multipath and change of satellite geometry which increases the PDOP from 2.6 (8 satellites were used in the navigation filter) to 3.8 (5 satellites were used in the navigation filter). The region within the blue lines in Figure 5.13 shows the predicted Doppler performance in vector-based navigation filter during the partially dense-foliage scenario. Carrier Doppler and carrier phase outputs from ultra-tight receiver are considered as reference here. In the ultra-tight receiver, the signal for PRN 22 was tracked well since the aiding information from INS is available. As can be seen, the predicted Doppler error increased significantly during the loss of lock period.

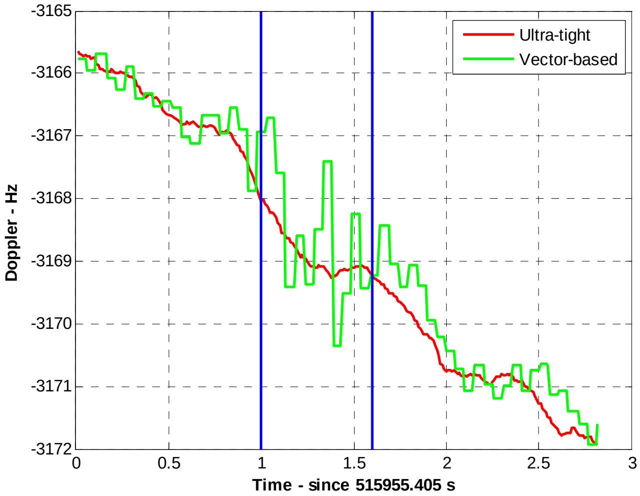

Figure 5.13: Doppler vs Time (blue lines denote loss of lock period)

Similarly, Figure 5.14 shows the error of the predicted carrier phase during this same period. Predicted carrier phase measurements were given by the proposed phase prediction method with acceptable error, namely less than 0.17 cycles during 0.6 s loss of lock period.

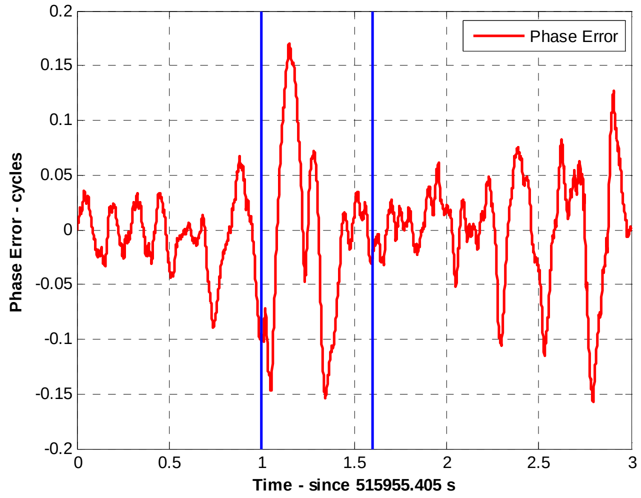

Figure 5.14: Performance of Predicted Phase during Partial Dense-foliage Period (indicated by blue lines)

It is noted, however, that the vector-based tracking is still initialized using scalar algorithms in the general vector-based architecture. Figure 5.15 shows the carrier phase transition process after reacquiring the signal, where a standard PLL is used.

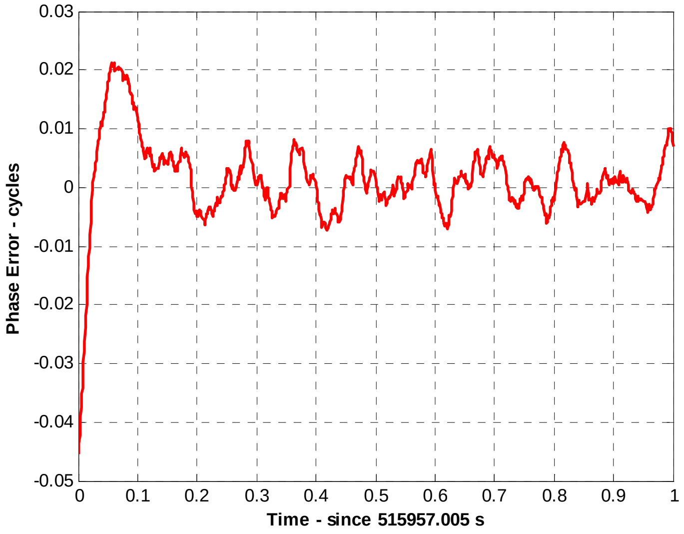

Figure 5.15: Phase Transition Process after Reacquiring the Signal Again

The transition time is less than 100 ms since the initial phase error is smaller than 0.05 cycles. This, in turn, demonstrates the benefit of the predicted carrier phase method. Specifically, the receiver can be started with small frequency error and small phase error. The following subsection analyzes the quality of predicted carrier phase in more stringent scenarios, namely, dense-foliage scenario. In so doing, a comparison is made for the phase prediction performance in the different velocity accuracy conditions. In the dense-foliage scenario, at least four satellites can be observed in the vector-based receiver, which is the case in the simulation shown later, otherwise the velocity cannot be obtained.

5.4.3 Dense-foliage Scenario

The phase prediction performance under dense-foliage scenario is assessed in this section. First of all, a simulated dense-foliage scenario is applied, where an outage on several satellites is simulated. This approach closely approximates a real dense-foliage scenario but provides the opportunity to generate a reference solution. In the second part, a real dense-foliage data is used to verify the simulation results.

A dense-foliage scenario is simulated first, the data was collected in an open-sky scenario as shown in Figure 5.16, however, an elevation constraint is applied in the receiver for 10 seconds. Specifically, during the simulated dense-foliage period, any satellite whose elevation angle was less than 40 degrees was (intentionally) not tracked by the receiver. In so doing, the GNSS constellation is similar to the dense-foliage scenario where there is still a view of the sky above 40 degrees.

Figure 5.16: Open-Sky Scenario (Front View)

Figure 5.17 shows the satellite constellation in the open-sky scenario, which provides very good GNSS satellite visibility. It is observed that 4 satellites whose elevations are greater than 40 degrees.

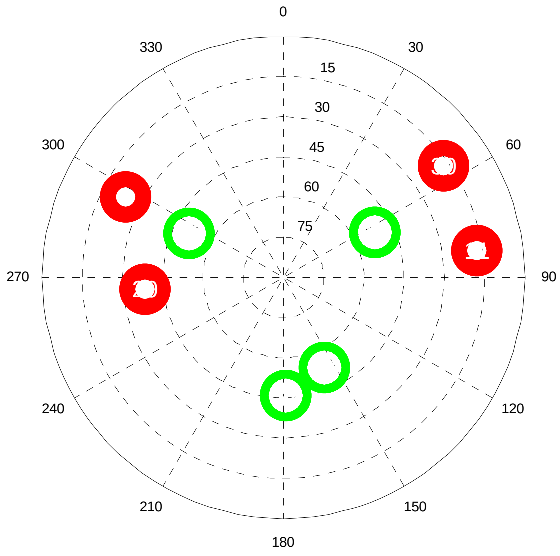

Figure 5.17: Sky-Plot of Open-Sky Scenario (satellites indicated in green/red are above/below 40 degrees elevation)

The benefit of this approach is that the carrier phase reference can be obtained in the open-sky condition. This is superior to the real dense-foliage scenario where it is very hard to obtain the phase reference for low elevation satellite. PRNs 14, 17, 31, and 32 are tracked by the receiver and thus used to update the navigation solution. Figure 5.18 shows the velocity performance for the vector-based architecture during the simulated dense-foliage period.

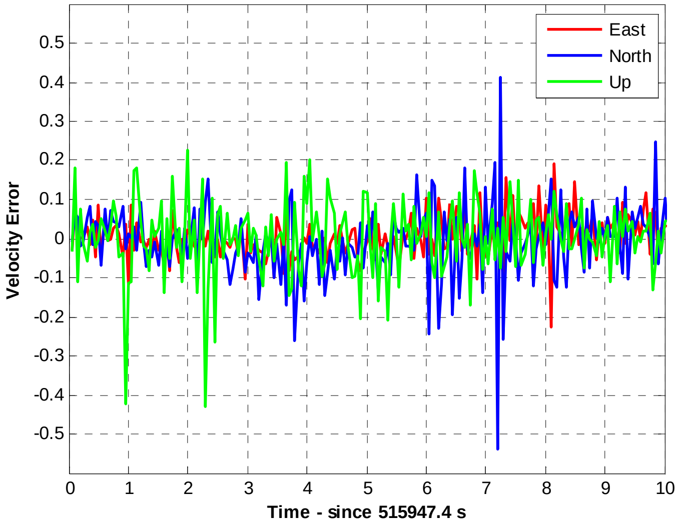

Figure 5.18: Velocity Performance of Vector-Based Receiver under Simulated Dense-Foliage Scenario

The standard deviation of north, east and vertical errors of the first 7 seconds are 0.05 m/s, 0.08 m/s, and 0.10 m/s respectively and the velocity update rate is 20 Hz. It is noted that the north velocity error increased substantially after 7 s. Figure 5.19 shows the error of the predicted carrier phase for the satellites whose elevations are smaller than 40 degrees. In this case, the truth trajectories are obtained by processing the data using all available satellites, since the PLLs work well for the satellites whose elevation angles were less than 40 degrees during this period.

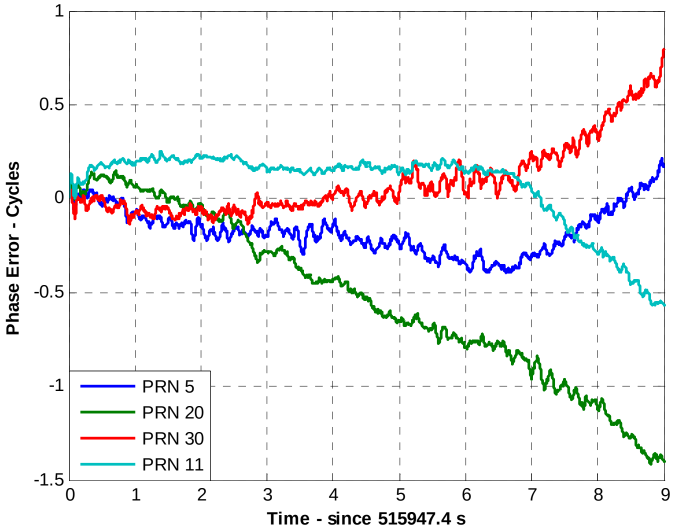

Figure 5.19: Phase Error for Vector-Based Receiver in the Simulated Dense-Foliage Scenario

It is observed that after 5 seconds, the phase error is smaller than half-cycle for PRNs 5, 11, and 30, however, the apparent increase starting at approximately 7 s is due to the north velocity error increase shown in Figure 5.18. Two other simulated dense-foliage scenarios are also simulated at different times for a duration of 10 seconds to show the vector-based receiver performance case. Figure 5.20 summaries the maximum phase errors within 5 seconds among these three scenarios.

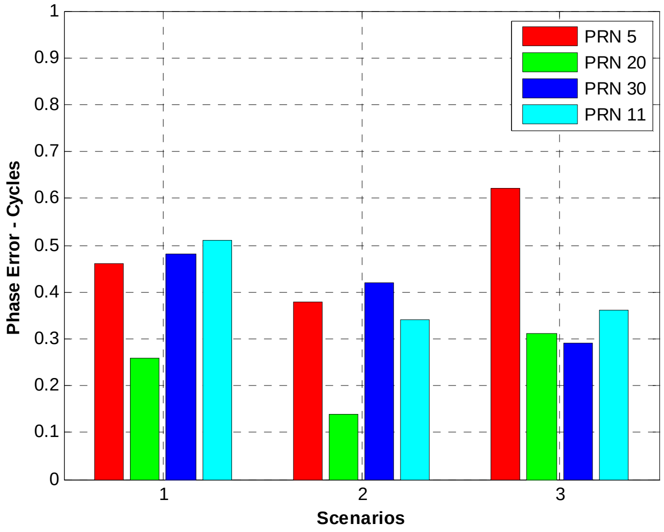

Figure 5.20: Maximum Phase Errors within 5 Seconds

for Vector-Based Receiver among 3 Simulated Dense-Foliage Scenarios

These results suggest that in the dense-foliage scenario, the higher elevation satellites can be used to generate receiver velocity, then predicted phase for low elevation satellites can be obtained with reasonable accuracy by integrating the predicted Doppler. However, in the scenario if the constellation is less than 4 satellites, phase prediction method cannot be applied.

However, the drawbacks of simulated dense-foliage are two-fold. First, in the real dense-foliage scenario, the high elevation satellite could also be affected by the surroundings, which is not the case in the simulated dense-foliage scenario. Second, the 40 degrees elevation threshold may be too optimistic in the simulated scenario. Therefore, following the simulated case, a real dense-foliage evaluation is conducted to verify the predicted phase performance. Figure 5.21 shows the dense-foliage test scenario, the red line indicates the vehicle trajectory for 20-second traverse.

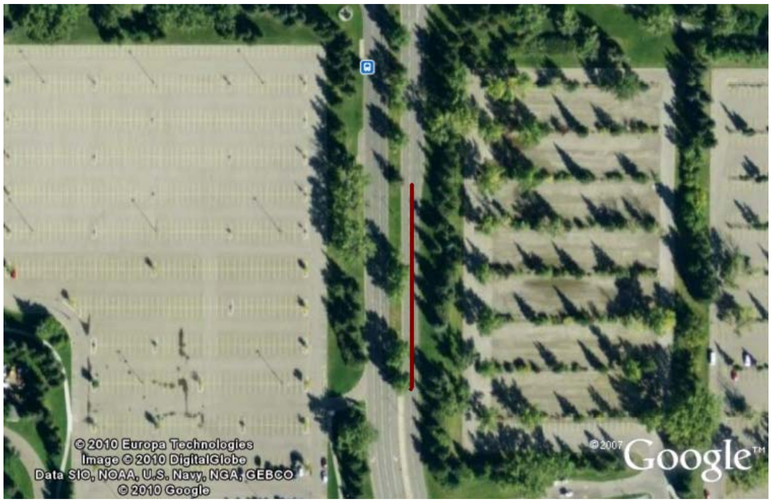

Figure 5.21: Real Dense-Foliage Scenario (red line indicates the trajectory, from Google^{TM})

Figure 5.22 shows the front view of the real dense-foliage scenario.

Figure 5.22: Dense-Foliage Scenario (Front View)

It is important to note that the 40 degrees elevation threshold is not satisfied in this case, fortunately, the signal for PRN 12 can be tracked since the azimuth is 179 degrees, then the full constellation for the GNSS-alone receiver includes PRNs 12, 14, 31, and 32. Since it is very hard to find a phase reference trajectory during the dense-foliage scenario for the low elevation satellites, the performance of predicted carrier phase is analyzed using PLI. Figure 5.23 shows the phase prediction performance for vector-based receiver, whereas the phase error is obtained by the Equation (4.2) shown in the Chapter 4.

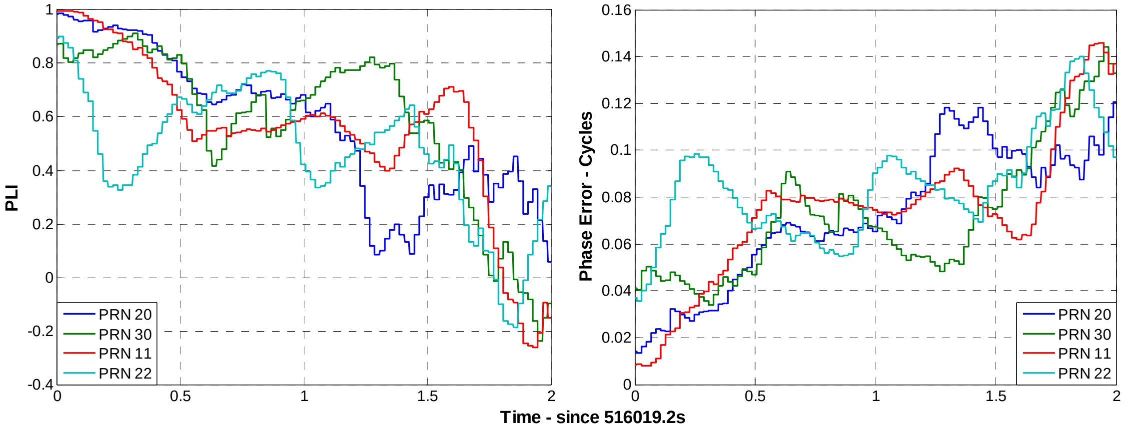

Figure 5.23: Phase Error for Vector-Based Architecture under Real Dense-Foliage Scenario over Two Seconds

Figure 5.23 only shows the first 2 seconds for the vector-based receiver, this is because the PLI is not a good metric when the phase error is larger than 45 degrees (PLI is 0 in this case). Compared to Figure 5.19, vector-based architecture has the same level of performance as the simulated dense-foliage, the phase error is smaller than 0.2 cycles after 2 seconds.

Section 5.4 assessed the performance of vector-based architecture in the open-sky scenario, partially dense-foliage scenario, and dense-foliage scenario. In the open-sky scenario, the predicted phase error is less than a quarter-cycle after two seconds. In the partially dense-foliage scenario, the carrier phase measurements are effectively provided during the 0.6 s loss of signal period, and the tracking loop can be started with small frequency error and small phase error after the signal is available again. In the dense-foliage scenario, the higher elevation satellites were used to generate receiver velocity, then obtain the predicted phase for low elevation satellites. The phase error was found to be smaller than half-cycle within 4 s.

5.5 Predicted Phase Accuracy Assessment for Ultra-Tight Receiver

The above analysis focused on the GNSS-only processing in a vector-based architecture and showed promising results. However, as noted in the Chapter 3, an ultra-tight receiver has better positioning performance than a GNSS-only receiver, and so it follows that the phase prediction concept can be applied to the ultra-tight receiver architectures with better performance. In the ultra-tight case, the receiver has the added benefit of using the inertial sensors to improve the navigation solution. In the context of this work, the improved navigation solution should yield better phase prediction accuracies than the GNSS-only case. Similar to the vector-based case, the simulated dense-foliage and real dense-foliage scenarios are also applied to the ultra-tight receiver. Moreover, a scenario where the receiver passes under a bridge is introduced assess the phase prediction performance under a more stringent signal scenario.

5.5.1 Dense-Foliage Scenario

This section is intended to show the improved performance of the phase prediction approach obtained with the aiding from INS under the dense-foliage scenario, where a high accuracy IMU (HG1700) is employed. Also, similar to the vector-based architecture, three simulated dense-foliage scenarios and a real dense-foliage scenario are applied. The data collected from the open-sky scenario as shown in section 5.4.3 is used to simulate the dense-foliage condition for 15 seconds. Figure 5.24 shows the improved velocity performance for the first simulated dense-foliage scenario. These results can be directly compared to the vector-based receiver results shown in Figure 5.18.

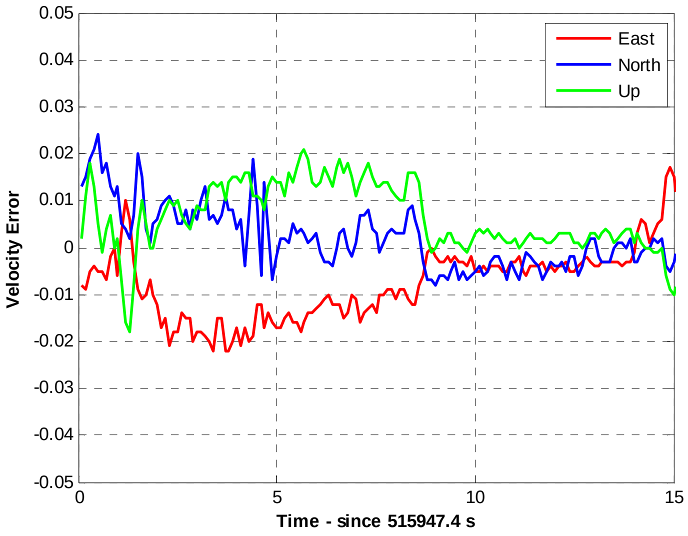

Figure 5.24: Ultra-Tight Receiver Velocity Performance under Simulated Dense-Foliage Scenario

It is noted that the velocity error is not white noise anymore, apparently a bias exists on the horizontal velocity. This is due to the uncompensated IMU errors in the navigation filter. Nevertheless, the overall errors are still smaller than in the vector-based case. Given their better velocity performance, better phase prediction can be obtained, this being the case as shown in Figure 5.25.

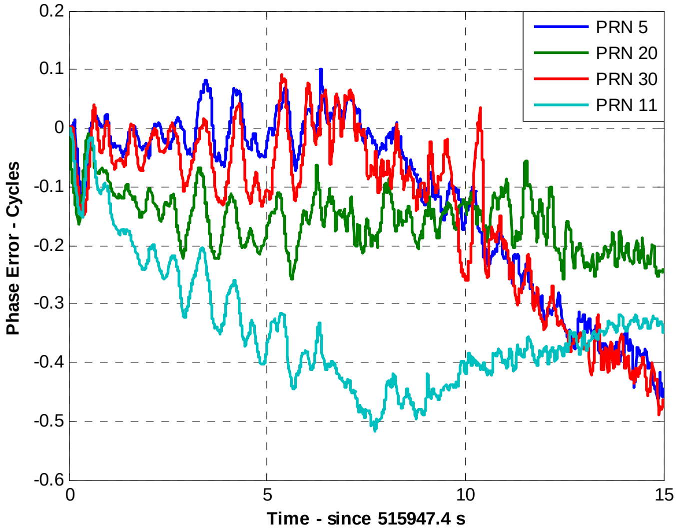

Figure 5.25: Predicted Phase Error for Ultra-Tight Receiver under the Simulated Dense-Foliage Scenario

As expected, the phase prediction performances for the ultra-tight receiver are better than the vector-based receiver. The error of the predicted phase is smaller than 0.5 cycles after 15 seconds as shown in Figure 5.25. More importantly, this is quite promising for carrier phase applications, since there are many scenarios where the receiver cannot track the signal very well. Such situations arise in dense-foliage and urban canyons, and in these situations the stand-alone GNSS receiver may not able to obtain the carrier phase measurements. Conversely, in the ultra-tight receiver, the continuous predicted phase is still available with reasonable accuracy. However, caution should be exercised when trying to incorporate such measurements in the navigation filter, since even a half cycle error can introduce relatively large position errors. Figure 5.26 summarizes the maximum phase errors for the three different dense-foliage scenarios over 5 seconds and 15 seconds.

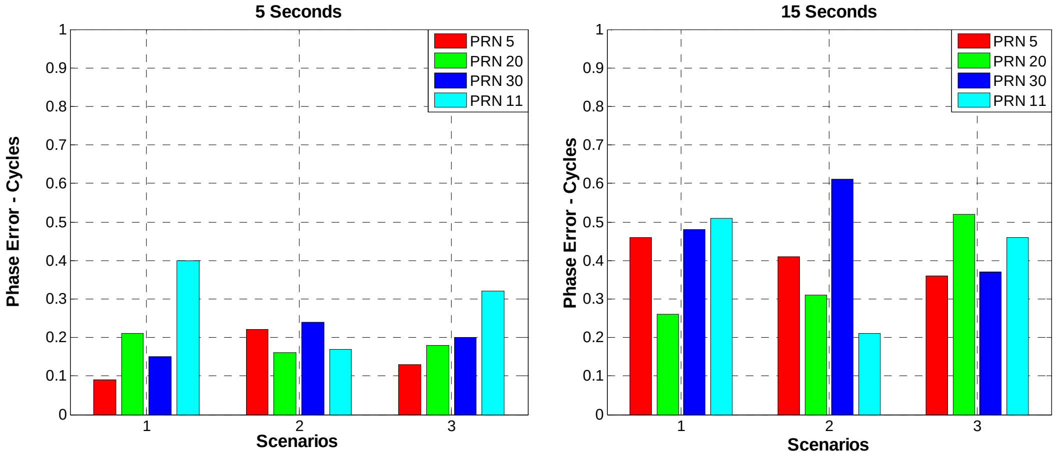

Figure 5.26: Phase Error Summary for Ultra-Tight Receiver under the Simulated Dense-Foliage Scenario over 5 s and 15 s

Compared to the vector-based receiver performance as shown in Figure 5.20, a better phase prediction performance is achieved by ultra-tight receiver. Figure 5.27 shows the ultra-tight performance in the real dense-foliage scenario, similar to the vector-based section, PLI is employed to obtain the phase errors.

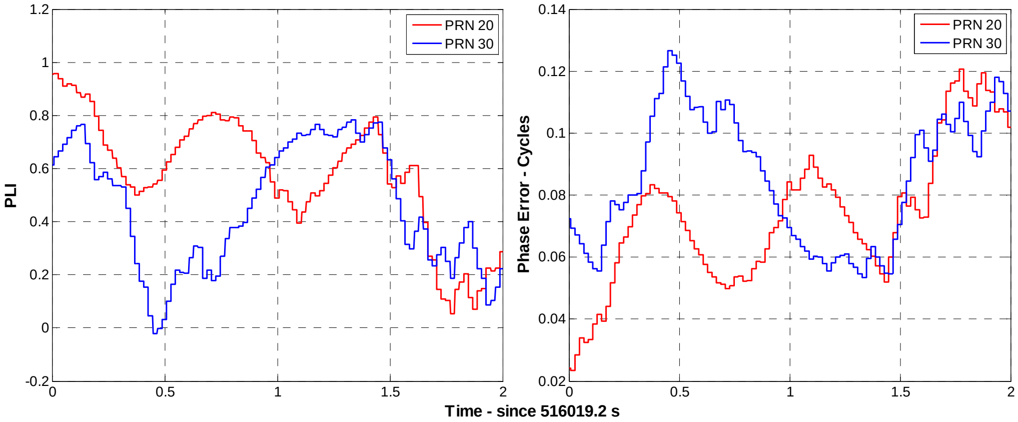

Figure 5.27: Phase Error for Ultra-Tight Receiver under Real Dense-Foliage Scenario over Two Seconds

Compared to Figure 5.26, ultra-tight architecture also has the same level of performance as the simulated dense-foliage.

5.5.2 Passing under the Bridge Scenario

The previous scenarios assumed the receiver performed in the degraded signal conditions, whereas some higher elevation satellites can be tracked. In this section, a more stringent scenario is assessed, namely, passing under the bridge scenario. In this case, the satellite signals are blocked by a simulated bridge, in so doing, the ultra-tight receiver relies solely on the INS, where no aiding information from GNSS is available, which means that the INS error will grow with time. For the GNSS-alone receiver, the carrier phase observations are not available when passing under the bridge since the receiver cannot track the signals. However, in the ultra-tight receiver, the velocity can be obtained by the INS, which in turn, can be used to predict the carrier phase. Herein, it is assumed that the length of a bridge is less than 100 metres, and the vehicle velocity is 20 m/s (72 km/h). In this case, a five-second period with no satellites is simulated.

Five bridge scenarios are simulated under open-sky conditions. Figure 5.28 shows the velocity performance of ultra-tight receiver during one of the scenarios, however, other scenarios have similar results except scenario 2, where the velocity error is slightly larger than the other four scenarios.

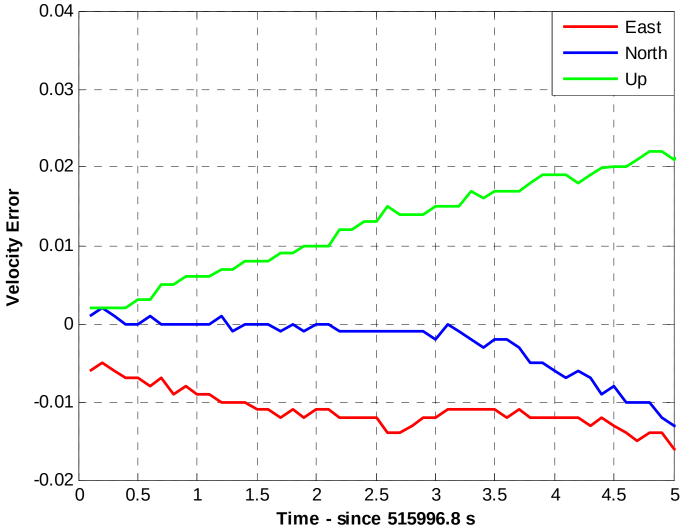

Figure 5.28: Velocity Performance for the Ultra-Tight Receiver over 5 Seconds during the First Bridge Scenario

Figure 5.29 shows the predicted carrier phase performance.

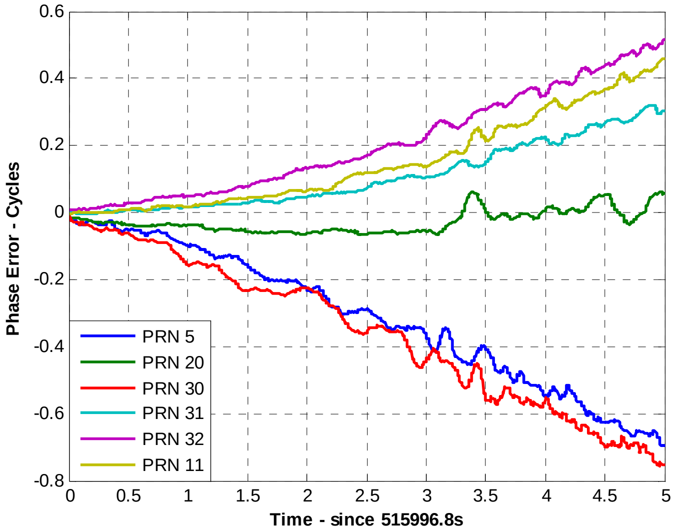

Figure 5.29: Predicted Phase Performance for Ultra-Tight Receiver over 5 Seconds during the First Bridge Scenario

As expected, a degraded phase prediction performance is obtained compared to the dense-foliage scenario. This is straightforward since without the updating of the GNSS observations, the INS-alone velocity error will grow unbound. Figure 5.30 summarizes the performance of five different scenarios.

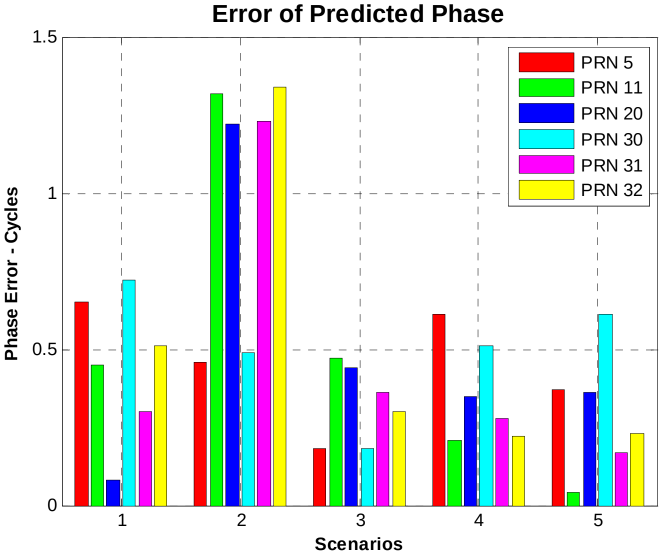

Figure 5.30: Phase Performance Summary for Ultra-Tight Receiver over 5 Seconds for Passing under Bridge Scenarios

It is noted that in the second scenario, the phase errors are much larger than in the other scenarios, this is due to the velocity error as mentioned before. For the other four scenarios, the maximum phase error is 0.72 cycles after 5 seconds. The benefit for the ultra-tight receiver with the phase prediction method is that, when the satellite signal becomes available again or at least becomes strong enough to acquire, the phase of the signal is already available from the INS, which means that the tracking loop can be started with relatively small initial phase and frequency errors

The work then ongoing to the PLL convergence behaviours assessment with different initial phase errors. Figure 5.31 shows the transition process for different initial carrier phase errors after reacquiring the signal. Four specific phase errors are of interest, which are 0.23 cycles, 0.46 cycles, 0.68 cycles, and 0.79 cycles, respectively. The general conclusion is that if the phase error is smaller than 90 degrees, it will converge to zero phase error (mathematically, however, a noise will be introduced in the PLL in practice); if the initial phase error is between 90 degrees and 270 degrees, it will converge to 180 degrees phase error; and finally, for errors larger than 270 degrees, it will converge to 360 degrees (1 cycle) phase error. Figure 5.31 shows the transition processes for different initial phase errors.

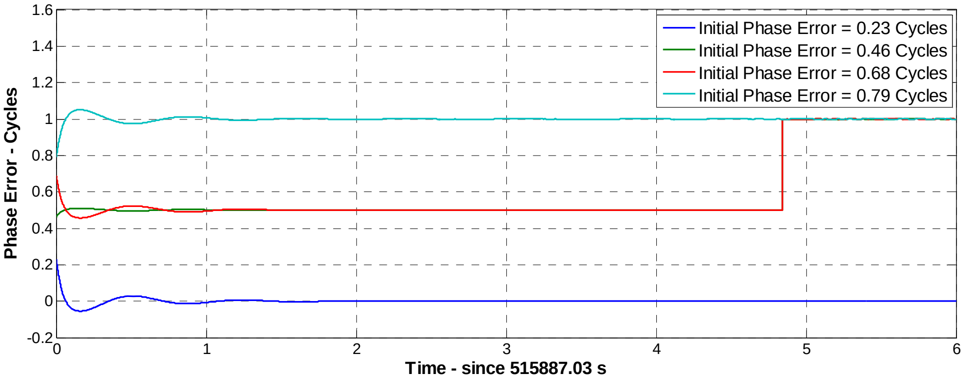

Figure 5.31: Transition Process for Different Initial Phase Errors

It is observed that for 0.23 cycles initial phase error, the phase error will be reduced by the transition process, however, for 0.46 cycles and 0.68 cycles initial phase errors, the phase errors are 0.5 cycles after reaching steady-state. At epoch 515891.9 s (4.87 s in the plot), the half-cycle lock is detected on this satellite, and then the phase errors become one cycle after half-cycle phase error correction. For 0.79 cycles initial phase error, the phase error after reaching steady-state is one cycle, in which case one needs to fix ambiguity again.

5.6 Conclusion

This chapter introduced a phase prediction method and assessed its performance in a GNSS-only receiver and an ultra-tight receiver in different scenarios. Specifically, partially dense-foliage, dense-foliage, and passing under bridges were considered. The phase prediction performance is highly correlated to the receiver velocity performance, a higher velocity quality will result in a better phase prediction performance. After employing the phase prediction method, the reacquisition process could possibly start with a small initial phase (and frequency) error, thus resulting in a faster carrier phase reacquisition.

CHAPTER SIX: CONCLUSIONS AND FUTURE WORKS

This thesis presented a thorough assessment for reducing carrier phase reacquisition time using advanced receiver architectures. This chapter discusses the main conclusions derived from the thesis, followed by recommendations for future work that can complement its work.

6.1 Conclusions

All of the objectives listed in Chapter 1 were achieved. First, a piece-wise control method was developed and evaluated. Second, the Kalman filter natural frequency was derived, and the transition process of the estimator-based tracking loop was assessed. Finally, a phase prediction method was proposed and employed in the vector-based receiver and ultra-tight receiver. Conclusions from each are expanded below.

6.1.1 Piece-Wise Control Method Assessment

Piece-wise control methods have been proposed in this work, a piece-wise FLL followed by a piece-wise PLL method was recommended. Different loop filter parameter values were assessed in order to achieve fast carrier phase reacquisition. The following conclusions can be drawn

1. Piece-wise FLL is used to reduce the frequency transition time in the reacquisition process, and enable a PLL start with a small initial frequency error. The transition processes of different natural frequencies and damping ratios were evaluated, as well as the logic of how to control the transitions between different loop filter parameter sets. Generally the piece-wise FLL control divides the reacquisition

and tracking process into separate periods each with different natural frequencies and damping ratios. Proper parameter sets have been obtained during the parameter tuning process. At the first period, the natural frequency and damping ratio are 60 Hz and 5.6 respectively and the piece-wise period is 20 ms. After the piece-wise method, general tracking loop parameters are used. In so doing, the piece-wise method produces a three-fold improvement in transition time. For example, the frequency transition is reduced from 0.59 s to 0.26 s for 200 Hz initial frequency error.

2. The same tracking loop parameters have been employed by the piece-wise PLL, whereas the improvement with the piece-wise approach is noticeable with a four- to five-fold improvement in all initial phase errors. To this end, for a 200 Hz initial frequency error and 90 degrees initial phase error case, the transition time is reduced from 0.91 s to 0.25 s, which means that more carrier phase observations are available after employing piece-wise control methods.
3. The drawback of piece-wise control method is however those larger damping ratios have slow reactions to user dynamics, and larger bandwidths introduce more noise in the tracking loop piece-wise period. Moreover, the time-based logic used in this work sometimes is not long enough to reduce the initial frequency error.

6.1.2 Kalman Filter Tracking Loop Assessment

The equivalence between the Kalman filter and standard tracking loops was shown in this work, and a faster transition process was obtained by using Kalman filter tracking loop in the software receiver. The following conclusions can be drawn

1. The natural frequency of estimator-based tracking loop has been derived for a three-state Kalman filter and a five-state Kalman filter. Different signal powers and process noises produce different Kalman filter natural frequencies. For a 50 dB/Hz C/N$_0$ and 4 $m/s^2/\sqrt{Hz}$ line of sight spectral density (process noise), the natural frequency is around 5 Hz.
2. Faster frequency and phase transition times were obtained in the estimator-based tracking loop. This is attributed to the fact that both the phase and frequency are updated by the filter, instead of just the frequency in a standard loop. However, the overshoot for the estimator-based tracking loop is slightly larger than the standard tracking loop.

6.1.3 Phase Prediction Method Assessment

Phase prediction method has been proposed and assessed by the vector-based receiver and ultra-tight receiver respectively. The phase prediction performance is highly correlated to the receiver velocity performance, which has been shown mathematically in the thesis. A higher velocity quality will result in a better phase prediction performance.

1. Open-sky, partially dense-foliage, and dense-foliage scenarios were assessed in the vector-based receiver. In the open-sky scenario, the predicted phase is a random walk process, since the receiver velocity output is white noise. A real data

assessment was shown in the partially dense-foliage scenario, the carrier phase for loss of lock satellites was predicted over 0.6 s with a maximum 0.17 cycles phase error. In turn, the tracking loop can be started with small frequency error and small phase error after the signal is available again. For the dense-foliage assessment, simulated dense-foliage scenarios were first used to obtain a baseline performance of the vector-based receiver. Next, real dense-foliage scenarios were assessed. In the dense-foliage scenario, the higher elevation satellites can be used to generate receiver velocity, then predicted phase for low elevation satellites can be obtained. It is shown that the phase error is smaller than half-cycle after 5 seconds.

2. Dense-foliage and passing under bridge scenarios were assessed in the ultra-tight receiver. Better phase prediction performance than the vector-based receiver was shown with the predicted phase error being smaller than 0.5 cycles after 15 seconds in the dense-foliage scenario. In the under pass scenario, the GNSS signal cannot be tracked in the GNSS-alone receivers, however, with the aiding information from the INS, effective carrier phase can be predicted with a maximum error of 0.72 cycles after 5 seconds, which was shown in the simulated scenario.

6.2 Recommendations for Future Works

Following these conclusions, this section lists the recommendations for the future work.

1. Implement the piece-wise method in the estimator-based architecture. Faster frequency and phase transition times were obtained in the estimator-based

receiver and these improvements are expected in a piece-wise estimator-based architecture.

2. Investigate the phase prediction performance with different vehicle velocity and acceleration scenarios, as well as different navigation filter orders (e.g., with or without acceleration state in the Kalman filter state vector)
3. Investigate the ultra-tight receiver performance with the aiding information from the commercial inertial measurement unit, such as MEMS. Since the predicted phase quality depends on the receiver velocity performance, the ultra-tight receiver with low quality IMU is of interest.
4. Investigate the possibility of using predicted carrier phase in carrier phase applications such as RTK, especially, after passing under bridges or through heavy foliage. Effectively, this would test the phase prediction architecture's ability to provide continuous RTK results.
5. The simulations shown in the piece-wise method and phase prediction method were limited to vehicle dynamics and the maximum frequency error is assumed to be 200 Hz. Testing the developed algorithm on the higher order dynamics is necessary.

References

Alban, S., D. M. Akos, S. M. Rock and D. Gebre-Egziabher (2003) Performance Analysis and Architectures for INS-Aided GPS Tracking Loops, in Proceedings of ION NTM 2003, Anaheim, CA, 22-24 January, pp. 611-622

Bar-Itzhack, I. Y. (1981) Minimal Order Time Sharing Filters for INS In-Flight Alignment, Journal of Guidance, Control and Dynamics, vol. 5, pp. 396-402

Bar-Itzhack, I. Y. (1988) Control theoretic approach to inertial navigation systems, Journal of Guidance, 11(3), pp. 237-245

Best, R. E. (2004) "Phase-Locked Loops: Design, Simulation, and Applications", 6th Edition, McGraw-Hill

Borio, D., C. O'Driscoll (2009), ENGO638 Lecture Notes, Department of Geomatics Engineering, the University of Calgary

Borio, D. N. Sokolova, and G. Lachapelle (2009) Doppler Measurements and Velocity Estimation: a Theoretical Framework with Software Receiver Implementation, in Proceeding of ION GPS GNSS, 23-25 September, Savannah, Georgia

Borre, K., D. M. Akos, N. Bertelsen, and P. Rinder (2006) "A Software-Defined GPS and Galileo Receiver", Birkhauser Boston

Brown, R. G. P. Y. C. Hwang (1996) "Introduction to Random signal and applied Kalman filtering", 3rd edition, Wiley Inc

Chiou, T. Y. (2004) GPS Receiver Performance Using Inertial-Aided Carrier Tracking Loop, in Proceedings of ION GNSS, 13-16 September, Long Beach CA, pp. 2895-2910

Chiou, T. Y., D. Gebre-Egziabher, T. Walter, and P. Enge (2007) Model Analysis on thePerformance for an Inertial Aided FLL-Assisted PLL Carrier-Tracking Loop in the Presence of Ionospheric Scintillation, in Proceedings of ION NTM 2007, 22-24 Jan., San Diego, CA, pp. 1276-1295

Farrell, J. A. and M. Barth (1998) "The Global Positioning System and Inertial Navigation", McGraw-Hill Publications

Farrell, J. A. (2008) “Aided Navigation: with High Rate Sensors”, McGraw-Hill Publications

Gao, Y (2008) ENGO629 Lecture Notes, Department of Geomatics Engineering, the University of Calgary

Gardner, F. M. (2005) “Phaselock Techniques”, Wiley Interscience

Gebre-Egziabher, D. (2001) Design and Performance Analysis of A Low-Cost Aided Dead Reckoning Navigator, Ph.D. dissertation, Stanford University

Gebre-Egziabher, D., and Razavi, A. (2003) Doppler Aided Tracking Loops for SRGPS Integrity Monitoring, in Proceeding of ION GPS/GNSS03, 9-12 September, Portland OR, pp. 2562-2571

Gebre-Egziabher, D. (2005) Sensitivity and Performance Analysis of Doppler-Aided GPS Carrier-Tracking Loops, in Navigation, Vol 52, No 2, Summer 2005, pp. 49-60

Gelb, A. (1974) “Applied Optimal Estimation”, The M.I.T. Press

Godha, S. (2006) Performance Evaluation of Low Cost MEMS-Based IMU Integration with GPS for Land Vehicle Navigation Application, Master Thesis, Department of Geomatics Engineering, the University of Calgary

Jekeli, C. (2000) Inertial Navigation Systems with Geodetic Applications, Berlin, Walter de Gruyter

Jovancevic, A. A. Brown, S. Ganguly, J. Noronha, B. Sirpatil (2004), Ultra Tight Coupling Implementation Using Real Time Software Receiver, in Proceeding of ION GNSS 2004, 21-24 September, Long Beach, CA

Jury, E. I. (1964) “Theory and Application of the z-Transform Method”, New York: John Wiley & Sons

Jwo, D. J. (2001) Optimisation and Sensitivity Analysis of GPS Receiver Tracking Loops in Dynamic Environments, IEE Proceeding of Radar, Sonar Navigation

Kaplan, E. D. (2006) “Understanding GPS: Principle and Applications”, Second Edition, Artech House, Boston

Kiesel, S. (2008) GNSS Receiver with Vector Based FLL-Assisted PLL Carrier Tracking Loop, in Proceeding of ION GNSS, 16-19, September, Savannah GA, pp. 197-203

Kim, H.S., S.C. Bu, G.I. Jee and C.G. Park (2003) An Ultra-Tightly Coupled GPS/INS Integration Using Federated Filtering, ION GPS/GNSS 2003, Portland, OR, Institute of Navigation, 2878-2885

Kuipers, J. B. (1998) "Quaternions and Rotation Sequences", Princeton University Press

Lachapelle, G. (2008) ENGO625 Lecture Notes, Department of Geomatics Engineering, the University of Calgary

Lashley, M. and D. Bevly (2007) Analysis of Discriminator Based Vector Tracking Algorithms, In Proceedings of ION NTM, 22-24 January, San Diego CA, pp. 570-576

Lashley, M. and D. Bevly (2008) Comparison of traditional tracking loops and vector based tracking loops for weak GPS signals, in Proceedings of ION NTM, 28-30 January, San Diego CA, pp. 310-316

Mongredien, C., G. Lachapelle, and M. E. Cannon (2006) Testing GPS L5 Acquisition and Tracking Algorithms Using a Hardware Simulator. Proceedings of ION GNSS 2006, Fort Worth, TX, Institute of Navigation, pp. 2901–2913

O'Driscoll, C., M. G. Petovello, and G. Lachapelle (2008) Software Receiver Strategies for the Acquisition and Re-Acquisition of Weak GPS Signals, in Proceeding of ION NTM, 28-30 January, San Diego CA, pp. 843-854

O'Driscoll, C. and G. Lachapelle (2009) Comparison of Traditional and Kalman Filter Based Tracking Architectures, in Proceedings of European Navigation Conference 2009, Naples, Italy, May 3-6, 2009

O'Driscoll, C., D. Borio, M.G. Petovello, T. Williams and G. Lachapelle (2009) The Soft Approach: A Recipe for a Multi-System, Multi-Frequency GNSS Receiver, Inside GNSS Magazine, Volume 4, Number 5, pp. 46-51

Odijk, Dennis. (2002) Fast Precise GPS Positioning in the Presence of Ionospheric Delays, published by Netherlands Geodetic Commission, Delft, The Netherlands

Ogata, K. (1997) “Modern Control Engineering”, third edition, Prentice Hall

Parkinson, B. W. and J. J. Spilker (1996) “Global Positioning System: Theory and Applications,” Vol.1, American Institute of Aeronautics and Astronautics publication, Inc.

Petovello, M. G. (2003), Real-Time Integration of a Tactical-Grade IMU and GPS for High-Accuracy Positioning and Navigation, PhD thesis, Department of Geomatics Engineering, the University of Calgary

Petovello, M. G. and G. Lachapelle (2006) Comparison of Vector-Based Software Receiver Implementations with Application to Ultra-Tight GPS/INS Integration, in Proceedings of ION GNSS, 26-29 September, Fort Worth TX, pp.2977-2989

Petovello, M.G., C. O'Driscoll and G. Lachapelle (2007) Ultra-Tight GPS/INS for Carrier Phase Positioning in Weak Signal Environment. NATO RTO SET-104 Symposium on Military Capabilities Enabled by Advances in Navigation Sensors, Antalya, Turkey, 1-2 October 2007

Petovello, M.G., C. O'Driscoll and G. Lachapelle (2008) Weak Signal Carrier Tracking Using Extended Coherent Integration with an Ultra-Tight GNSS/IMU Receiver. European Navigation Conference 2008, Toulouse, France, 23-25 April

Psiaki, M. L. (2002) Extended Kalman Filter Methods for Tracking Weak GPS Signals, in Proceedings of ION GPS02, 24-27 September, Portland OR, pp. 2539-2553

Psiaki, M. L. (2007) Tracking L1 C/A and L2C Signals through Ionospheric Scintillations, in Proceeding of ION ITM, 25-28 September, Fort Worth TX, pp. 246-268

Razavi, A. (2008) Carrier Loop Architectures for Tracking Weak GPS Signals, IEEE Transactions on Aerospace and Electronic Systems, Vol. 44, No. 2, pp. 697-710

Rogers, R. M. (2003) “Applied Mathematics in Integrated Navigation Systems”, 2nd edition, AIAA Publications

Ronald, J. C. D. W. Diggle, M. U. de Haag, and Christopher J. H (2006) "Differential GPS," Chapter 8 in Understanding GPS Principles and Applications, second edition, Artech House Mobile Communications Series

Rosales, J. J., I. Colomina (2005) A Flexible Approach for the Numerical Solutions of the INS Mechanization Equations, Proceedings of the 6th Geomatic Week, Barcelona

Salem, D. R. (2010) Approached for the Combined Tracking of GPS L1/L5 Signals, PhD thesis, Department of Geomatics Engineering, the University of Calgary

Savage, P. G. (1998) Strapdown Inertial Navigation Integration Algorithm Design Part 2: Velocity and Position Algorithms, Journal of Guidance, Control, and Dynamic, Vol. 21, No. 2, March–April 1998

Savage, P. G. (2000) "Strapdown Analytics", vol.1. Strapdown Associates, Inc.

Simon, D. and H. EI-Sherief (1996) Hybrid Kalman filtering in phase locked loops, Control Engineer. Practice, Vol. 4, No. 5, pp. 615-623

Simon, D. (2006) "Optimal State Estimation: Kalman, H∞, and Nonlinear Approaches", John Wiley & Sons, Inc

Soloviev, A., S. Gunawardena, and F. van Graas (2004), Deeply Integrated GPS/Low-Cost IMU for Low CNR Signal Processing: Flight Test Results and Real Time Implementation, ION GNSS 17th ITM, 21-24 September, 2004, Long Beach, CA

Spilker, J. J. (1994) "Fundamentals of Signal Tracking Theory in Global Positioning System: Theory and Applications", vol. I, B. W. Parkinson and J. J. Spilker, Jr., Eds.: American Institute of Aeronautics and Astronautics, Inc., 1994, pp. 245-327.

Spilker, J. J. (1996) "GPS Signal Structure and Theoretical Performance. In Parkinson, B. W., editor, Global Positioning System: Theory and Applications", Volume 1, volume 163 of Progress in Astronautics and Aeronautics, chapter 3. American Institute of Aeronautics and Astronautics, Washington, DC.

Statman, J. and W. Hurd (1990) An Estimator-Predictor Approach to PLL Loop Filter Design. IEEE Transactions on Communications

Sun, D. (2010) Ultra-Tight GPS/Reduced IMU for Land Vehicle Navigation, Ph.D thesis, the University of Calgary

Thomas J. B. (1989) An Analysis of Digital Phase-Locked Loops, Jet Propulsion Laboratory Publication 89-2, California Institute of Technology, Pasadena, California, February 1989

Titterton, D. H. and J. L. Weston (2004) "Strapdown Inertial Navigation Technology", 2nd Edition, Peter Peregrinus Ltd., The Institution of Electrical Engineers, London, United Kingdom

Tsui, J. (2004) "Fundamentals of Global Positioning System Receivers: A Software Approach". Wiley, 2004

Van Dierendonck, A. J. (1996) "GPS Receivers," Chapter 8 in Global Positioning System: Theory and Applications, Volume 1, B. W. Parkinson & J. J. Spilker Jr., ed., American Institute of Aeronautics and Astronautics, Inc., Washington D. C.

Ward, P. W., J. W. Betz, and C. J. Hegarty (2006) "Satellite Signal Acquisition, Tracking and Data Demodulation," Chapter 5 in Understanding GPS Principles and Applications, second edition, Artech House Mobile Communications Series

Watson, J. (2005) High-Sensitivity GPS L1 Signal Analysis for Indoor Channel Modelling, Master thesis, the University of Calgary

Wendel, J. G. F. Trommer (2004), Tightly Coupled GPS/INS Integration for Missile Applications, Aerospace Science and Technology, 8, pp. 627-634

Zarchan, P. (2005) "Fundamentals of Kalman Filtering: A Practical Approach", Second Edition, American Institute of Aeronautics and Astronautics, Inc

APPENDIX A:

INS ERROR PROPOGATION EQUATIONS

Navigation error arises due to errors in the initial states and the accumulation of instrumentation errors through the integration process (Farrell 2008). Consequently, error analysis is of utmost importance in the design and operation of INS. Error analysis enables the estimation of the INS sensor accuracy and initial conditions before the mission. The purpose of this section is to give the error propagation equation of the INS.

Many models have been developed to describe the error propagation behaviour of INS errors in the literature (Bar-Itzark 1988, Savage 2000, Farrell 1998), the two most important models are Phi-angle error model and Psi-angle error model. Phi-angle method is employed in this work. For the Phi-angle method, error models are derived by perturbing the differential equations used in the mechanization process, where the navigation parameters are perturbed with respect to the true navigation frame. The full derivation of error model can be found in Schwarz (1999), Bar-Itzhack (1988), Farrell (2008), which will not be derived here. Instead, the final results are shown in this section, the error model has the form as shown below:

$$\begin{bmatrix} \delta\dot{p} \\ \delta\dot{v} \\ \dot{\varepsilon} \end{bmatrix} = \begin{bmatrix} F_{pp} & F_{pv} & F_{p\varepsilon} \\ F_{vp} & F_{vv} & F_{v\varepsilon} \\ F_{\varepsilon p} & F_{\varepsilon v} & F_{\varepsilon\varepsilon} \end{bmatrix} \begin{bmatrix} \delta p \\ \delta v \\ \varepsilon \end{bmatrix} + \begin{bmatrix} 0 & 0 \\ -R_b^n & 0 \\ 0 & R_b^n \end{bmatrix} \begin{bmatrix} \delta f^b \\ \delta\omega_{ib}^b \end{bmatrix} \tag{A.1}$$

The error vector is defined as $\delta x = \begin{bmatrix} \delta p & \delta v & \varepsilon \end{bmatrix}^T$, where

$$\delta p = \begin{bmatrix} \delta\phi & \delta\lambda & \delta h \end{bmatrix}^T \tag{A.2}$$

$$\delta v = \begin{bmatrix} \delta v_n & \delta v_e & \delta v_d \end{bmatrix}^T \tag{A.3}$$

$$\varepsilon = \begin{bmatrix} \varepsilon_n & \varepsilon_e & \varepsilon_d \end{bmatrix}^T \tag{A.4}$$

where v	:	Vehicle velocity
p	:	Vehicle position
ε	:	Attitude error
δf^b	:	Accelerometer error
$\delta\omega_{ib}^b$	:	Gyroscope error
n, e, d	:	North, East, and Down directions

The position error system model is given by

$$\delta\dot{p} = F_{pp}\delta p + F_{pv}\delta v + F_{p\varepsilon}\varepsilon \tag{A.5}$$

where

$$F_{pp} = \begin{bmatrix} 0 & 0 & \dfrac{-v_n}{(R_M + h)^2} \\ \dfrac{v_e}{(R_N + h)}\tan\phi\sec\phi & 0 & \dfrac{-v_e}{(R_N + h)^2\cos\phi} \\ 0 & 0 & 0 \end{bmatrix} \tag{A.6}$$

$$F_{pv} = \begin{bmatrix} \frac{1}{(R_M + h)} & 0 & 0 \\ 0 & \frac{\sec\phi}{(R_N + h)} & 0 \\ 0 & 0 & -1 \end{bmatrix} \tag{A.7}$$

$$F_{p\varepsilon} = \begin{bmatrix} 0 & 0 & 0 \\ 0 & 0 & 0 \\ 0 & 0 & 0 \end{bmatrix} \tag{A.8}$$

where	R_N	:	Radii of curvature along lines of constant latitude
	R_M	:	Radii of curvature along lines of constant longitude
	ϕ	:	Vehicle latitude
	h	:	Vehicle height

The velocity error is given by

$$\delta\dot{v} = F_{vp}\delta p + F_{vv}\delta v + F_{v\varepsilon}\varepsilon - R_b^n \delta f^b \tag{A.9}$$

where

$$F_{vp} = \begin{bmatrix} -2\omega_{ie} v_e \cos\phi - \frac{v_e^2 \sec^2\phi}{(R_N + h)} & 0 & \frac{-v_n}{(R_M + h)^2} \\ 2\omega_{ie} v_n \cos\phi + \frac{v_e v_n \sec^2\phi}{(R_N + h)} & 0 & \frac{-v_e}{(R_N + h)^2 \cos\phi} \\ -2 v_e \omega_{ie} \sin\phi & 0 & 0 \end{bmatrix} \tag{A.10}$$

$$F_{vv} = \begin{bmatrix} \frac{v_d}{R_e} & -2\omega_{ie}\sin\phi - \frac{2v_e\tan\phi}{R_e} & \frac{v_n}{R_e} \\ 2\omega_{ie}\sin\phi + \frac{v_e\tan\phi}{R_e} & \frac{v_d}{R_e} + \frac{v_n\tan\phi}{R_e} & 2\omega_{ie}\cos\phi + \frac{v_e}{R_e} \\ -\frac{2v_n}{R_e} & -2\omega_{ie}\cos\phi - \frac{2v_e}{R_e} & 0 \end{bmatrix} \tag{A.11}$$

$$F_{v\varepsilon} = \begin{bmatrix} 0 & f_d & -f_e \\ -f_d & 0 & f_n \\ f_e & -f_n & 0 \end{bmatrix} \tag{A.12}$$

Equation (A.9) also shows the relationship between accelerometer error and velocity error, the accelerometer error will be projected into the navigation frame, which then increases the velocity error.

The attitude error is given by

$$\dot{\varepsilon} = F_{\varepsilon p}\delta p + F_{\varepsilon v}\delta v + F_{\varepsilon\varepsilon}\varepsilon + R_b^n \delta\omega_{ib}^b \tag{A.13}$$

where

$$F_{\varepsilon p} = \begin{bmatrix} -\omega_{ie}\sin\phi & 0 & \frac{v_e}{\left(R_N + h\right)^2} \\ 0 & 0 & \frac{-v_n}{\left(R_M + h\right)^2} \\ \omega_{ie}\cos\phi + \frac{v_e\sec^2\phi}{\left(R_N + h\right)} & 0 & \frac{-v_e\tan\phi}{\left(R_N + h\right)^2} \end{bmatrix} \tag{A.14}$$

$$F_{\varepsilon v} = \begin{bmatrix} 0 & \dfrac{-1}{R_N + h} & 0 \\ \dfrac{1}{R_M + h} & 0 & 0 \\ 0 & \dfrac{\tan\phi}{R_N + h} & 0 \end{bmatrix} \tag{A.15}$$

$$F_{\varepsilon\varepsilon} = \begin{bmatrix} 0 & -\omega_{ie}\sin\phi - \dfrac{v_e \tan\phi}{(R_N + h)} & \dfrac{v_n}{(R_M + h)} \\ \omega_{ie}\sin\phi + \dfrac{v_e \tan\phi}{(R_N + h)} & 0 & \omega_{ie}\cos\phi + \dfrac{v_e}{(R_N + h)} \\ -\dfrac{v_n}{(R_M + h)} & -\omega_{ie}\cos\phi - \dfrac{v_e}{(R_N + h)} & 0 \end{bmatrix} \tag{A.16}$$

Equation (A.13) also shows the relationship between gyroscope error and attitude error. The gyroscope error will be projected to the navigation frame, and then increases the attitude error.

The vertical error channels are unstable and must be compensated by negative feedback. Also, the vertical channel has a weak affect on other states, so usually vertical channel are removed from the error model (Bar-Itzhack 1981, Savage 2000, Farrell 2008). Reduced-order error models are also used in some specific applications due to the stringent requirements of the onboard computer or Kalman filter observability consideration.

APPENDIX B:

THREE-STATE KALMAN FILTER NATURAL FREQUENCY

Appendix B derives the natural frequency for the three-state Kalman filter. Theoretically, an estimator-based tracking loop is essentially a standard tracking loop after Kalman filter reaching steady-state (Zarchan 2005). The Kalman filter can be simplified to become equivalent to a standard control system, which means that the natural frequency concept can also be applied in the Kalman filter. The following is an example demonstrating how to get the equivalent natural frequency of a three-state estimator-based tracking loop (Zarchan 2005).

The state vector is given by (Psiaki et al 2007)

$$X = \begin{bmatrix} \delta\varphi & \delta f & \delta a \end{bmatrix}^T \tag{B.1}$$

where $\delta\varphi$: Phase tracking error

δf : Frequency tracking error

δa : Frequency error rate

The system model is given by

$$F = \begin{bmatrix} 0 & 1 & 0 \\ 0 & 0 & 1 \\ 0 & 0 & 0 \end{bmatrix} \tag{B.2}$$

For simplicity, the phase error from the discriminator is taken as a measurement in the Kalman filter; however, in the general architecture, the I and Q correlations are used as measurements directly. The observation matrix is thus given by:

$$H = \begin{bmatrix} 1 & 0 & 0 \end{bmatrix} \tag{B.3}$$

If only the frequency rate error uncertainty is modeled stochastically, the corresponding process noise is given by:

$$Q = \begin{bmatrix} 0 & 0 & 0 \\ 0 & 0 & 0 \\ 0 & 0 & \omega_a \end{bmatrix} \tag{B.4}$$

where ω_a : Driving noise to account for line-of-sight acceleration

And observation noise is given by:

$$R = \omega_\phi \tag{B.5}$$

where ω_ϕ : Phase noise from discriminator

In order to get the natural frequency of the Kalman filter, the steady-state filter gain should be derived first (Zarchan 2005). Specially, the filter gain is a constant matrix after reaching steady-state, and the continuous Kalman filter can be simplified as:

$$\dot{X} = FX + K_C\left(z - HX\right) \tag{B.6}$$

where K_C : Continuous filter gain, which denoted as $\begin{bmatrix} K_1 & K_2 & K_3 \end{bmatrix}^T$

z : Measurement from the phase discriminator

The discrete Kalman filter is given by:

$$X_{k+1} = AX_{k+1/k} + K_D\left(z_{k+1} - HX_{k+1/k}\right) \tag{B.7}$$

where A : Discrete form of the system model

K_D : Discrete form of filter gain

The continuous filter gain, K_C, and discrete filter gain, K_D, are related according to:

$$K_D = K_C \cdot T_S \tag{B.8}$$

where T_S : Kalman filter time interval

A transfer function for the Kalman filter can also be developed in the steady-state Kalman filter. Note that Equation (B.6) can be expanded as:

$$\delta\dot{\varphi} = \delta\varphi + K_1\left(z - \delta\varphi\right) \tag{B.9}$$

$$\delta\dot{f} = \delta f + K_2\left(z - \delta f\right) \tag{B.10}$$

$$\delta\dot{a} = \delta a + K_3\left(z - \delta a\right) \tag{B.11}$$

After some algebraic manipulation and taking the Laplace transform (Ogata 2005), Kalman filter transfer function was obtained from the state estimates to the measurements as (Zarchan 2005):

$$\frac{\delta\varphi}{z} = \frac{K_3 + sK_2 + s^2K_1}{K_3 + sK_2 + s^2K_1 + s^3} \tag{B.12}$$

It is observed that Equation (B.12) is quite closed to Equation (2.3) in Chapter 2. Now, the problem turns out to be how to obtain the constant filter gain.

The steady-state equation for the Kalman filter is derived by noting that steady-state is reached when the covariance matrix no longer changes. To this end, the continuous Riccati equation is employed to get the steady-state filter gain, K_C, as well as the steady-state covariance matrix, P (Zarchan 2005, O'Driscoll 2009). The continuous Riccati equations are given by:

$$\dot{P} = -PH^T R^{-1} HP + PF^T + FP + Q \tag{B.13}$$

$$K_C = PH^T R^{-1} \tag{B.14}$$

where P : Steady-state filter covariance matrix

By solving this equation, the continuous steady-state gain vector is given as (Zarchan 2005):

$$K_C = \begin{bmatrix} 2\left(\frac{\omega_a}{\omega_\phi}\right)^{\frac{1}{6}} & 2\left(\frac{\omega_a}{\omega_\phi}\right)^{\frac{1}{3}} & \left(\frac{\omega_a}{\omega_\phi}\right)^{\frac{1}{2}} \end{bmatrix}^T \tag{B.15}$$

However, it is important to note that this equation is only satisfied when the filter interval time is small.

If $\left(\frac{\omega_a}{\omega_\phi}\right)^{\frac{1}{6}}$ is defined as the natural frequency, ω_n, Equation (B.15) can be rewrite as:

$$K_C = \left[2\omega_n \quad 2\omega_n^2 \quad \omega_n^3\right]^T \tag{B.16}$$

Equation (B.12) can be expressed as:

$$\frac{\delta\varphi}{z} = \frac{2\omega_n s^2 + 2\omega_n^2 s + \omega_n^3}{s^3 + 2\omega_n s^2 + 2\omega_n^2 s + \omega_n^3} \tag{B.17}$$

Compared to Equation (2.3) in Chapter 2, the three-state Kalman filter has the same close-loop transfer function as the standard third-order PLL, which means that the estimator-based tracking loop is essentially a standard PLL after reaching steady-state. Note that the natural frequency is a function of process noise and observation noise, the natural frequency will be increased if the process noise increases or the observation noise decreases. This is straightforward since, if the observation noise increases, the natural frequency should be reduced in order to reject the noise. Conversely, if the process noise is increased, which means that the dynamic model is no longer accurate, then the natural frequency should be increased to track the change in dynamics.

APPENDIX C:

FIVE-STATE KALMAN FILTER NATURAL FREQUENCY

The equivalence between the three-state Kalman and third-order PLL was already shown in Appendix B, in Appendix C, a method to derive the Kalman filter equivalent natural frequency is presented. As shown in Appendix B, the steady-state Kalman filter gain is given by

$$K_C = \begin{bmatrix} 2\omega_n & 2\omega_n^2 & \omega_n^3 \end{bmatrix}^T \tag{C.1}$$

where	K_C	:	Continuous filter gain
	ω_n	:	Natural frequency

Specially, filter gain K_C indicates the Kalman filter natural frequency. Mathematically, the steady-state filter gain is related to the observation noise and process noise as shown in Appendix B, however, in this section, the filter gain is obtained through practical way, since the steady-state filter gain can be output by the software receiver.

A five-state Kalman filter is employed in the software receiver whereas the signal amplitude and code phase error are considered in the system, as well as oscillator noises, which is different from the three-state Kalman filter assessed in Chapter 2. The natural frequency assessment in this section is based on the three-state Kalman filter, in order to compare the Kalman filter and standard PLL in a fairer manner, oscillator noises are removed from the process noise matrix. The parameters used in the Kalman filter are given by

Table C-1: Kalman Filter Parameters

States	5
C/N$_0$	50 dB/Hz
Observation Noise	0.005
Line of Sight Spectral Density	4 $m/s^2/\sqrt{Hz}$
Integration Time	1 ms

Table C-2 shows the steady-state gain of the Kalman filter.

Table C-2: Steady-State Filter Gain

	K(:,1) I$_E$	K(:,2) Q$_E$	K(:,3) I$_P$	K(:,4) Q$_P$	K(:,5) I$_L$	K(:,6) Q$_L$
K(1,:) A	9.42e-5	0	0.2248	2.43e-6	0	0
K(2,:) $\delta\tau$	0.0002	0	0.001	7.15e-6	0	0
K(3,:) $\delta\varphi$	1.45e-5	0	1.75e-5	0.07	0	0
K(4,:) δf	0.0004	0	0.001	2.06	0	0
K(5,:) δa	0.006	0	0.003	30.76	0	0

It is observed that the steady-state filter gains for the phase, frequency and frequency rate states corresponding to the early and late observations, and also the prompt I, are much smaller than the gain corresponding to the prompt Q, which suggests that the six-observation Kalman filter can be simplified as one-observation Kalman filter. In the further analysis, only $K(3,4)$, $K(4,4)$, and $K(5,4)$ are assessed. The steady-state gain is given by

$$K_D = \begin{bmatrix} 0.07 & 2.06 & 30.76 \end{bmatrix}^T$$

Rewrite the Equation (B.8) related the discrete gain and the continuous gain in Appendix B:

$$K_D = K_C \cdot T_S \qquad 1$$

where			
	K_D	:	Discrete steady-state gain
	K_C	:	Continuous steady-state gain
	T_S	:	Kalman filter time interval

Notice that this equation is only satisfied when $\omega_n T_S << 1$, which is true in this case since T_S is 0.001 s. Notice that $K_C\left(3\right) = \omega_n^3$, the equivalent natural frequency is then given by

$$\omega_n = \frac{\sqrt[3]{30.76/0.001}}{2\pi} = 4.98\ Hz$$

After getting the equivalent natural frequency for the Kalman filter, the next step is to evaluate how it compares to the standard PLL case. Herein, an empirical approach is used to compare the Kalman filter tracking with the equivalent standard PLL. More specifically, a strong signal under a static scenario is tracked, with a C/N$_0$ of 50 dB/Hz, is used. Figure C.1 shows the carrier frequency tracking performance of the estimator-based tracking loop and standard third-order PLL, the natural frequency of standard PLL is 5 Hz.

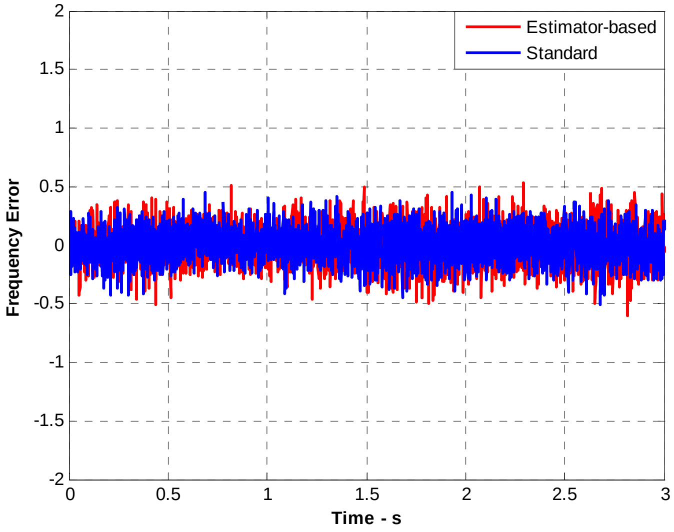

Figure C.1: Carrier Frequency Tracking Performance for Estimator-Based Tracking Loop and Standard PLL

Figure C.1 shows the results from both estimator-based tracking loop and standard PLL, it is observed that the two tracking methods give the same standard deviations for carrier frequency tracking, which are 0.16 Hz and 0.14 Hz respectively. This result suggests that the comparison procedure shown above returns a reasonable comparison of Kalman filter and standard PLL, which in turn, can be used to calculate the natural frequency of the five-state Kalman filter.

The natural frequency of Kalman filters with different process noises are summarized in Table C-3, assuming the observation noise is 0.005.

Table C-3: Equivalent Natural Frequency for Different Dynamics

	10 $m/s^2/\sqrt{Hz}$	20 $m/s^2/\sqrt{Hz}$	30 $m/s^2/\sqrt{Hz}$
$K(3,4)$	0.09	0.13	0.14
$K(4,4)$	4.95	9.14	10.44
$K(5,4)$	129.47	320.11	382.18
ω_n	8.1 Hz	10.8 Hz	11.5 Hz

Table C-4 shows the equivalent natural frequency with different C/N$_0$, assuming the vehicle dynamic are white noise with a spectral density of 4 $m/s^2/\sqrt{Hz}$. It is shown that a weaker signal power results in a smaller natural frequency, as should be expected.

Table C-4: Equivalent Natural Frequency for Different Observation Noises

	52 dB/Hz	44 dB/Hz	37 dB/Hz
$K(3,4)$	0.09	0.07	0.06
$K(4,4)$	3.44	2.05	2.03
$K(5,4)$	72.06	32.86	27.07
ω_n	6.6 Hz	5.1 Hz	4.8 Hz